An Investigation of Nonstoichiometric Oxides for Solar-Driven Thermochemical Fuel Production

Thesis by
Michael Joseph Ignatowich

In Partial Fulfillment of the
Requirements for the Degree of
Doctor of Philosophy

Caltech

CALIFORNIA INSTITUTE OF TECHNOLOGY
Pasadena, California

2017
(Defended May 12, 2017)

© 2017

Michael J. Ignatowich
ORCID: 0000-0002-0097-664X

ACKNOWLEDGEMENTS

First and foremost, thank you to my advisor, Professor Sossina Haile. She is one of the most reasonable advisors I could have hoped for and her guidance and careful judgement allowed me to grow as a scientist.

Thank you to all the Haile lab members past and present with whom I've had the opportunity to work and especially those who shared in the adventure of transporting the lab across the country, namely Dr. Timothy Davenport, Chris Kucharczyk, Anu Khan, Dr. Ho-Il Ji, Haemin Paik, and Dr. Sihyuk Choi and Stephen Wilke.

Thank you to the Caltech community for being so welcoming and diverse. A special thanks to Scott Jung and Ben Raphelson of the Caltech Cross Country and Track and Field teams. Their mentorship allowed me to both grow as an athlete and an ambassador of the sport.

Thank you to my family and friends for all the external support you've provided on my entire academic journey. A special appreciation to my loving parents, Jill and Bill, younger brothers, Steven and Daniel, and grandmother, Mary Genovese, for always supporting and encouraging me in each of my endeavors.

Thank you to the students and professors from around the world who I had the opportunity to collaborate with including Dr. Danielle Casillas and Chun-Han Lai of Professor Bruce Dunn's group at University of California-Los Angeles (inverse opals), Dr. Jie Yin of Professor Xue-Jian Liu's group at the Shanghai Institute of Ceramics, Chinese Academy of Sciences (reticulated porous ceramics), and Dr. Alexander Bork of Professor Jennifer Rupp's group at ETH Zurich (LSM thermodynamics).

Financial support for this work was provided by the DOE ARPA-e HEATS program and the NSF EFRI award with additional support from the International Center for Materials Research at the UCSB.

ABSTRACT

In order to realize energy independence and substantially combat global climate change, renewable and sustainable energy technologies must be developed. Solar energy is the most readily abundant, and if converted into a chemical fuel, could be stored and transported easily. Solar-driven thermochemical cycling is a method of chemical fuel production that shows great promise, but current state-of-the-art systems have very low efficiencies. This work discusses new reactor designs and cycling techniques using nonstoichiometric oxides that will enable more efficient solar to fuel energy conversion. Practical aspects of the reactor design are explored – specifically, thermochemical expansion of the reactive oxide, and morphologies aimed at enhancing the reaction kinetics. Additionally, doped fluorite- and perovskite-structured materials are evaluated for thermodynamic behavior and in-situ thermochemical cycling performance. Oxide morphology and new doped compounds show little improvement over previously established neat ceria due to thermodynamic limitations. The thermodynamic limit is explored in new reactor geometries and is shown to demonstrate significantly more efficient fuel production. Finally, different nonstoichiometry thermodynamics are explored to provide guidance for further material exploration, as well as applicable methodologies.

PUBLISHED CONTENT AND CONTRIBUTIONS

D. C. Casillas, D. C. Wilkinson, C.-H. Lai, S. K. Wilke, M. J. Ignatowich, S. M. Haile, and B. S. Dunn, "High-Temperature Structural Stability of Ceria-Biased Inverse Opals" J. Amer. Ceramic Soc. ***2017****, DOI: 10.1111/jace.14781*

http://onlinelibrary.wiley.com/doi/10.1111/jace.14781/full

Performed isothermal, chemical cycling, on zirconia doped ceria inverse opal samples. Evaluated experimental profiles against theoretical model. Performed gas phase diffusion calculations.

H.-I. Ji, T. C. Davenport, M. J. Ignatowich, and S. M. Haile, "Gas Phase vs. Material-Kinetic Limits on the Redox response of Nonstoichiometric Oxides" Phys. Chem. Chem. Phys. ***2017****, 19, 7420. DOI: 10.1039/C7CP00449D*

http://pubs.rsc.org/en/content/articlelanding/2017/cp/c7cp00449d#!divAbstract

Provided instruction on synthesis techniques for reticulated porous ceramics.

T. C. Davenport, C.-K. Yang, C. J. Kucharczyk, M. J. Ignatowich, and S. M. Haile, "Maximizing Fuel Production Rates in Isothermal Solar Thermochemical Fuel Production" Applied Energy. ***2016****, 183, 1098.DOI: 10.1016/j.apenergy.2016.09.012*

http://www.sciencedirect.com/science/article/pii/S0306261916313162

Performed scanning electron microscopy and energy dispersive spectroscopy on samples used for thermochemical cycling experiments.

T. C. Davenport, C.-K. Yang, C. J. Kucharczyk, M. J. Ignatowich, and S. M. Haile, "Implications of Exceptional Material Kinetics on Thermochemical Fuel Production Rates" Energy Technol. ***2016****, 4, 764. DOI:10.1002/ente.201500506*

http://onlinelibrary.wiley.com/doi/10.1002/ente.201500506/pdf

Codeveloped governing model for reduction and oxidation profiles. Performed isothermal pressure-swing cycling on ceria fiberboard for model verification.

TABLE OF CONTENTS

TABLE OF FIGURES

TABLE OF TABLES

NOMENCLATURE

Symbol	Units	Description
$\bar{\dot{\boldsymbol{v}}}_{H_2}$	sccm/g	cycle-averaged volumetric hydrogen production rate per gram of oxide
$\dot{V}_{H_2}$	mL/min	volumetric flow rate of hydrogen
$\dot{V}_{O_2}$	mL/min	volumetric flowrate per gram of oxide
$\dot{V}_{STP}$	mL/min	Volumetric flow rate at STP
$\dot{V}_{tot}$	sccm	total volumetric flow rate, $\dot{V}_{tot} = V_M F_{tot}$
$\langle\delta\rangle_{\Delta V}$	-	Average nonstoiciometry of the oxide in the control volume
$\dot{\boldsymbol{v}}_{H_2}^{t_{tot}}$	sccm/g	cycle-averaged volumetric hydrogen production rate for an incremental swing in nonstoichiometry
$\dot{\boldsymbol{v}}_{H_2}$	sccm/g	volumetric hydrogen production rate per gram of oxide
$\dot{\boldsymbol{v}}_{O_2}$	sccm/g	volumetric oxygen production rate per gram of oxide
$\mathbf{I_0}$	-	normalized zeroth order peak intensity
$\mathbf{I_r}$	-	relative intensity (I/I_0)
γ_0	-	relative order parameter for the as synthesized material
γ_r	-	relative order parameter
Ω_D	-	Collision integral for molecular diffusion
$D_{O_2.Ar}$	cm^2/s	diffusion coefficient of oxygen in argon
F_{H_2O}	mol/min	Molar flow rate of water
F_{H_2Oin}	mol/min	molar flow rate of water at inlet of reactor
F_{H_2Oout}	mol/min	molar flow rate of water at outlet of reactor
F_{O_2}	mol/min	molar flow rate of oxygen
F_{O_2in}	mol/min	molar flow rate of oxygen at inlet of reactor
F_{O_2out}	mol/min	molar flow rate of oxygen at outlet of reactor
F_{out}	mol/min	molar flow rate at outlet of reactor
F_{ox}	mol/min	molar flow rate at inlet of reactor during oxidation

$\boldsymbol{F_{red}}$	mol/min	molar flow rate at inlet of reactor during reduction
$\boldsymbol{F_{tot}}$	mol/min	total molar flow rate, $F_{tot} = F_{red} + F_{ox}$
$\boldsymbol{K_{H_2O,T_0}}$	-	equilibrium constant for water thermolysis at temperature
$\boldsymbol{M_{CeO_2}}$	g/mol	molar mass of ceria
$\boldsymbol{M_{O_2}}$	g/mol	Molecular weight of oxygen
$\boldsymbol{M_{Ar}}$	g/mol	molecular weight of argon
$\boldsymbol{P_{H_2}}$	atm	partial pressure of hydrogen
$\boldsymbol{P_{H_2O}}$	atm	partial pressure of water
$\boldsymbol{P_{H_2Oout}}$	Atm	outlet partial pressure of water
$\boldsymbol{P_{H_2out}}$	Atm	outlet partial pressure of hydrogen
$\boldsymbol{P_{O_2}(\delta, T)}$	atm	oxygen partial pressure of a gas in equilibrium with a material at a nonostoichiometry of δ and temperature T
$\boldsymbol{P_{O_2in}}$	atm	oxygen partial pressure at the reactor inlet
$\boldsymbol{P_{O_2out}}$	atm	oxygen partial pressure at the reactor outlet
$\boldsymbol{P_{ref}}$	atm	reference pressure
$\boldsymbol{P_{tot}}$	atm	total pressure in reactor (atm)
$\boldsymbol{T_0}$	K	temperature of the reactor
$\boldsymbol{T_0}$	K	temperature of the reactor
$\boldsymbol{\dot{V}}$	mL/min	Volumetric flow rate
$\boldsymbol{V_M}$	L/mol	molar volume
$\boldsymbol{d\delta_{ox}/dt}$	min^{-1}	rate of change in oxygen nonstoichiometry during the oxidation half-cycle
$\boldsymbol{d\delta_{red}/dt}$	min^{-1}	rate of change in oxygen nonstoichiometry during the reduction half-cycle
$\boldsymbol{\frac{dV}{dt}}$	mL/min	volumetric flowrate of mercury into the pore
$\boldsymbol{k_B}$	J/K	Boltzmann constant
$\boldsymbol{m_{CeO_2}}$	g	mass of ceria
$\boldsymbol{n_{CeO_2}}$	mol	moles of ceria
$\boldsymbol{r_{O_2}}$	mol/min	rate of oxygen generation (or consumption)

$\boldsymbol{r_{pellet}}$	m	Radius of pellet
$\boldsymbol{r_{tube}}$	m	Radius of tube
$\boldsymbol{t_{ox}}$	min	oxidation half-cycle time
$\boldsymbol{t_{red}}$	min	reduction half-cycle time
$\boldsymbol{t_{tot}}$	min	total cycle time, $t_{tot} = t_{red} + t_{ox}$
$\boldsymbol{v_z}$	m/s	Face velocity of gas
$\boldsymbol{x_v}$	-	vacancy concentration
$\boldsymbol{r_s}$	Å	Shannon Radius of substituted cation
$\boldsymbol{r_{anion}}$	Å	Shannon Radius of anion
$\boldsymbol{r_{cation}}$	Å	Shannon Radius of cation
$\boldsymbol{r_h}$	Å	Shannon Radius of host cation
$\boldsymbol{r_o}$	Å	Shannon Radius of oxygen ion
$\boldsymbol{r_v}$	Å	Shannon Radius of oxygen vacancy
$\boldsymbol{\Delta H_{red}}$	kJ/mol	enthalpy of reduction
$\boldsymbol{\Delta S_{red}}$	J/mol/K	entropy of reduction
$\boldsymbol{\alpha_C}$	mol^{-1}	chemical expansion coefficient
$\boldsymbol{\alpha_T}$	ppm/°C	thermal expansion coefficient
$\boldsymbol{\delta_f}$	-	oxygen nonstoichiometry at end of the reduction half-cycle
$\boldsymbol{\delta_i}$	-	oxygen nonstoichiometry at initiation of the reduction half-cycle
$\boldsymbol{\varepsilon_{O_2,Ar}}$	-	intermolecular potential field between oxygen and argon
$\boldsymbol{\varepsilon_{O_2}}$	-	intermolecular potential field of oxygen
$\boldsymbol{\varepsilon_{Ar}}$	-	intermolecular potential field of argon
$\boldsymbol{\sigma_{O_2,Ar}}$	m	Collision diameter
$\boldsymbol{\sigma_{O_2}}$	J	Self attracting energy of oxygen
$\boldsymbol{\sigma_{Ar}}$	J	Self attracting energy of argon
$\boldsymbol{\sigma_D}$	m	hard sphere diameter of a gas molecule
$\boldsymbol{\chi_{H_2O}}$	-	mole fraction of water in inlet gas

$\boldsymbol{\chi_{H_2Oin}}$	-	inlet mole fraction of water
b	m^3/mol	excluded volume coefficient
I	-	1st order peak intensity
$\boldsymbol{\gamma}$	-	reciprocal space order parameter
$\boldsymbol{\Delta G^{\phi}}$	kJ/mol	standard free energy of reduction
$\boldsymbol{\Delta H^{\phi}}$	kJ/mol	standard enthalpy of reduction
$\boldsymbol{\Delta S^{\phi}}$	J/mol/K	standard entropy of reduction
$\boldsymbol{\Delta P}$	atm	pressure drop
$\boldsymbol{D}$	m	pore diameter
$\boldsymbol{Kn}$	-	Knudsen Number
$\boldsymbol{L}$	m	length
$\boldsymbol{Na}$	at/mol	Avogadro's number
$\boldsymbol{Q}$	-	characteristic hydrogen production rate for an incremental change in nonstoichiometry
$\boldsymbol{R}$	J/mol/K	ideal gas constant
$\boldsymbol{T}$	K	temperature
$\boldsymbol{d}$	m	pore diameter
$\boldsymbol{n}$	-	number of partitions
$\boldsymbol{t}$	min	time
$\boldsymbol{\Delta\delta}$	-	change in oxygen nonstoichiometry over a half-cycle
$\boldsymbol{\gamma}$	N/m	surface tension
$\boldsymbol{\delta}$	-	oxygen nonstoichiometry
$\boldsymbol{\eta}$	kg/s/m	fluid viscosity
$\boldsymbol{\theta}$	degrees	contact angle
$\boldsymbol{\lambda}$	m	mean free path
$\boldsymbol{\psi}$	-	extent of reaction of water
$\boldsymbol{\epsilon}$	-	strain

Chapter 1 Introduction

1.1 Motivation

Throughout the last century, our planet has experienced an unprecedented growth in energy consumption, fueled both by population increase and technological advances. Traditional means of energy production, such as fossil fuels and coal, have diminishing supplies and rising costs, and are damaging to the environment. These factors present the need for alternative energy technologies, which not only support our growing demand for energy, but do so in an environmentally friendly fashion. Since more energy from sunlight strikes the earth in ninety minutes than all of the energy consumed on the planet in one year, solar energy represents the largest potential energy source [10]. To date, efficient large-scale conversion and storage of solar energy has been elusive. The strategy investigated here is to use a thermochemical process in which a variable valence metal oxide is heated to high temperature using concentrated solar energy, inducing oxygen loss from the structure. The material is then cooled and exposed to steam and/or carbon dioxide. As dictated by thermodynamic considerations, the gases react with the reduced

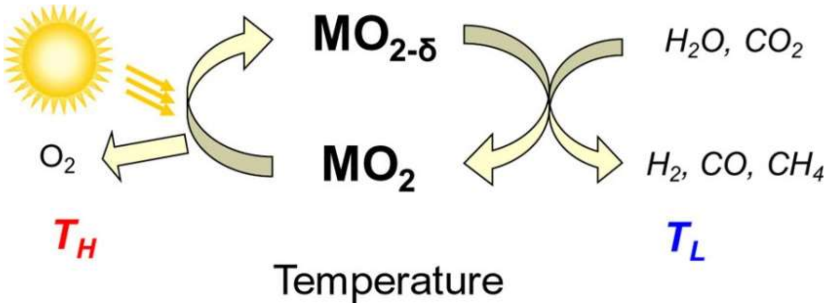

FIGURE 1.1-1 A thermochemical cycle that converts H_2O and CO_2 to chemical fuels by reduction and oxidation of a metal oxide using thermal energy as the input [4].

oxide to yield hydrogen and/or carbon monoxide as products. The reaction scheme is illustrated in **Figure 1.1-1**. Chemical fuels are particularly attractive because they incur minimal losses even when large quantities of energy are stored over long periods of time. Chemical fuels can be converted readily into electricity via a fuel cell or similar technology. Furthermore, high electrical power can be delivered continuously, and over long periods of time, in such a scenario because the functions of energy storage and electricity generation are decoupled. In comparison to photovoltaic or photocatalytic utilization of solar energy, a solar-thermal process has the benefit of inherently utilizing the entire solar spectrum in the photon-to-phonon conversion step.

1.2 Concentrated Solar Energy

During each of the past five years, concentrated solar energy has seen a growth rate between 30% and 60%. **Figure 1.2-1** from the International Energy Agency illustrates the cumulative gigawatts of concentrated solar power (CSP) capacity across the Earth. Two concentrated solar systems, Ivanpah in southern California and GEMASOLAR in Seville, Spain, have driven the bulk of this growth. The Ivanpah system in the Mojave Desert is composed of three towers that use concentrated solar energy to boil water and drive steam turbines. The systems produce an aggregate 377 megawatts of power, and can provide electricity to 140,000 surrounding homes during peak sunlight hours. Since these towers became operational in 2013, the U.S. CSP capacity has increased by 100%.

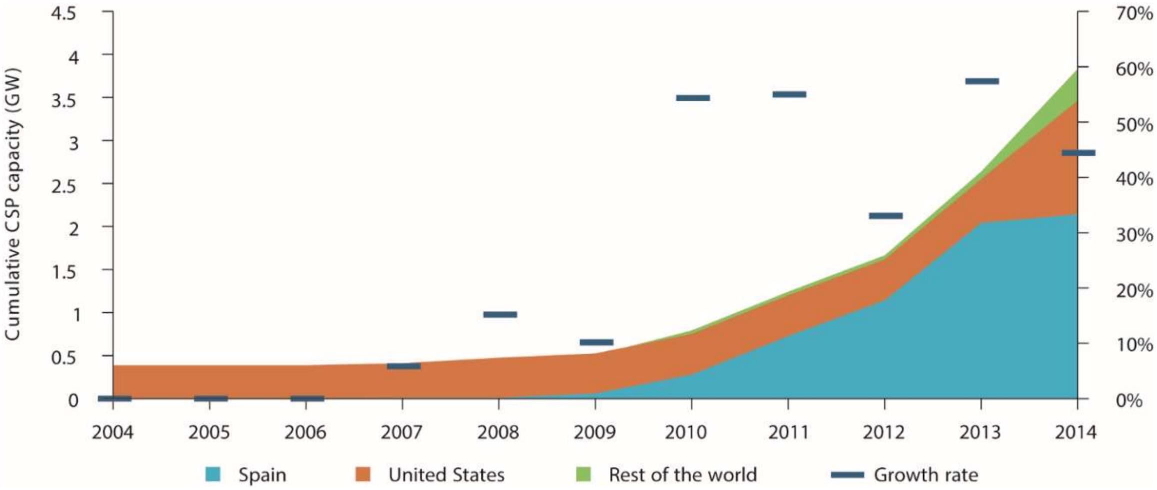

FIGURE 1.2-1 Cumulative concentrated solar power capacity across the globe for the past decade. Year over year rate of growth is denoted by the dashes.

The GEMASOLAR project in Spain the realization of a power plant that generates 110 GWh of electricity annually. The system, depicted in **Figure 1.2-2**, consists of a large field of heliostats (parabolic reflectors) which redirect and concentrate the sunlight at the top of the tower where the reactor is located. The plant has achieved continuous electricity production for a full week [9]. The solar energy is captured at a

FIGURE 1.2-1 GEMASOLAR Solar Electric Generating System in Seville, Spain [9].

1000-sun concentration, or about 500ºC, in a molten salt carrier; the carrier is then used to heat water to steam and operate a steam turbine. Due to the high heat capacity of the molten salt, the reactor is operable beyond daylight hours. Despite these major advancements in technology, however, reliable production of energy during non-daylight hours remains a challenge. For this reason, it is desirable to store the energy as a chemical fuel - which can be consumed when needed - rather than directly producing electricity, which must be consumed immediately or stored at an additional expense in batteries.

1.3 Survey of Reactor Demonstrations

Thermochemical fuel production was originally proposed by Nakamura in the late 1970's using the iron (II) oxide and iron (II, III) oxide redox pair [11]. At about the same time, the Gas Technology Institute in the U.S. investigated over 200 candidate cycles over the course of nine years. Most of these cycles were not pursued further do to a variety of reasons, including slow kinetics and unwanted byproducts that could not be easily separated. Each of these factors led to very low demonstrated efficiencies, despite high theoretical efficiencies. The three most promising reactions all had one trait in common: the thermal decomposition of sulfuric acid. Westinghouse was the first company to demonstrate water splitting from the waste heat of their nuclear plants using a hybrid sulfur process. Funding for the project, however, ceased due to a drop in oil prices around that time. Research resumed in 2002 when the U.S. included this (the coupling of thermochemical water splitting with the waste heat of nuclear power plants) as part of the plan to transition to a hydrogen economy. In addition, since the 1970's, in general, further developments in optics have allowed for higher temperatures to be achieved via concentration of solar energy. This has given new life to many cycles that were previously thought to be ineffective due to sluggish kinetics.

1.3.1 Zinc Oxide

Reactor demonstrations based on the zinc/zinc oxide thermochemical system have been pioneered at the Paul Scherrer Institute in Switzerland [8]. In the reduction reaction, zinc oxide is heated to 1800°C, at which point it evaporates to oxygen and zinc vapor. The gas mixture is then quenched at 10,000 °C/sec, preventing the recombination of zinc and oxygen and allowing the formation of solid zinc particles. The solid zinc particles are then oxidized with steam to re-form zinc oxide and produce hydrogen gas. Finally, the mixture is filtered and condensed to remove the zinc oxide nanoparticles and excess steam, respectively.

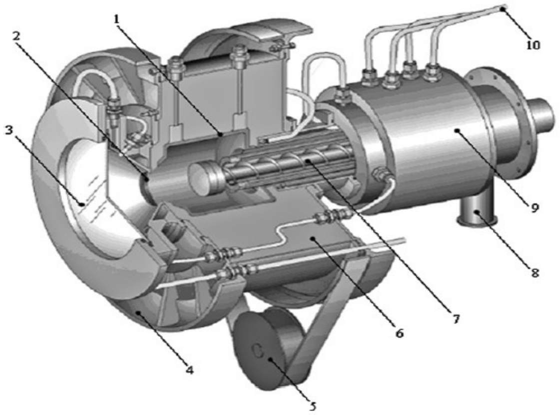

FIGURE 1.3-1 Schematic of ZIRRUS reactor: 1-cavity, 2-insolation, 3-quartz window, 4-rotating drum, 5-actuation, 6-insulation, 7-screw feeder, 8-product's outlet port, 9-rotary joint, 10-cooling fluids [8]

There is currently no reactor that solely accomplishes both of the half reactions. To study the reduction of zinc oxide, several groups at the Paul Scherrer Institute developed the ZIRRUS reactor. **Figure 1.3-1** illustrates the reactor in which solid zinc oxide is fed into a central cavity, where it is then exposed to concentrated solar radiation, evaporating and splitting the zinc oxide. When tested at varying temperatures up to 2300°C, it was found that higher temperatures yielded better reaction rates and conversion ratios. Peak fuel production was 12 g/min. for 9.1 kW of solar energy input. This yields a solar-to-fuel conversion ratio of 14.8% [8]. At much higher temperatures, the reactor's efficiency decreased due to re-radiative heat loss.

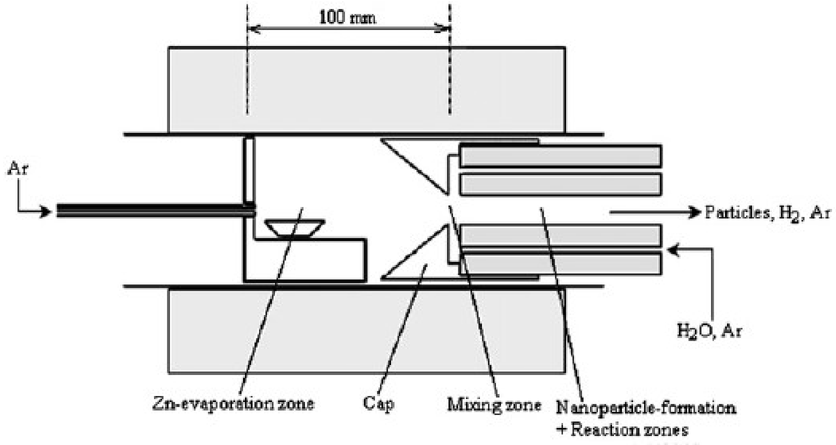

FIGURE 1.3-2 Schematic lab-scale reactor for Hydrolysis and formation of Zn nanoparticles [2]

To investigate the oxidation (fuel production) reaction, a prototype lab-scale reactor was developed by Aldo Steinfeld. Illustrated in **Figure 1.3-2**, this prototype consists of two sections. In the upstream zinc evaporation section, pure zinc is heated to 1000°C. The zinc vapor flows downstream with argon sweep gas, where it contacts steam heated to 200ºC fed in from the opposite end. The initial temperature decrease causes zinc nanoparticles to form, and subsequent interaction with the steam causes the nanoparticles to oxidize, resulting in hydrogen production. The highest chemical conversion of zinc to zinc oxide achieved has been 83% [2]. Since the steam initially reacts with the surface of the zinc nanoparticles, a zinc oxide layer forms on the surface, preventing further oxidation of the bulk zinc. To maintain a high conversion percentage in light of this effect, faster quenching rates of the zinc vapor are desirable in order to form smaller nanoparticles, which have a higher surface area to volume ratio. Unfortunately, faster quench times mean faster flow rates of the argon sweep gas, and shorter residence times in the reactor for the zinc to react.

1.3.2 Iron Oxide

In the 1970's, Nakamura investigated the FeO/Fe_3O_4 redox system for thermochemical cycling. The reduction reaction requires temperatures of over 2000K. In addition, the phase change from FeO in the cubic rock salt structure to Fe_3O_4 in the cubic spinel structure incurred a large energy penalty. After the turn of the century, Kodama discovered that supporting the iron oxide on cubic yttria stabilized zirconia (YSZ) allowed the reduction reaction to occur at more modest temperatures of around 1400K and improved the kinetics of the reaction [12]. Mechanistically, as the Fe^{3+} ions reduce to Fe^{2+}, they enter into the cubic YSZ lattice, allowing the Fe_3O_4 to remain in the cubic spinel structure. Upon oxidation, the iron atoms exsolve from the YSZ lattice to reform Fe_3O_4 on the surface.

Laboratory-scale tests have shown that low conversion is still the major challenge. Samples were prepared with about 10wt% iron oxide on an 8% YSZ substrate. It was found that stabilizing the zirconia with 8% yttria versus 3% yttria prevented sintering from occurring over 32 hours. Maximum conversion of Fe_3O_4 was about 60% at reaction temperatures of 1600°C. At higher temperatures, the YSZ substrate began to change to the tetragonal phase, resulting in a severe energy penalty. At lower temperatures (1400°C), which are more feasible for thermochemical reactors, conversion was only around 30-45% [13].

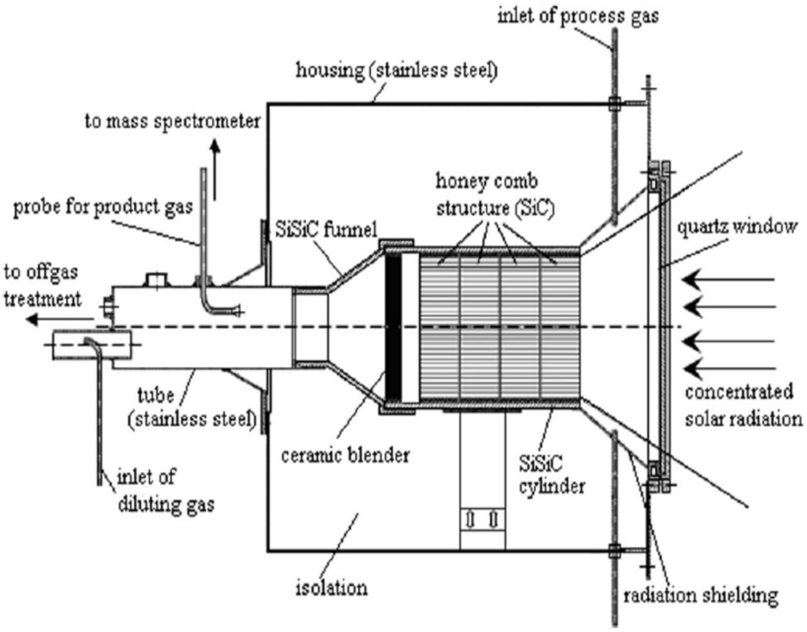

FIGURE 1.3-3 Schematic of solar reactor with multi-channeled honeycomb ceramic support [5]

A solar prototype reactor was developed in 2006 at the German Aerospace center in Cologne, Germany, and is depicted in **Figure 1.3-3**. It features a honeycomb monolith support, modeled after catalytic converters. In this prototype, cycles are operated between 800°C and 1200°C. During heating, sweep gas flows through the honeycomb-like reactor core, purging oxygen from the system. Upon cooling, steam is swept through the reactor, which oxidizes the iron oxide on the support. One inherent problem with this design is the batch-style production of hydrogen. Much of the efficiency is lost while waiting for the system to cool down. One proposal suggests solving this problem with two sister reactors built side by side and operating out of phase with one another. In this way, one will heat while the other cools and hours of sunlight are not wasted.

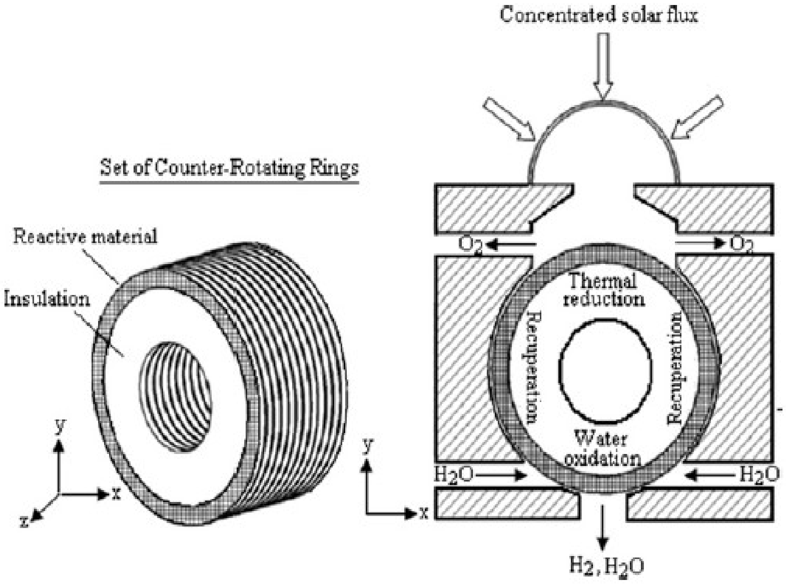

FIGURE 1.3-4 Schematic of the counter-rotating ring reactor [1]

To address the solid-state heat recovery and continuous production of hydrogen, Sandia National Laboratories developed a Counter-Rotating Ring Reactor, whose schematic is depicted in **Figure 1.3-4**. In this design, compact disks of YSZ, with iron oxide deposited on the edges, are stacked on top of one another. Concentrated solar radiation enters the reactor radially inwards towards the stack of disks, heating one side up to the desired temperature. The backside of the core is unexposed to the solar energy and remains cool, at an appropriate temperature for the oxidation reaction to occur. Each disk spins in an opposite direction to the ones above and below so that, as they rotate, they help to heat and cool one another, thereby conserving heat. This system was predicted to have 30% solar-to-fuel energy conversion, but was ultimately abandoned due to due to mechanical failure of the disks. The complex heat recovery system and thermal gradients caused the reactor core to fail.

1.3.3 Cerium Oxide

Recently, Chueh et al. demonstrated the thermochemical cycling of cerium dioxide in a solar cavity-receiver reactor [4]. **Figure 1.3-5** illustrates the reactor schematic. Ceria exists in the fluorite structure, and can undergo significant reduction

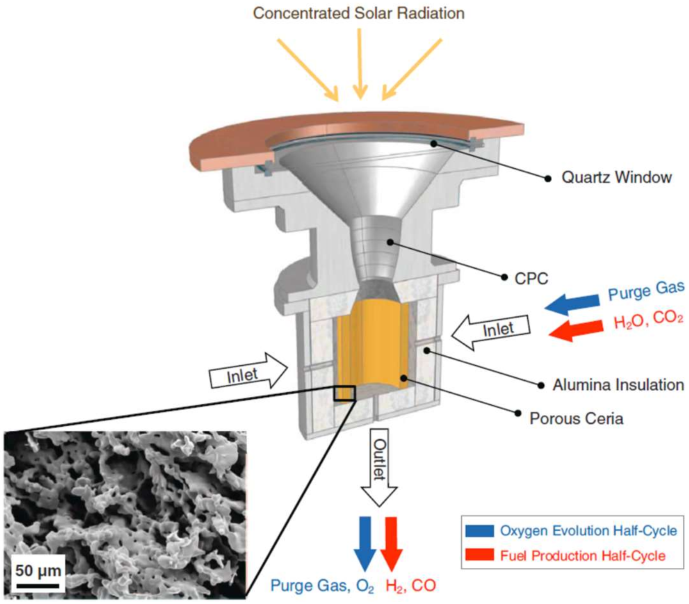

FIGURE 1.3-5 Schematic of the solar cavity receiver and operation on a porous ceria annulus [4].

without a phase change under high temperatures. This results in chemical nonstoichiometry via oxygen vacancies throughout the lattice. The material can then be exposed to either water or carbon dioxide at a lower temperature to refill those vacancies, producing either hydrogen or carbon monoxide, respectively. This allows for several advantages over the previously-discussed material systems. The oxide used for the reaction is unsupported by a second oxide. In the case of the iron supported on YSZ systems, thermal energy is wasted in heating up the YSZ, which does not directly contribute to the oxidation or reduction reactions. With ceria, due to its high oxygen ion diffusivity, oxygen atoms that fill vacancies on the surface are quickly transported to the bulk, making room for further surface adsorption and reaction. This avoids the isolating effect of the outer oxide layer in the zinc system. Despite these significant advancements to the reaction mechanics, however, they were only able to demonstrate a 1% solar-to-fuel efficiency. There is much room for improvement in this technology, both in the material development and reactor design, in order to realize an efficient means of converting solar energy to chemical fuels. This work aims to create a theoretical framework for rational selection and design of materials and of reactor configurations.

Chapter 2 Theory and Background

2.1 Thermochemical Cycling Strategies

2.1.1 Two-Temperature Cycling

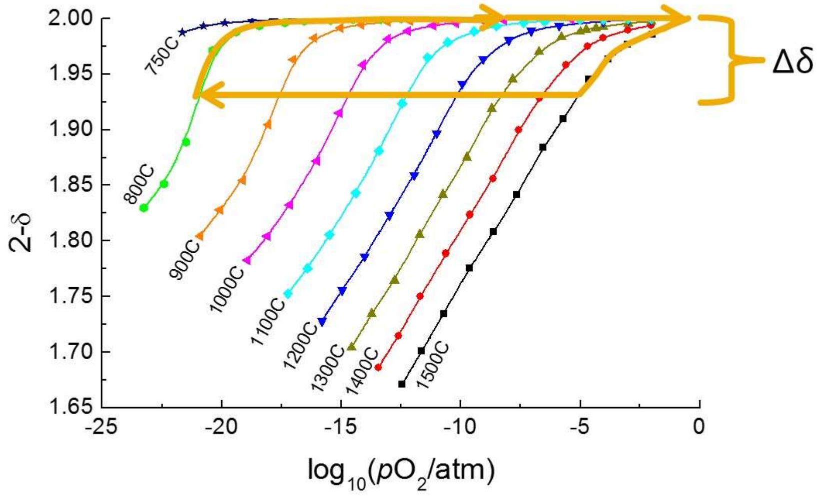

FIGURE 2.1-1 Schematic of the two-temperature thermochemical cycle on ceria when reduced at 1500 ºC under 10 ppm O_2 and oxidized under 20% steam at 800 ºC

Ceria exhibits the largest nonstoichiometry change when subjected to two temperature cycling. By leveraging its rapid kinetics at low temperature, the material can be fully reoxidized, allowing every vacancy that was formed during reduction to contribute to the oxidation process. A schematic of this cycle is depicted in **Figure 2.1-1**. Ceria is first reduced under 10 ppm O2 in a balance of argon at 1500 C and then the system is quickly quenched to 800 C. The gas atmosphere is changed to 20% steam in a balance argon and the system is allowed to reach equilibrium. The temperature is then quickly ramped to 1500 C while the gas atmosphere is switched back to 10 ppm O2 in a balance of argon, thus completing the cycle.

The nonstoichiometry achieved represents the fraction of oxygen atoms that leave the structure. Using the total moles of oxide we can determine the exact number of oxygen vacancies formed. Each oxygen vacancy will produce one hydrogen molecule upon water splitting. The volumetric amount of hydrogen produced is then calculated under standard temperature and pressure. For this specific cycle, one expects 8.66 mL/g of hydrogen produced. This is just over double (4.19 mL/g) the expected yield for one complete cycle of isothermal pressure-swing cycling discussed in detail in the next section.

2.1.2 Pressure-Swing Cycling

Water splitting for fuel production via isothermal pressure-swing cycling has recently emerged as a means of converting solar heat to a storable medium [14]. For the generation of hydrogen, the process involves the high temperature reduction of a variable valence oxide under an inert gas of low oxygen content followed by oxidation by steam at the same high temperature. Due to thermolysis, the higher the temperature the greater the oxidizing power of the steam, providing a means of converting thermal energy to chemical energy. In comparison to a more conventional temperature-swing cycle, the isothermal, pressure-swing cycle offers the potential for greater efficiency because the need for solid state heat recovery is eliminated, although the demands on gas-phase heat recovery are increased. To date, isothermal, pressure-swing process has been demonstrated only using ceria. **Figure 2.1-2** illustrates this cycle.

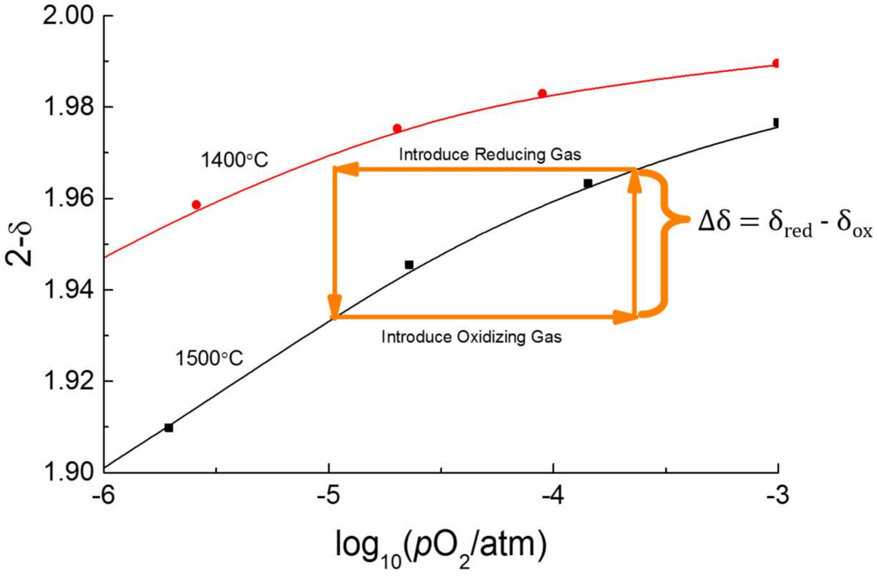

FIGURE 2.1-2 Schematic of the isothermal pressure-swing cycle on ceria oxidized with 20% steam and reduced in 10ppm O_2 at 1500ºC overlaid on the digitized nonstoichiometry data taken by Panlener et al.

2.2 Experimental Measurement of Material Thermodynamics

Thermogravimetric analysis (TGA) is a technique that allows for the determination of small mass changes in a sample when exposed to a chosen temperature and gas atmosphere. In this work, ceria derivatives were analyzed in a thermogravimeter (TG) so that the nonstoichiometry behavior could be understood and compared to known materials before thermochemical cycling. In this process, the synthesized porous pellets are placed in the TG chamber and sealed. A desired partial pressure of oxygen and temperature are chosen to induce reduction of the sample. Once the sample reaches equilibrium, the mass loss reported by the TG indicates the amount of oxygen lost in the sample and ultimately the nonstoichiometry. By specifying a full range of oxygen partial pressures and temperatures, the full nonstoichiometry behavior can be determined.

Digital mass flow controllers deliver ultra high purity (UHP) gases to the sample chamber, which are vented to exhaust. To achieve the oxidizing conditions, a 10% oxygen mixture with argon balance is diluted with pure argon. To achieve lower oxygen partial pressures, hydrogen concentrations of 0.1% to 3% in balance argon are fully humidified at room temperature. Since the temperature inside the TG chamber is known, the oxygen partial pressure can be calculated from the known thermodynamic equilibrium of water formation.

For a given measurement program, a background correction is performed by running the experiment without a sample. The mass loss indicated during this background scan indicates the buoyancy effect from heating. The mass loss is then subtracted from the results of the experiment to negate this buoyancy effect.

2.2.1 Theory

For each material, the nonstoichiometry data was collected via thermogravimetric analysis. Specifically, the gas compositions used were 10% O_2, 1% O_2, 0.1% O_2, 1000 ppm O_2, 100 ppm O_2, 10 ppm O_2, 0.03% H_2, 1% H_2, and 3% H_2. All of the gas compositions were in balance with argon. The hydrogen mixtures flowed through a humidifier at room temperature, which introduced about 2% H_2O to the mixture. The oxygen partial pressure could then be determined at each temperature according to the equilibrium of the thermolysis reaction, depicted below.

$$K_{H_2O}(T) = \frac{p_{H_2}\sqrt{p_{O_2}}}{p_{H_2O}} \qquad 2.2.1\text{-}1$$

Once the measured nonstoichiometric behavior is compiled in a similar manner to **Figure 2.2-1** it is possible to extract the entropy and enthalpy for the reduction reaction

$$\lim_{\varepsilon\to 0}\frac{2}{\varepsilon}MO_{2-\delta} \Leftrightarrow \frac{2}{\varepsilon}MO_{2-\delta-\varepsilon} + O_2 \qquad 2.2.1\text{-}2$$

by noting the equilibrium constant

$$K_{redox}(\delta) = P_{O_2}(\delta) \qquad 2.2.1\text{-}3$$

and its relationship to the thermodynamic quantities

$$\Delta G^{\phi}_{redox}(T,\delta) = RTln(K_{redox}) = \Delta H^{\phi}_{redox}(\delta) - T\Delta S^{\phi}_{redox}(\delta) \qquad 2.2.1\text{-}4$$

Combining **Equations 2.2.1-3** and **2.2.1-4** yields

$$\ln\big(P_{O_2}(\delta)\big) = \frac{\Delta H^{\phi}(\delta)}{RT} - \frac{\Delta S^{\phi}(\delta)}{R} \qquad 2.2.1\text{-}5$$

and thus an iso-stoichiometric (fixed δ) plot of $\ln P_{O_2}$ vs. $1/T$ yields $\Delta H^{\phi}(\delta)$ from its slope and $\Delta S^{\phi}(\delta)$ from its intercept, where the superscript ϕ indicates the standard state. Once the enthalpy and entropy of the reduction reaction are known for all of the relevant nonstoichiometries, the nonstoichiometry of a material can be determined for any desired oxygen partial pressure and temperature.

When generating the Arrhenius plots it is necessary to interpolate the isotherms in the collected data for each fixed nonstoichiometry. The nonstoichiometries over which to perform the interpolation are chosen such that one point is always experimentally determined. This allows for better continuity in the enthalpy and entropy data. An example of this interpolation and associated Arrhenius plot are detailed in **Figure 4.2-1** for 10% praseodymium doped ceria.

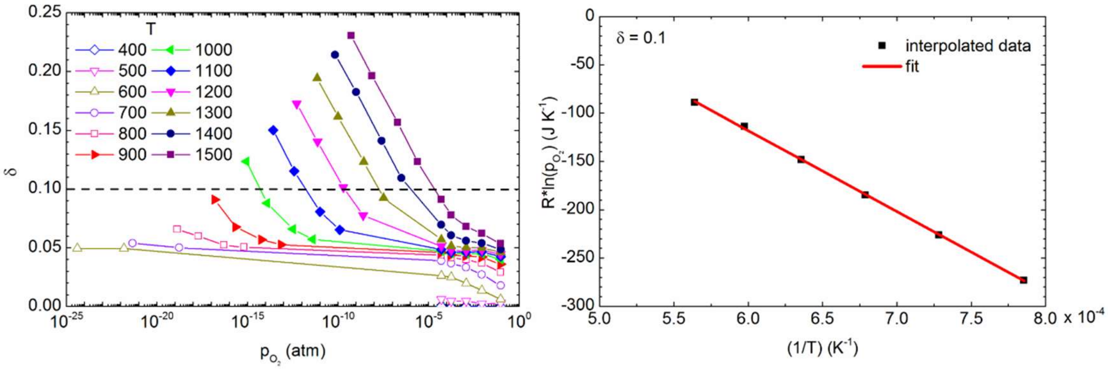

Figure 2.2-1 10% praseodymium doped ceria nonstoichiometric data showing the interpolated points (left) and Arrhenius plot (right) based of the nonstoichiometry of 0.1 on the 1200°C isotherm.

2.3 Thermochemical Cycling Apparatus

2.3.1 Temperature-Swing and Pressure-Swing Cycling

In order to evaluate thermochemical cycling of the materials, an in-house, lab-scale thermochemical reactor was constructed. The cycling was performed in an infrared gold image furnace (ULVAC RHL-E44VHT). The samples were each formed into a cylindrical shape such that they fit snugly within a 1/4" ID alumina tube placed in the furnace, and through which the reduction or oxidation gas was flowed. The furnace temperature was controlled by an alumina-sheathed S-type thermocouple in contact with the downstream end of the sample.

Four digital mass flow controllers delivered 10 ppm O_2 in an argon gas to the furnace during the reduction half-cycle. Oxidation was carried out using an atmosphere of 20% H_2O in argon. This was achieved by passing dry argon through a bubbler inside of a temperature-controlled oven at 60°C prior to its delivery to the furnace. Gas flow rates were calibrated by a primary air flow calibrator, and were referenced to 0°C and 1 atm. All reduction steps were performed using flow rates between 200 sccm and 1000 sccm (standard cubic centimeters per minute). The oxidation gas flow rates varied from 100 sccm to 500 sccm. Gases were obtained at UHP purity from Air Liquide.

Downstream of the furnace, the gas was passed through a condenser held at 1°C in order to remove H_2O, and was then sampled by a quadrupole mass spectrometer (Pfeiffer Thermostar GSD301T2) every 6.5 seconds. Quantification of the mass spectrometry data was achieved by a five- or six-point calibration with known compositions of hydrogen and oxygen in argon. The operational schematic of the thermochemical test station is detailed at the end of this section in **Figure 2.3-1**.

Isothermal cycling was performed by loading synthesized porous pellets into a horizontal alumina tube reactor (9.5 mm diameter), which was then placed inside of a high-temperature electric furnace (Lindberg/Blue M STF54434C with controller model CC59256PCOMC). The furnace was ramped to 1500 °C (at 10 °C min^{-1}) and held at 1500 °C for the duration of the experiments. Calibration of the temperature within the alumina tube with an external thermocouple indicated that the temperature in the alumina tube at the position of the sample was uniform at 1500 ± 2 °C.

2.3.2 Thermolysis Reaction in Pressure-Swing Cycling

To induce recombination of hydrogen and oxygen produced by water thermolysis within the furnace (distinct from hydrogen production via the presence of the reactive oxide), a hollow cylinder of Rh-decorated ceria, shaped such that the thermocouple could pass through, was placed at the downstream end of the furnace where the temperature was 600 – 800 °C.

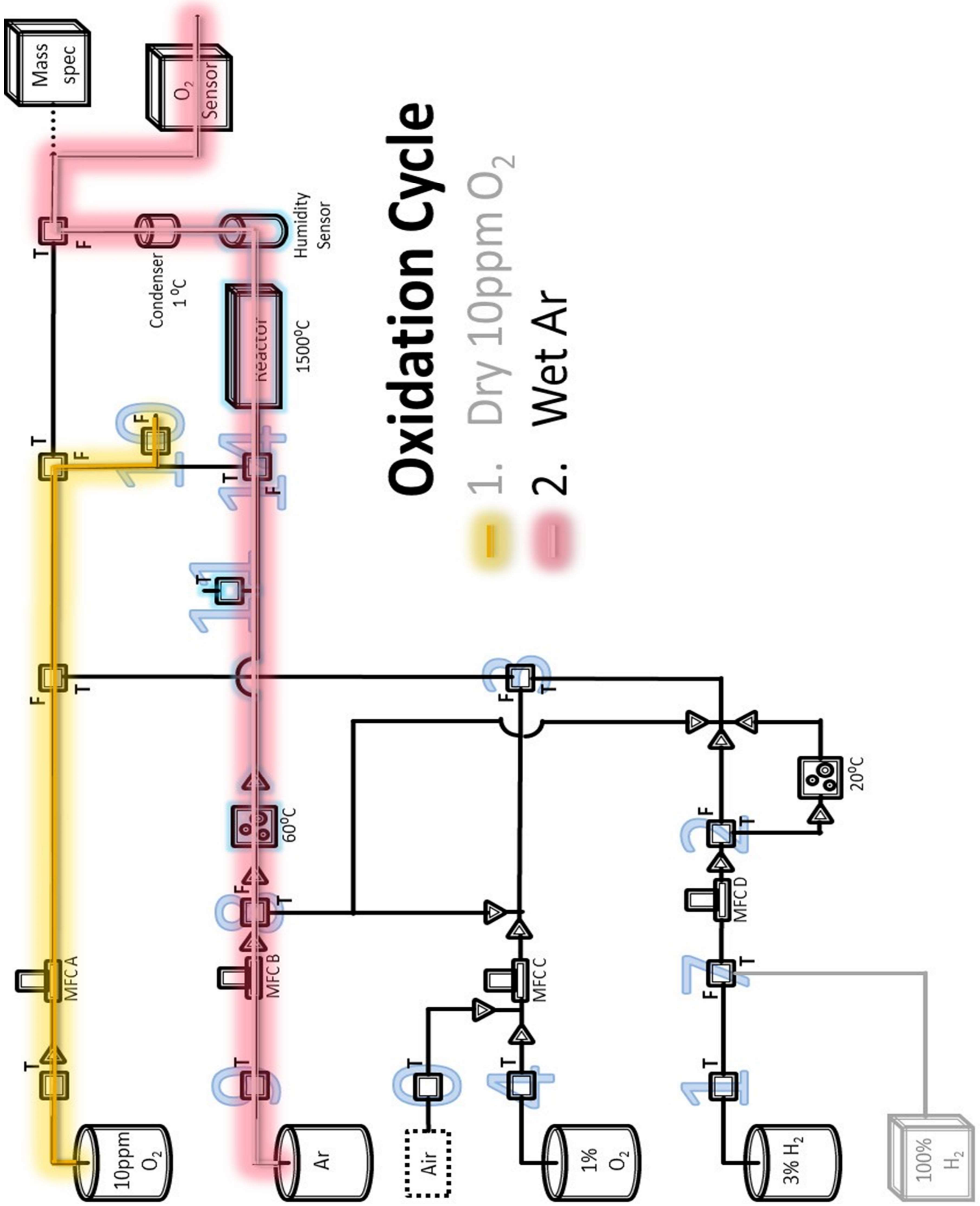

FIGURE 2.3-1 Operational Schematic of the thermochemical test station, with squares indicating solenoid valves. The highlighted gas lines indicate the flow of gas during the oxidation cycle or hydrogen production step. To switch to the reduction step, the state of valves 10, 11, and 14 are changed, with no need to adjust the flowrates.

2.3.3 Thermal Management in the Infrared Furnace

An additional thermocouple (of the same type) was placed in contact with the upstream end of the sample. On the inside of the alumina tube, 3 cm was lined with Pt foil (99.9% purity, 0.025 mm thick, Alfa Aesar) centered on the sample to ensure blackbody heating of the sample and thermocouples. The position of the sample within the furnace was adjusted such that the temperature difference between the two thermocouples was less than 7°C during reduction.

The rapid temperature changes obtainable with the IR furnace allow two-temperature cycling experiments to be performed quickly enough to limit the reaction of material with residual oxygen while cooling the reactor to oxidation temperature. However, due to the tightly focused heating zone of the IR furnace and the absorption/release of heat during reaction, accurate temperature control was a significant challenge. In particular, the measured temperatures, as well as the temperature difference between the two thermocouples in contact with either end of the sample, depended on the temperature of the reactor, the position of the sample within the reactor, the flow rate of gas through the reactor, and the composition of the gas flowing through the reactor. To address the issue of temperature difference between the furnace set temperature and that of the sample, the effective sample temperature was determined by calibration to the well-established thermodynamic data of ceria. Specifically, the true sample temperature was established using the measured oxygen partial pressure, the quantity of oxygen released from the sample, and the expected oxygen release. Effects on gas production profiles due to temperature inhomogeneities across the sample were determined to be small enough to be ignored, and hereafter the calibrated and positionally averaged temperature is quoted. To ensure that reported results would reflect steady-state behavior, the materials were subjected to one day of high-temperature experimentation prior to the collection of the data.

2.3.4 Relevant Experimental Parameters for Thermochemical Experiments

It will become evident in the following sections, that there are two different rate-limiting behaviors that materials can exhibit during thermochemical experiments. In order to properly characterize which of these phenomena governs the fuel production rate a number of parameters must be reported with each experiment. These include sample mass and the temperature and oxygen partial pressure at which the oxidation and reduction steps occur. This will allow for determination of the theoretical mass-normalized fuel production per cycle. The porosity, gas flow rate, tube diameter (gas velocity), and sample cross-sectional area must also be reported so that the molar specific flow rates and linear velocities face can be calculated. The porosity helps to characterize the gas access to the sample.

2.4 Influence of Material Thermodynamics on Fuel Production Rate

2.4.1 Introduction

A significant aspect of pressure-swing cycling, particularly in the case of ceria, is the thermodynamic advantage of operating at high temperature, with fuel productivity increasing monotonically with temperature. High temperature operation, in turn, leads to extremely rapid material kinetics, in terms of both surface reaction rate and bulk oxygen diffusion. Rapid diffusion and surface reaction then raise the intriguing possibility that the overall fuel production rate may be limited not by these material kinetic factors (which can then be considered to be infinitely fast), but rather by the thermodynamic capacity of the reactant gas to modify the oxide oxidation state. Indeed, it has been suggested that even during the rapid heating step in a typical temperature-swing cycle (as high as 1000 °C min^{-1}) the oxide can maintain continuous thermal and chemical equilibrium with the gas throughout much of the initial temperature ramp, providing a precedent for gas-phase limited behavior [4].

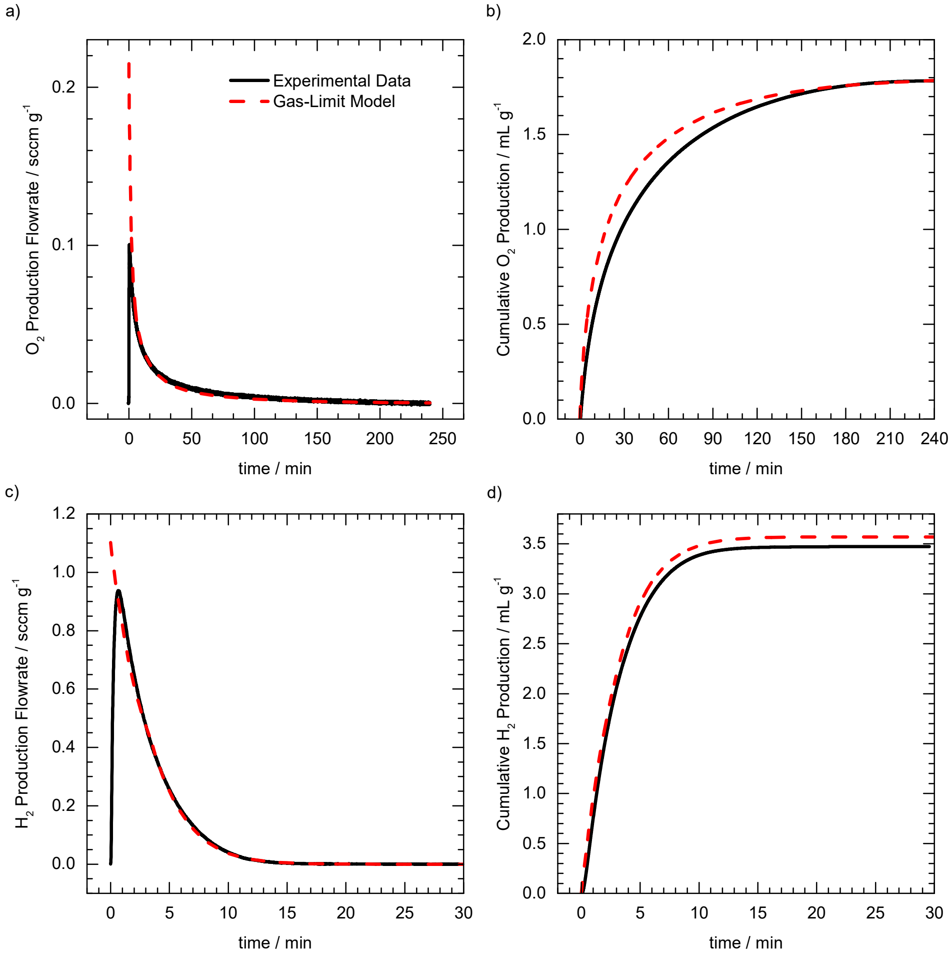

FIGURE 2.4-1 Comparison of an isothermal pressure-swing cycle at 1500 °C with (a-b) oxygen production during reduction of 0.51 g ceria by 467 sccm flow of 10 ppm O_2 in Ar, and (c-d) hydrogen production during oxidation by 280 sccm flow of 20% H_2O in Ar to the calculated production profiles by the gas-phase limited model are shown by red dashed curves. Instantaneous flowrate profiles are given in (a) and (c), and cumulative production profiles are given in (b) and (d). Due to the presence of a low level of air leak into the reactor, the calculated profiles assume an O_2 concentration of 14.7 ppm during reduction.

Such rapid material kinetics create an additional motivation, beyond those associated with heat recovery strategies, to pursue isothermal pressure-swing cycling, despite the typically lower fuel productivity per cycle relative to the temperature-swing approach, a criticism noted in the recent literature [15].

To better understand the gas phase limited regime, a numerical model was developed, to allow quantitative prediction of the rate of fuel production, by assuming the sample is always at uniform nonstoichiometry. Comparison against experimental data reveals that, under appropriate conditions, the model correctly predicts gas release profiles for ceria illustrated in **Figure 2.4-1**.

2.4.2 Thermokinetic Limit Derivation

The physical situation of interest is illustrated schematically in **Figure 6.2-1**. A block of porous, reactive oxide, in this case ceria, is held at a fixed temperature, T (set here at 1500 °C) and exposed sequentially to reducing and oxidizing atmospheres, with oxygen non-stoichiometry values cycling schematically between the represented states. Consistent with the notion of infinitely rapid material kinetics, the oxygen partial pressure at a given time, t, of the gas coming out of the reactor, $P_{O_2,out}(t)$, is taken to be equal to the oxygen partial pressure of a gas in equilibrium with the material, $P_{O_2}(\delta, T)$, at its nonstoichiometry, $\delta(t)$. In other words, the oxide releases oxygen instantaneously up to the thermodynamic capacity of the gas flowing across the sample, regardless of the kinetic properties of the material. The sample is assumed to be small enough that no stoichiometry gradient exists across it, and the gas flow through the reactor is assumed to be characterized by plug flow.

(a) reduction conditions

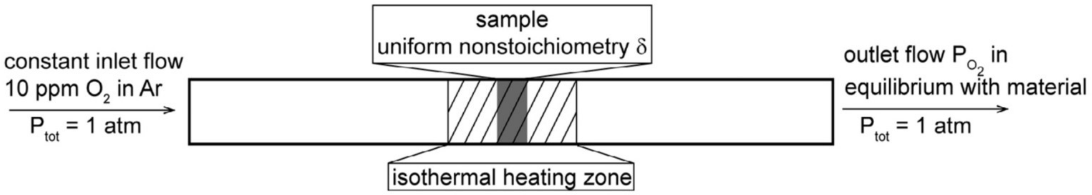

(b) oxidation conditions

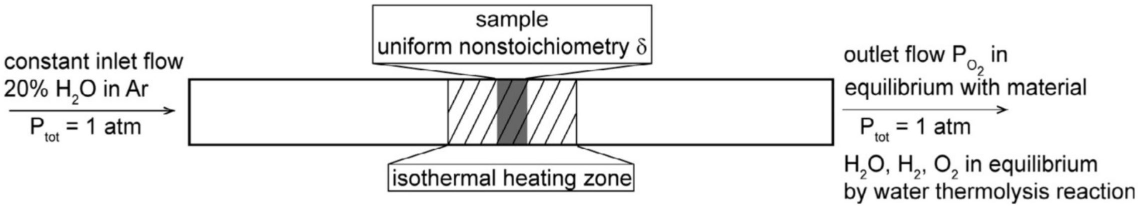

FIGURE 2.4-2 Schematic of the thermochemical reactor under gas phase limitation a) reduction conditions and b) oxidation conditions [16].

2.4.2.1 Reduction

The behavior under reduction is considered first [17]. In this step, the material is exposed to an oxygen-poor gas, supplied at an inlet flow rate of F_{red}. This exposure induces reduction according to reaction

$$\frac{1}{\Delta\delta}CeO_{2-\delta_i} \rightarrow \frac{1}{\Delta\delta}CeO_{2-\delta_f} + \frac{1}{2}O_2 \tag{2.4.2-1}$$

where $\Delta\delta = \delta_f - \delta_i$, and δ_i and δ_f are the oxygen non-stoichiometry values at the initiation and completion of the reduction step. Oxygen mass balance across the reactor requires

$$\boldsymbol{F_{O_2out} - F_{O_2in} = r_{O_2}} \qquad \textbf{2.4.2-2}$$

where F_{O_2in} and F_{O_2out} are the molar flow rates of oxygen into and out of the reactor at a specified time, and r_{O_2} is the rate of oxygen generation by the sample. Given the reduction reaction in **Equation 2.4.2-1**, the latter term is given by

$$\boldsymbol{r_{O_2} = \frac{n_{CeO_{2-x}}}{2}\frac{d\delta_{red}}{dt}} \qquad \textbf{2.4.2-3}$$

where $n_{CeO_{2-x}}$ is the number of moles of metal oxide inside the reactor (x is arbitrary for this expression) and $d\delta_{red}/dt$ is the rate of change of oxygen stoichiometry in the metal oxide, denoted with red to indicate reduction. The molar flow rate of oxygen into the reactor is fixed experimentally as

$$\boldsymbol{F_{O_2in} = \frac{P_{O_2in}}{P_{tot}}F_{red}} \qquad \textbf{2.4.2-4}$$

where P_{O_2in} is the inlet oxygen partial pressure, and P_{tot} is the total pressure, set at 1 atm. F_{red} is the total inlet molar flow rate of gas during reduction (an inert carrier gas with a known, small quantity of oxygen) and is constant over time.

Under the assumption that the oxygen partial pressure of the outlet stream is determined by the nonstoichiometry of the material, the molar flow rate of oxygen out of the reactor is simply

$$\boldsymbol{F_{O_2out} = \frac{P_{O_2}(\delta, T_0)}{P_{tot}}F_{out}} \qquad \textbf{2.4.2-5}$$

where $P_{\mathrm{O}_2}(\delta, T_0)$ is the equilibrium oxygen partial pressure of a gas in equilibrium with the metal oxide at a nonstoichiometry of δ. The total outlet flow rate, F_{out}, will be the sum of the inlet flow rate, F_{red}, and the oxygen generated within the reactor, r_{O_2}, as given in **Equation 2.4.2-3**. With **Equation 2.4.2-5** this implies

$$\boldsymbol{F_{O_2out} = \frac{P_{O_2}(\delta,T_0)}{P_{tot}}\left(F_{red} + \frac{n_{CeO_2}}{2}\frac{d\delta_{red}}{dt}\right)} \qquad \textbf{2.4.2-6}$$

Combining **Equations 2.4.2-2** through **2.4.2-5** and solving for $d\delta_{red}/dt$ gives

$$\boldsymbol{\frac{d\delta_{red}}{dt} = \frac{2F_{red}}{n_{CeO_2}}\frac{\left(P_{O_2}(\delta,T_0)-P_{O_2in}\right)}{\left(P_{tot}-P_{O_2}(\delta,T_0)\right)}} \qquad \textbf{2.4.2-7}$$

in which the only unknown is $P_{O_2}(\delta, T_0)$. If the thermodynamics of reduction of the material, that is, the enthalpy and entropy of the reduction reaction expressed in **Equation 2.4.2-1** ($\Delta H_{red}(\delta)$ and $\Delta S_{red}(\delta)$, respectively) have been determined, then $P_{O_2}(\delta, T_0)$ can be calculated according to

$$\boldsymbol{\frac{1}{2}ln\left(P_{O_2}(\delta,T)\right) = \frac{-\Delta H_{red}(\delta)+T\Delta S_{red}(\delta)}{RT}} \qquad \textbf{2.4.2-8}$$

With **Equations 2.4.2-6** and **2.4.2-7** and knowledge of $\Delta H_{red}(\delta)$ and $\Delta S_{red}(\delta)$, the evolution of nonstoichiometry during reduction then can be determined as a function of time via an iterative treatment. The volumetric oxygen production profile (the relevant quantity typically detected by measurement of the outlet gas stream composition) is readily computed from the rate of change in nonstoichiometry. Reported as a volumetric flowrate per gram of oxide, it is given by

$$\boldsymbol{\dot{V}_{O_2}(t) = \frac{V_M}{2M_{CeO_2}}\frac{d\delta_{red}}{dt}} \qquad \textbf{2.4.2-9}$$

where V_M is the molar volume of oxygen and M_{CeO_2} is the molecular mass of ceria.

2.4.2.2 Oxidation

We now turn to the behavior under oxidation [17], **Figure 2.4-2b**. In this case, the oxidation of the metal oxide is defined by the reaction

$$\frac{1}{\Delta\delta}CeO_{2-\delta_i} + H_2O \rightarrow \frac{1}{\Delta\delta}CeO_{2-\delta_f} + H_2 \qquad \textbf{2.4.2-10}$$

In addition, the water in the reactor can undergo thermolysis according to

$$H_2O \rightarrow \frac{1}{2}O_2 + H_2 \qquad \textbf{2.4.2-11}$$

where K_{H_2O,T_0} is the equilibrium constant for the water thermolysis reaction at the reactor temperature T_0. Thus, characterization of the reactor in the fuel production step will require material balances on water, hydrogen, and oxygen similar to those expressed in **Equation 2.4.2-2**. The inlet flow of gas is delivered at a constant flow rate, F_{ox}, and is a mixture of only inert gas and water with a fixed mole fraction of water, χ_{H_2O}, such that

$$F_{H_2Oin} = \chi_{H_2Oin}F_{ox} \qquad \textbf{2.4.2-12}$$

where F_{H_2Oin} is the total inlet molar flow rate of water during oxidation.

After entering the reactor, water is consumed both by reaction with the oxide and by thermolysis. The combined extent of consumption is designated ψ, the extent of reaction of water. With ψ so defined, the flowrate of water out of the reactor becomes

$$F_{H_2Oout} = (1-\psi)F_{H_2Oin} \qquad \textbf{2.4.2-13}$$

Because consumption of water by either **Equation 2.4.2-10** (oxide oxidation) or **Equation 2.4.2-11** (thermolysis) directly results in generation of hydrogen, the flowrate of hydrogen out of the reactor is

$$F_{H_2out} = \psi F_{H_2Oin} \qquad \textbf{2.4.2-14}$$

In the case of oxygen, generation occurs via **Equation 2.4.2-11**, but due to consumption of water via **Equation 2.4.2-10**, the amount of oxygen flowing out of the reactor is less than what would be expected from thermolysis alone. Balancing these factors yields

$$F_{O_2out} = \frac{\psi}{2} F_{H_2Oin} + \frac{n_{CeO_2}}{2} \frac{d\delta_{ox}}{dt} \qquad \textbf{2.4.2-15}$$

The total molar flowrate out of the reactor, F_{out}, is simply the total coming in, modified by the additional flows due to oxygen and hydrogen production and the loss due to water consumption:

$$F_{out} = F_{ox} + F_{O_2out} + F_{H_2out} - \psi F_{H_2Oin} = F_{ox} + F_{O_2out} \qquad \textbf{2.4.2-16}$$

Inserting the definition of F_{O_2out} given in **Equation 2.4.2-15** into the above yields

$$F_{out} = F_{ox} + \frac{\psi}{2} F_{H_2Oin} + \frac{n_{CeO_2}}{2} \frac{d\delta_{ox}}{dt} \qquad \textbf{2.4.2-17}$$

The unknown quantity F_{out} is eliminated by recognizing that, as before, in the limit of infinitely fast material kinetics, the oxygen partial pressure of the outlet stream is determined by the nonstoichiometry of the material, giving

$$F_{O_2out} = \frac{p_{O_2}(\delta, T_0)}{P_{tot}} F_{out} \qquad \textbf{2.4.2-18}$$

Inserting this and **Equation 2.4.2-12**, into **Equation 2.4.2-17**, and solving for $d\delta_{ox}/dt$ yields

$$\frac{d\delta_{ox}}{dt} = \frac{F_{ox}}{n_{CeO_2}} \frac{\left(2P_{O_2}(\delta,T_0) - \psi\chi_{H_2O}\left(P_{tot} - P_{O_2}(\delta,T_0)\right)\right)}{\left(P_{tot} - P_{O_2}(\delta,T_0)\right)} \qquad \textbf{2.4.2-19}$$

which is analogous to **Equation 2.4.1-16** for the rate of nonstoichiometry change under reducing conditions. However, the expression for $d\delta_{ox}/dt$ in **Equation 2.4.2-19** contains the additional unknown ψ. This quantity can be determined given the additional constraint that the outlet gases must be at equilibrium with the water thermolysis reaction and thus

$$K_{H_2O,T} = \frac{P_{H_2out}P_{O_2}(\delta,T_0)^{\frac{1}{2}}}{P_{H_2Oout}P_{ref}^{\frac{1}{2}}} = \left(\frac{\psi}{1-\psi}\right) P_{O_2}(\delta, T_0)^{\frac{1}{2}} \qquad \textbf{2.4.2-20}$$

where the reference pressure P_{ref} is 1 atm. Combining **Equations 2.4.2-19** and **2.4.2-20** and eliminating ψ gives an expression for $d\delta_{ox}/dt$ that depends only on determining $P_{O_2}(\delta, T_0)$

$$\frac{d\delta_{ox}}{dt} = \frac{F_{ox}}{n_{CeO_2}} \left(\frac{2P_{O_2}(\delta,T_0)}{\left(P_{tot} - P_{O_2}(\delta,T_0)\right)} - \frac{\chi_{H_2O}K_{H_2O,T_0}}{\left(P_{O_2}(\delta,T_0)^{\frac{1}{2}} + K_{H_2O,T_0}\right)} \right) \qquad \textbf{2.4.2-21}$$

In analogy to **Equation 2.4.2-9**, the time evolution of the gravimetric hydrogen production can be determined from the above result for the evolution of the nonstoichiometry using the relationship

$$\dot{V}_{H_2}(t) = -\frac{V_M}{M_{CeO_2}} \frac{d\delta_{ox}}{dt} \qquad \textbf{2.4.2-22}$$

2.4.3 Demonstration with Ceria Fiberboard Structure

2.4.3.1 Characterization

A potential commercial supplier of porous ceria (Zircar Zirconia Inc.) was identified, and an evaluation of the material was performed. The material supplied is in the form of porous fiberboard, robust enough to support twice its weight, but readily machined to arbitrary dimensions. Evaluation initially focused on thermal stability. The material was characterized by X-ray powder diffraction, scanning electron microscopy, and porosimetry. Measurements were performed on the as-received fiberboard and on samples heated to 1500°C at a rate of 15°C/min and held there for 6 h (followed by cooling at 20°C/min). No visual deformation of the sample was evident following the heat treatment. The measurement results are presented in **Figure 2.4-3** through **Figure 2.4-5**.

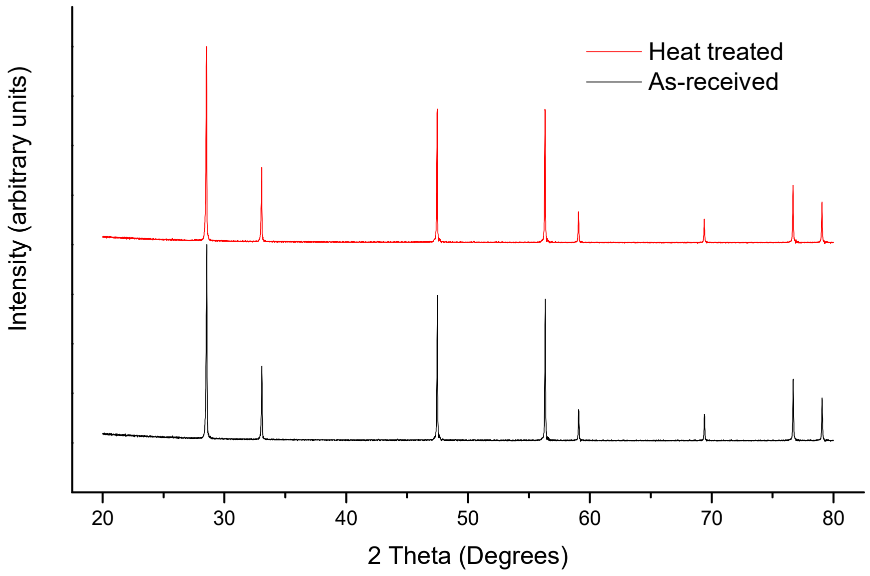

FIGURE 2.4-3 Comparison of the XRD pattern from the as-received ceria fiberboard and heat-treated ceria

The x-ray diffraction results, **Figure 2.4-3**, show appropriate peak positions, both before and after heat treatment. Again, the heat treatment has not induced any changes.

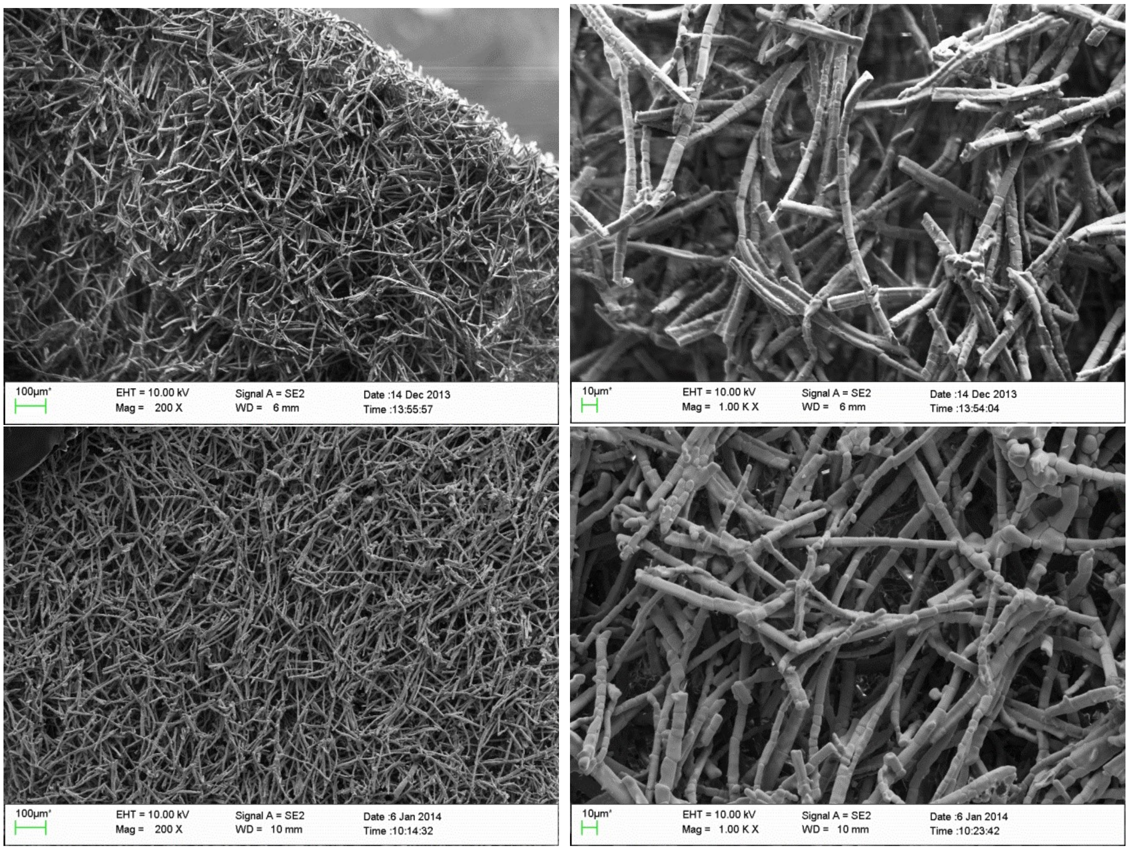

FIGURE 2.4-4 SEM images of the ceria fiberboard at low (left) and high (right) magnification. Upper images are from as-received samples, whereas lower images are after heat-treatment.

As evident from the SEM images in **Figure 2.4-4**, the ceria fiberboard is composed of fibers each between 300 and 500 μm in length and 4-5 μm in diameter. Each fiber is, in turn, composed of cylindrical grains with lengths ranging from 5 to 20 μm. The random orientation of fibers is the apparent reason for the ease of machining; no particular direction is favored for fracture. The microstructure is unchanged after heat treatment, indicating suitability of the overall architecture for thermochemical cycling.

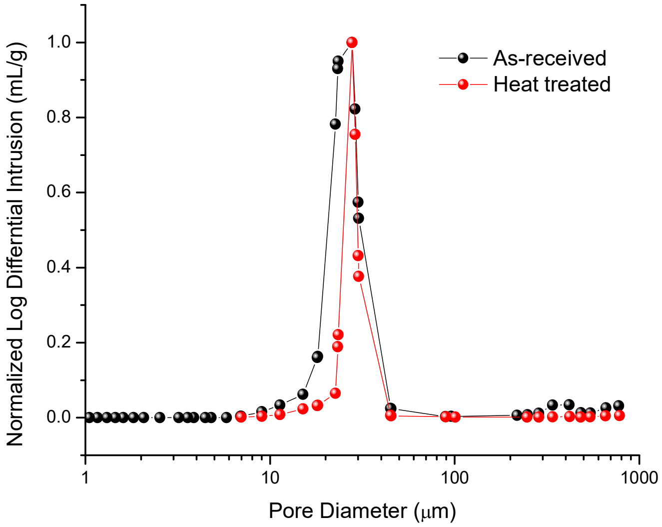

FIGURE 2.4-5 Normalized log differential intrusion versus pore size diameter for the as-received and heat-treated ceria fiberboard

The results of the porosimetry measurements, **Figure 2.4-5**, similarly indicate that the material microstructure is virtually unchanged upon heat treatment. The dependence of the normalized log differential intrusion volume on pore size provides a measure of the pore distribution in the sample. In this case, the pores are distributed between 30 and 20 μm with extremely low variance. The as-received ceria fiberboard has an average pore size of 25 μm and bulk porosity of 85.4%. The heat-treated samples displayed an average pore size of 26 μm and bulk porosity of 88.0%. Additionally, the average measured apparent skeletal density of the two samples is 6.9 g/cm^3. When compared to the actual density of ceria (7.2 g/cm^3), this value indicates that over 95% of the pores are accessible.

The combination of structural stability and pore accessibility renders the ceria fiberboard very promising for thermochemical cycling. This material is further available in ‘grog’ form, in which the fiberboard is subjected to milling to create pieces 1.2 to 2.4 mm in diameter, ideally suited for reactor operation.

2.4.3.2 Thermochemical Cycling

In order to evaluate the volatility and stability of the fiberboard material, extended high-temperature thermochemical cycling experiments were performed. The evaluated grog material is composed of irregular pellets 2.38 – 1.19 mm in diameter, prepared by Zircar by crushing fiberboard with a density of 125 lb/ft^3. A sample (3 g) was heated to 1500°C in an electric furnace, and the atmosphere was switched between 400 mL/min of reducing gas (10 ppm O_2 in Ar) and 400 mL/min of oxidizing gas (20% H_2O in Ar), with the material held under each atmosphere for 30 minutes, such that a full cycle was one hour in duration. During the evaluation, the material was exposed to more than 100 such cycles. In total, the material was held at 1500°C for ~ 4.5 days.

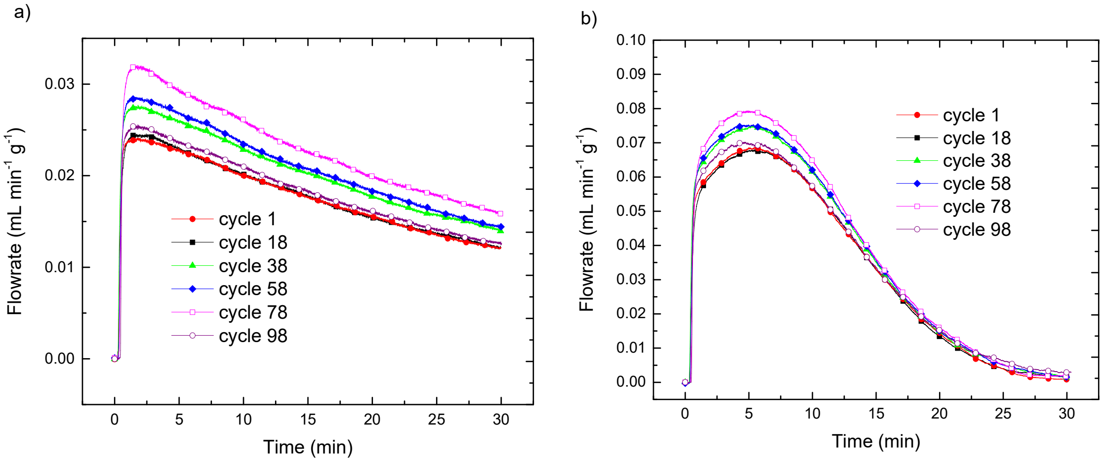

Figure 2.4-6 Isothermal cycling behavior of 3 g ceria fiberboard grog at 1500°C under 400 mL/min reducing gas (10 ppm O_2 in Ar) for 30 min and 400 mL/min of oxidizing gas (20% H_2O in Ar) for 30 min. (a) shows oxygen release profiles for six selected cycles of the 100-cycle test and (b) shows hydrogen production profiles for the same six selected cycles of the 100-cycle test.

The production curves of selected cycles from the 100-cycle evaluation are given in **Figure 2.4-6**. The shapes of the oxygen and hydrogen production profiles are generally reproduced for all of the cycles, although there is some variation in the magnitudes of the oxygen and hydrogen production curves, with the middle cycles (particularly cycles 58 and 78) peaking higher than the early or late cycles. The integrated gas productions for representative cycles are given in **Table 2.4.3-1**. From the table, it is clear that the total gas production is periodically increasing during the evaluation. We hypothesize that this effect is caused by the periodic water addition to the bubbler system and draining of the condenser required over such a long measurement time.

TABLE 2.4.3-1 Integrated Oxygen and Hydrogen Production (mL/g) for Selected Cycles During 100-Cycle Test

Cycle	1	10	18	28	38	48	58	68	78	88	98
O_2	0.53	0.53	0.53	0.82	0.61	0.58	0.62	0.56	0.68	0.60	0.55
H_2	0.99	1.00	0.99	1.27	1.08	1.06	1.10	1.04	1.13	1.09	1.03

At the conclusion of the experiment, the ceria fiberboard was recovered; 2.9 g of material was recovered, representing 96% of the material originally added to the furnace. Because of the relatively stable fuel production, the 4% mass loss is tentatively attributed to handling losses, rather than volatility of the ceria. Furthermore, the reactor displayed no visual evidence of ceria volatilization.

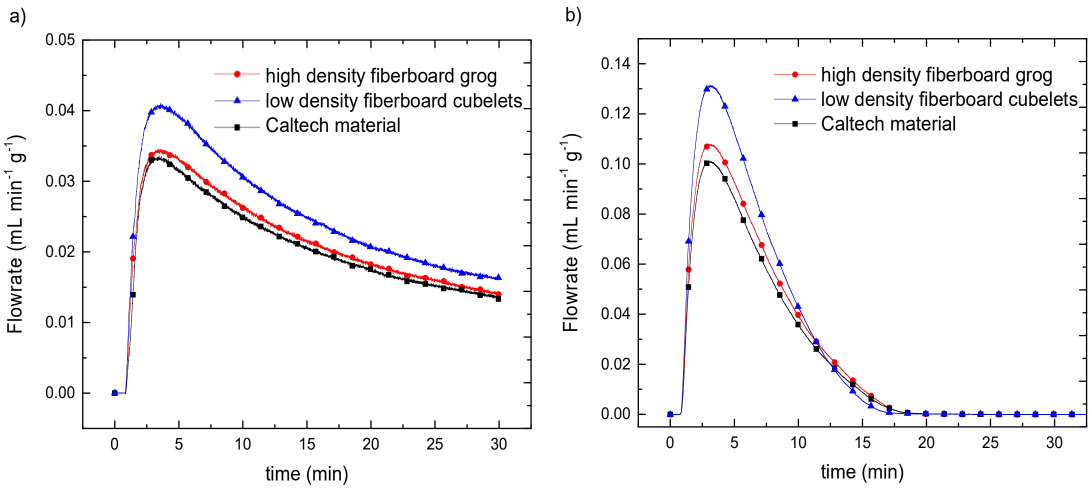

Figure 2.4-7 The reduction (a) and oxidation (b) profiles for the second cycle of zircar and Caltech ceria materials

Properties of the low- and high-density materials from Zircar were compared to the in-house prepared porous ceria via isothermal pressure-swing cycling. Specific materials are high-density fiberboard grog (125 lb/ft^3, 75% porosity), low-density fiberboard cubelets (60 lb/ft^3, 87% porosity, ~2 mm on edge), and Caltech materials prepared using a fugitive pore-former (90 lb/ft^3, 80% porosity). Thermochemical cycling was performed on each material with experimental conditions as follows: 0.5 grams of the sample were reduced for 30 minutes in 10 ppm O_2 in Ar at 100 ml/min, and then oxidized for 45 minutes in 20% steam in Ar at 100 mL/min. In each case, 10 or 11 cycles were performed, exposing the samples to 1500°C for approximately 24 hours total. **Figure 2.4-7** compares the oxidation and reduction of each material for a characteristic cycle. The low-density ceria fiberboard cubes display significantly more rapid kinetics for both oxygen evolution and hydrogen production. Surprisingly, the Caltech material, which has an intermediate porosity (80%) does not display intermediate kinetics. Instead, it behaves very much like the grog (74% porosity). Thus, porosity alone is not a sufficient parameter for predicting kinetic characteristics. In this case, factors such as internal surface-to-volume ratio and tortuosity may play a role. Most significantly, the low-density fiberboard produces 20% more hydrogen per unit mass than both Caltech's pellets and the high density fiberboard grog under the same experimental conditions. This difference is substantial. However, there are challenges in taking advantage of this enhanced kinetic response in actual reactor systems because of the difficulties in packing sufficient material mass into the given reactor volume. Whether or not the 20% increase in gravimetric fuel production outweighs the 18% decrease in material mass per volume remains to be resolved.

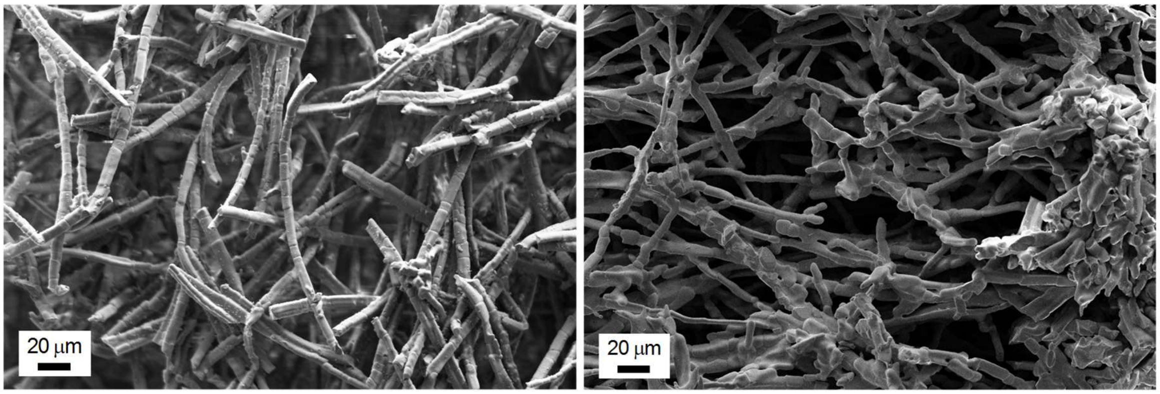

FIGURE 2.4-8 Low-density fiberboard before (left) and after (right) thermochemical cycling; exposed to 1500°C for more than 24 hr.

Scanning electron microscopy images of the low-density Zircar materials, before and after thermochemical cycling are presented in **Figure 2.4-8**. The sample retains its fibrous morphology over the course of the 24-hour treatment. In some regions (not shown), the low-density fiberboard exhibited slight particle agglomeration. However, fuel production profiles for the second and final cycles (not shown) were indistinguishable, indicating that any agglomeration over this short time scale is truly minimal. X-ray diffraction analysis (not shown) similarly revealed no change in the material after longtime exposure to 1500°C.

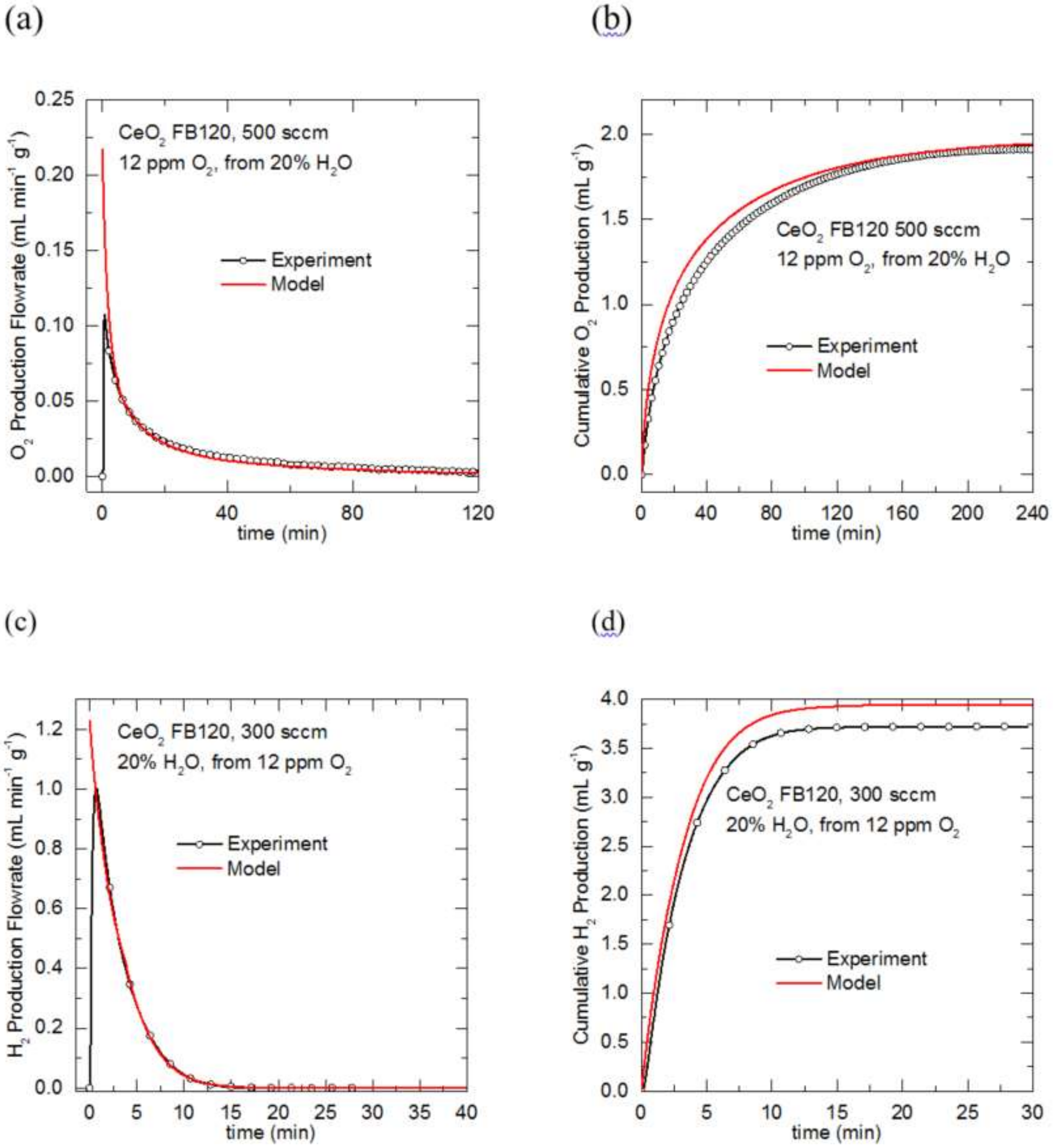

FIGURE 2.4-9 Oxygen release profile of ceria fiberboard, FB120, exposed to 1.2 × 10^{-5} atm pO_2 (balance Ar) at 1500°C, subsequent to oxidation by 20% H_2O in Ar at 1500°C

In **Figure 2.4-9**, a comparison is provided between the computed thermokinetic model and measured gas production profiles of neat ceria. In **Figure 2.4-9, a** and **b** refer respectively to the instantaneous and cumulative oxygen release behavior; **Figure 2.4-9 c** and **d** refer, respectively, to the analogous results for hydrogen production. The time-dependent models for the change in nonstoichiometry are compared to those of measured isothermal cycling data obtained from the fiberboard. This material is the Zircar ‘grog,’ and is prepared by crushing ceria fiber board of 120 lb/ft^3 density and selecting out, via sieving, particles that fall between Tyler mesh sizes of -8 and +14. The characteristic particle length was determined to be 1-3 mm by image analysis. Here 0.512 g of material was used for cycling experiments. Measurements were performed at 1500°C. Reduction was carried out for 4 hr under 10 ppm O_2 in Ar using a gas flow rate of 500 sccm. Subsequent oxidation was performed for 30 min under 20% steam in Ar, supplied at a flow rate of 300 sccm.

For both reduction (**Figure 2.4-9ab**) and oxidation (**Figure 2.4-9cd**), the experimental data are in remarkable agreement with the computed profiles. This agreement indicates that, in the flow regime of interest and for typical porous microstructures, the rate at which the material changes oxidation state is dictated by the thermodynamic, rather than kinetic, properties of the material. The deviation at $t = 0$ in the case of reduction is attributed to the finite time required to fully change out gas atmospheres in the furnace. In the case of oxidation, the deviation is attributed to consumption of the initial hydrogen produced by residual oxygen.

Understanding the relative roles of thermodynamic and kinetic properties has profound implications on how to define strategies to enhance fuel production rates and overall efficiency. Essentially, the kinetics are so fast at these low flow rates that enhancing surface reaction rate or bulk diffusion, or even modifying pore structure to increase surface area or decrease diffusion length, will have no effect whatsoever on the material response. Indeed, even the asymmetry between the rates of oxidation and reduction are unrelated to surface reaction kinetics, but can be explained instead by thermodynamic properties. The situation stands in stark contrast to temperature-swing thermochemical fuel production, in which the fuel production half-cycle on porous ceria is unquestionably rate-limited by surface reaction kinetics, even at moderate flow rates.

2.4.3.3 Limits of application for the Thermokinetic Limit

The two different cycling strategies discussed earlier in their chapter yield 4 distinct cycling paradigms. Oxidation at high temperature, oxidation at low temperature, reduction at high temperature, and reduction during a ramp from low to high temperature. Each of these are demonstrated in Figure **Figure 2.4-10**. It is clear to see that the low temperature oxidation behavior is the only case in which the thermokinetic model predicts significantly faster gas production rates than are actually observed experimentally.

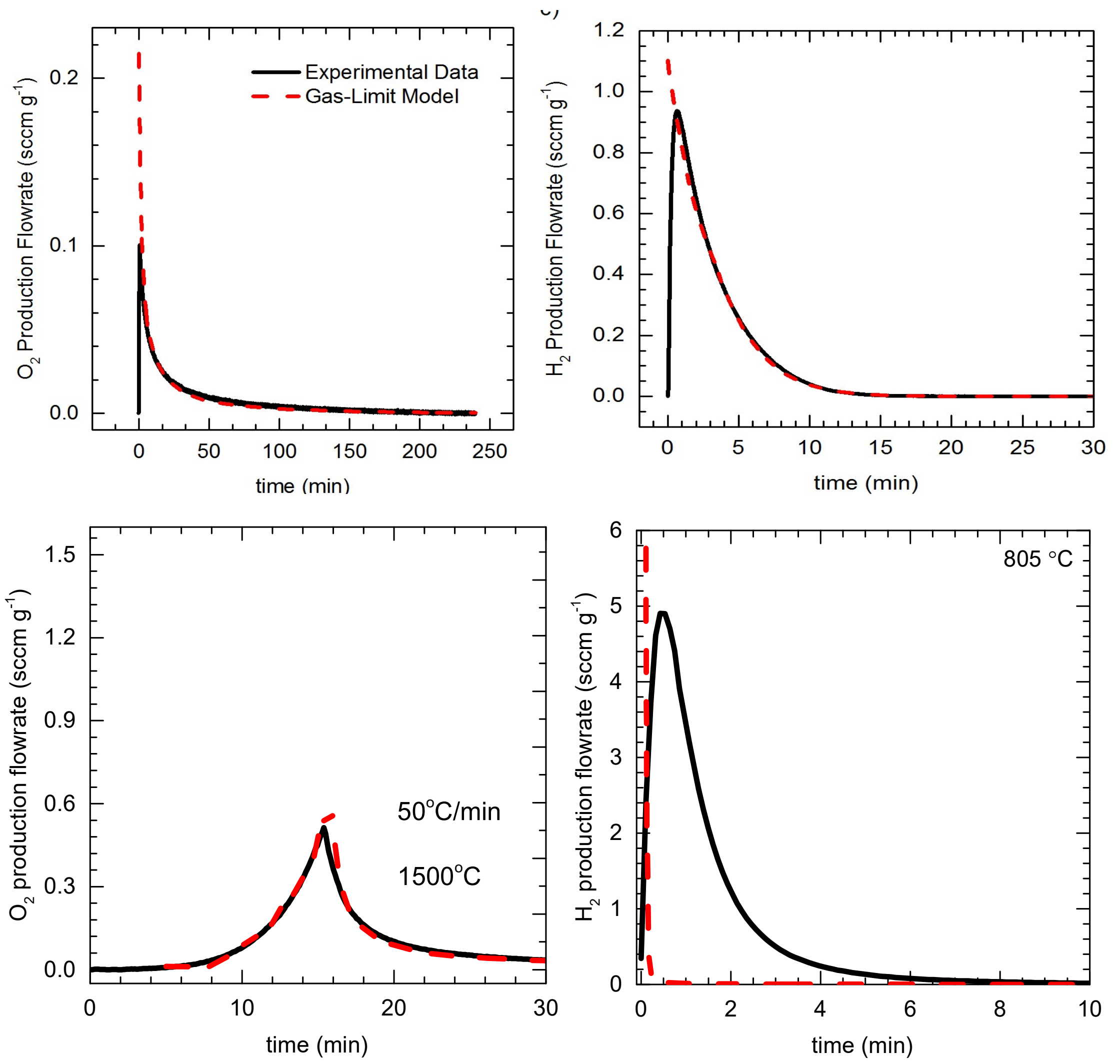

FIGURE 2.4-10 Oxidation and reduction of ceria under high temperature reduction at 1500 ºC (upper left), high temperature oxidation at 1500 ºC (upper right), ramped reduction from 800 ºC to 1500 ºC at 50 ºC/min (lower left) and low temperature oxidation at 805 ºC (lower right).

Thus for practical thermochemical cycling applications the surface kinetics and bulk ionic diffusion coefficients only limit the cycling behavior of ceria under low temperature oxidation. In the following section most of the cycling work will be focused on exploring low temperature oxidation behavior. Some isothermal pressure-sqing cycling will be relevant in order to demonstrate how under certain finite cycling times and conditions, other materials can outperform ceria.

2.5 Goals of the Present Work

This work aims to understand the mechanisms by which a more efficient thermochemical reactor could be realized. The approach taken is two-fold. First to explore novel materials that will improve upon ceria's solar fuel production capacity and create a framework for rational material selection. Second to design and analyze a model for reactor design.

1) Analyze structural changes that the ceria and zirconia doped ceria undergo when subject to thermochemical cycling conditions
2) Enhance the cycling performance of zirconia doped ceria by tuning the morphology.
3) Perform thermodynamic evaluation on novel doped ceria compounds and demonstrate in situ thermochemical cycling
4) Investigate various lanthanum strontium manganite oxide compositions for both two temperature and isothermal pressure-swing cycling
5) Extend the thermokinetic model for fuel production to allow for more accurate application to large scale reactor systems

Chapter 3 Thermomechanical Strain in ZDC

3.1 Introduction

In this section, the practical barriers to realizing a more efficient means of solar fuel production are explored in particular, reactive oxide morphology. Manipulation of macroscopic architecture can improve the performance of catalyst materials relevant to thermochemical cycling applications. In addition to improving the reactive element's kinetic performance, understanding the physical behavior of ceramics at high temperature will enable reactor designs that allow for more efficient solar-to-fuel energy conversion. One major obstacle to more efficient fuel production in thermochemical reactors is the batch-wise heating and cooling process. Namely, no fuel is produced during the heating stages, and no sunlight is used while the reactor is cooling for the low-temperature oxidation step.

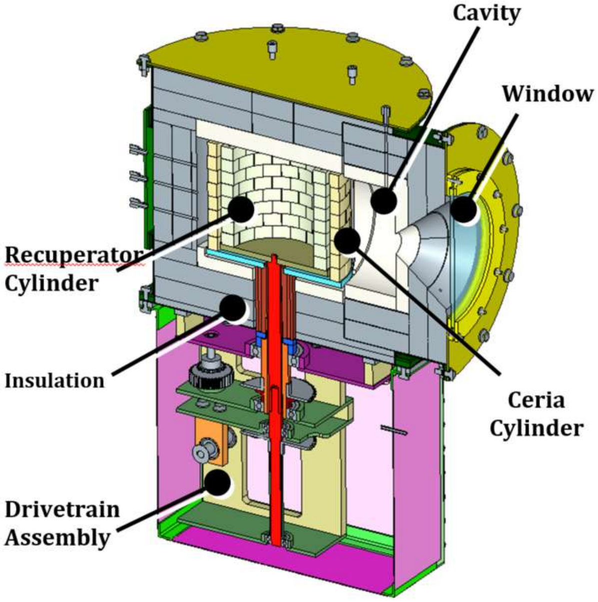

FIGURE 3.1-1 Schematic of the novel thermochemical reactor design (courtesy UM)

Here a reactor operation schematic is discussed that allows for continuous solar energy utilization and continuous fuel production. These improvements should allow for greater than 1% solar-to-fuel efficiency, which is the current state-of-the-art in solar concentrator reactors [11]. The low efficiency is primarily due to poor solid-state heat recovery during the cooling phase of the reactor. The reactor schematic in **Figure 3.1-1** introduces a unique but simple solid-state heat recuperation system. In this design, concentrated solar radiation heats one side of the central ceria annulus exposed to the reduction gas. On the opposite side, the annulus, at a lower temperature, is exposed to the oxidizing gas. The annulus rotates through the two zones such that half is continuously reducing and half continuously oxidizing. The key to heat recovery is an alumina annulus inside the ceria annulus, which rotates in the opposite direction. This way, the part of the alumina annulus in the hot zone will rotate out of the zone next to the ceria that is about to enter the hot zone. The radiative heat from the alumina annulus will serve to preheat the ceria. A similar cooling effect occurs on the opposite half of the reactor. Theoretical calculations done by Prof. Jane Davidson at the University of Minnesota (UM) indicate that this reactor design could reach 10% solar-to-fuel conversion efficiency.

Quintessential to the demonstration of a 10% efficient, 3 kW scale solar-thermochemical reactor is the successful design of macroscopic monoliths of porous ceria with high porosity, good mechanical integrity, and arbitrary dimensions. Success in this aspect is particularly important since the advanced reactor design requires the reactive oxide to be mechanically self-supporting. Since half of the annulus is exposed to two different regimes, the spatial non-uniformity of the radiative solar heating will subject the ceria annulus to significant thermal and chemical gradients. Formation of oxygen vacancies yields electrostatic forces, which, in combination with thermal energy and the larger radius of the Ce^{3+} cation, will cause the reactor core to undergo thermochemical expansion, where the ceria lattice constant increases. The thermal and chemical gradients will impose non-uniform lengthening of atomic bonds, introducing significant strain to the material. Additionally, the fabrication of porous monolithic structures from ceria should have porosity tuned to maximize surface area for reactivity, maximize gas transport rates, minimize structural coarsening during operation, and maximize temperature uniformity. To date, efforts carried out to prepare such monoliths (primarily by employing fugitive pore-formers) have been largely unsuccessful. Furthermore, even if the challenges are ultimately overcome, there is little flexibility in terms of macroscopic dimensions because these methods rely on the use of a die in which to form the final shape. Preliminary modeling by Professor Davidson's group indicates that these structures will fail when exposed to conditions in the reactor.

To better understand these challenges, the thermochemical expansion behavior of ceria and ceria-based derivatives have been evaluated to determine how much the annulus of the reactor will expand and contract during cycling. In addition, alternate microstructures for the annulus were investigated, namely, reticulated porous ceramics, which have markedly improved thermal conductivity. High effective thermal conductivity will promote temperature uniformity, which alleviates strain in the lattice. Inverse opals were also investigated as a potential high-surface-area and rapid-kinetics microstructure for the reactor. Lastly, a ceramic fiberboard structure was evaluated via mercury porosimetry and thermochemical cycling.

3.2 Thermochemical Expansion of Doped and Undoped Ceria

3.2.1 Background

Nonstoichiometric oxides play a critical role not only in thermochemical cycling, but also in other high temperature applications and energy technologies [18-21]. The vacancies that form at high temperatures and under reducing conditions allow for exceptionally fast rates of oxygen ion diffusion throughout the bulk of the materials. The vacancy formation process also causes a volumetric expansion of the lattice. These changes in cell volume will cause mechanical stresses, which may cause failure of the devices [22-24]. It is crucial to understand this behavior for the design of future applications.

The expansion of the cell is especially critical to two-temperature thermochemical cycling reactors where several temperature and nonstoichiometry gradients will occur. The thermal expansion is due to the longer bond lengths from more energetic atomic vibrations. The chemical expansion itself results from two different processes. The predominant cause is the 23% (97 pm to 119 pm) increase in ionic radius as ceria is reduced from the 4+ to the 3+ oxidation state. The second process is the formation of the oxygen vacancy itself. The removal of the oxygen ion exposes the positively charged metal ions to one another, causing electrostatic repulsion. Each of these phenomena is of particular concern for two-temperature thermochemical reactors where the reactive element is subjected to a wide range of temperatures and oxygen partial pressures. The lower temperature behavior for ceria constitutes much of the literature's focus [24], but here the higher temperature behavior will be explored.

In addition to ceria, zirconium doped ceria has been of particular interest to the thermochemical cycling community [25]. Zirconium will always exist in the 4+ oxidation state. Unlike most lanthanides, it is not redox active, and consequently will not participate in the reduction or oxidation reaction. Since it is smaller in radius than cerium 4+, introducing it into the lattice will cause strain, which can be relieved when the cerium reduces from a smaller 4+ ion to the larger 3+ ion. For this reason, it is expected that doping ceria with zirconia will increase ceria's nonstoichiometry at a given temperature and partial pressure. Zirconia doped ceria (ZDC) is thus expected to have both a greater delta-delta and capacity to produce hydrogen per cycle than neat ceria. Hao et al.'s work confirmed that ZDC has a lower reduction enthalpy and entropy, and will yield more hydrogen per cycle than neat ceria, specifically at reduced temperatures, (T_H = 1300-1500°C, T_L = 500-800°C). Due to ZDC's promise in thermochemical cycling applications, it will be evaluated in addition to ceria. Ceria, $Zr_{0.1}Ce_{0.9}O_2$ (ZDC10), and $Zr_{0.2}Ce_{0.8}O_2$ (ZDC20) were investigated to determine chemical and thermal expansion.

3.2.2 Results

High temperature X-ray diffraction (HT-XRD) scans ranging between 30°C and 1200°C were performed on the three materials under 20% O_2 in Ar and 1% H_2 in Ar. For each scan, Nelson-Riley plots were produced to calculate the lattice parameter and to correct for incorrect sample height and theta measurement. The lattice parameter was then plotted at each temperature to demonstrate the expansion. **Figure 3.2-1** indicates the change in lattice parameter with temperature of ceria, ZDC10, and ZDC20 in air. Note that the error bars are smaller than the data points since XRD patters produce lattice parameters accurate to within one thousandth of an angstrom.

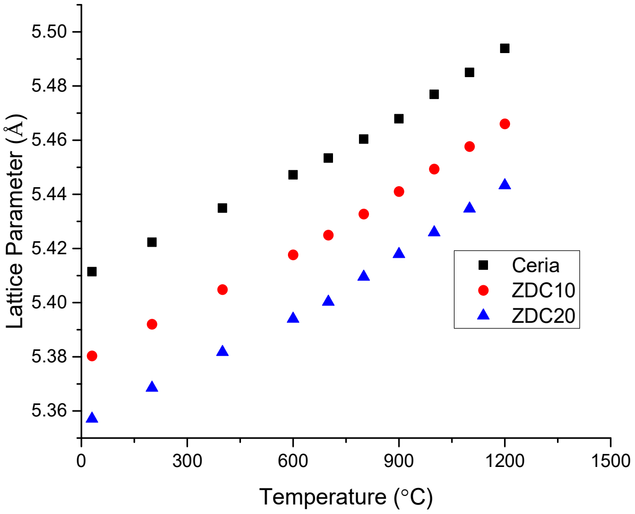

FIGURE 3.2-1 Lattice parameter of Ceria, ZDC10, and ZDC20 as a function of temperature under air.

It is of note that the lattice parameter on this plot is actually a function of both temperature and non-stoichiometry. However, in 20% O_2, the non-stoichiometry of all of the materials is negligible as determined from each material's nonstoichiometry plot. Since there is an absence of chemical and mechanical forces, thermal expansion is the only factor contributing to the uniaxial strain, ϵ, which can be calculated via the equation below. The lattice parameter at a given temperature and oxygen vacancy concentration (defined as δ/2) is denoted by $a(T, x_v)$.

$$\epsilon(T, x_v) = \frac{a(T,x_v) - a(T_{ref},0)}{a(T_{ref},0)} \qquad \textbf{3.2.2-1}$$

The total derivative of the uniaxial strain relates to the thermal and chemical expansion coefficients via the following equation [26].

$$d\epsilon(T, x_v) = \frac{1}{3}\alpha_T dT + \frac{1}{3}\alpha_C dx_v \qquad \textbf{3.2.2-2}$$

Since the concentration of oxygen vacancies is zero for all temperatures under air, taking the derivative of second-degree polynomial best-fit lines to the lattice parameter data allows for direct determination of the thermal expansion coefficient, α_T, as a function of temperature. The thermal expansion coefficients for each material are listed in **Table 3.2.2-1**. It is of note that within the operating temperature range (800°C to 1500°C), there is no significant identifiable trend in the thermal expansion coefficient with increasing dopant concentration of zirconia in ceria.

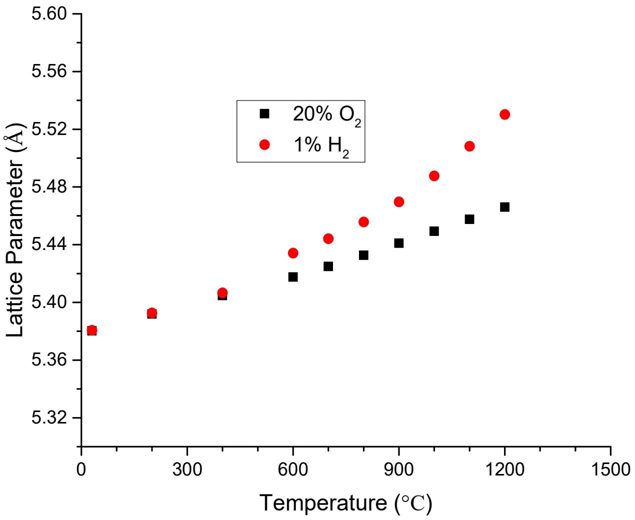

FIGURE 3.2-2 Thermal and Chemical expansion effect on ZDC10 lattice parameter

In order to model the chemical expansion inside the reactor, the same set of high temperature scans were performed for the three materials in an atmosphere of 1% H_2 in Ar, bubbled through water at room temperature. Since the thermodynamics of thermolysis are well known, an equivalent partial pressure of oxygen can be calculated at each temperature. Using the nonstoichiometry data, the oxygen vacancy concentration can be determined at each measurement. **Figure 3.2-2** illustrates the change in lattice parameter for ZDC10 under both gas streams. Note that at temperatures above 600˚C, the effect of chemical expansion is apparent.

To calculate the chemical expansion coefficient, Vegard's law was employed. The law states that, at constant temperatures there will be a linear relationship between the dopant concentration and the lattice parameter. In this case, reduced ceria is equivalent to cerium (IV) oxide doped with cerium (III) oxide. Thus, it is reasonable to assume that the chemical expansion coefficient will have no temperature dependence, and the increase in lattice parameter from chemical expansion can be calculated by subtracting the lattice parameter under air from that of under 1% H2 for each temperature. **Figure 3.2-3** illustrates this result parameterized by nonstoichiometry instead of temperature for all of the materials. As expected, there is a linear relationship between lattice parameter and nonstoichiometry, confirming that there is no temperature dependence on the chemical expansion coefficient. **Table 3.2.2-1** lists the chemical expansion coefficients determined by linear regression analysis.

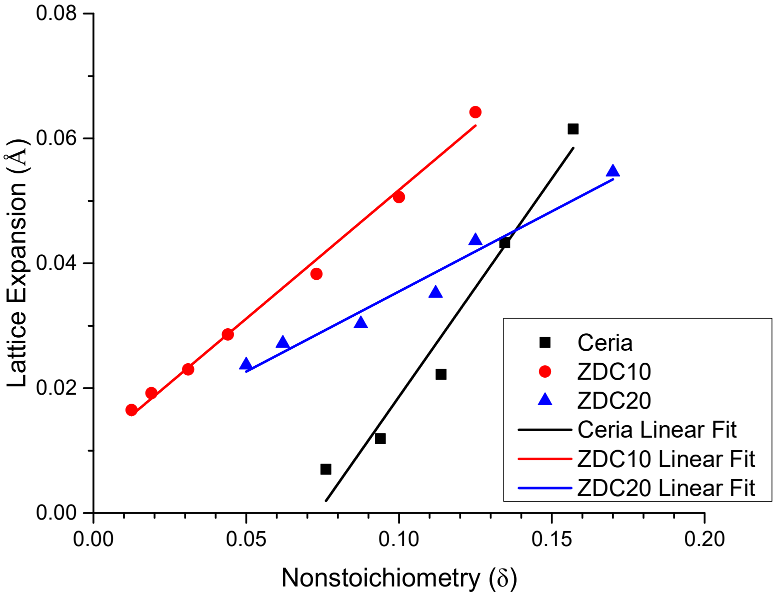

FIGURE 3.2-3 Expansion of lattice parameter as a function of nonstoichiometry for Ceria, ZDC10, and ZDC20

Now that the thermal and chemical expansion behaviors are known, the lattice parameter at each temperature, as well as onstoichiometry, can be determined. Calculating the strain for the projected lattice constant under reducing conditions yields the linear expansion coefficient for a reactive cylinder made from each material. The results are displayed in **Table 3.2.2-1**. Values of thermal and chemical expansion coefficients for ceria match those found in the literature [27, 28].

TABLE 3.2.2-1 Thermochemical Expansion Properties of Ceria, ZDC10, and ZDC20

Material	$1/3\alpha_T$ (ppm/°C)	$1/3\alpha_C$ (1/molO_2)	Linear Expansion Ratio (1500°C, 10ppm O_2)
Ceria	$9.6620 + 5.352\text{x}10^{-3}(T-30°C)$	0.258	0.0213
ZDC 10	$10.741 + 4.736\text{x}10^{-3}(T-30°C)$	0.157	0.0293
ZDC 20	$10.360 + 5.596\text{x}10^{-3}(T-30°C)$	0.095	0.0271

Thus, for a reactive annulus with a height of 20 cm and outer diameter of 13.3 cm, like the one described in the introduction, it will at most expand to 20.6 cm and 13.7 cm respectively. It will be necessary to include this amount of space in the reactor core.

3.2.3 Implications

Beyond calculating the dimensions of the individual reactor components, the thermochemical expansion information can be useful for directing the development of materials that exhibit reduced volumetric expansion under cycling conditions. Marrocchelli et al. performed molecular dynamic simulations to probe the dual effects of vacancy formation and metal ion reduction in the crystal lattice [3]. They found that the introduction of a vacancy resulted in a decrease in the overall lattice parameter. More precisely, the introduction of the vacancy caused the unshielded cations to relax away from one another, while at the same time, nearby oxygen anions were pulled towards the positively charged center. **Figure 3.2-4** demonstrates how the oxygen and cerium ions shift relative to a relaxed lattice. The cerium atoms move by 0.1 Å, while the oxygen ions move by 0.16 Å.

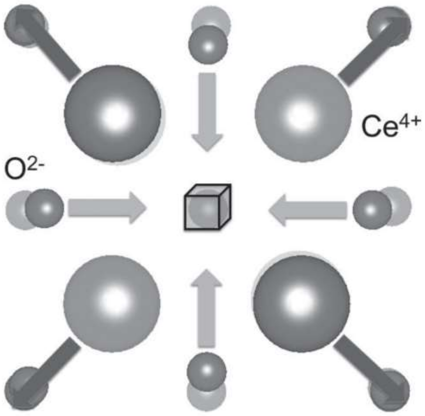

FIGURE 3.2-1 (001) plane local lattice relations observed around a vacancy cube in reduced ceria. Small (big) spheres indicate oxygen (cerium) ions, and lighter shading indicates ions in places below the page (for depth cuing). [3]

Assuming each oxygen vacancy had an effective radius, Hong et al. developed a model centered around Vegard's law that would allow for the determination of this feature [29]. First, simplifying **Equation 3.2.2-1** in order to account for only the chemical expansion in the absence of thermal effect yields the following:

$$\epsilon = \frac{a - a_0}{a_0} = \alpha_C x_v \qquad \textbf{3.2.3-1}$$

For the fluorite structure, the lattice parameter can be related to the ionic radii of the cation and the anion. Each of the cation and anion radii can be expressed as a weighted average of the cations and anions. In the case of the cation, radius is a weighted average of the constituent metal radii. The anion radius is a weighted average of the oxygen ions and vacancies, while taking into account the overall stoichiometry of the compound.

$$a = \frac{4}{\sqrt{3}}(r_{cation} + r_{anion}) \qquad \textbf{3.2.3-2}$$

$$\boldsymbol{r_{cation} = xr_s + (1-x)r_h} \qquad \textbf{3.2.3-3}$$

$$\boldsymbol{r_{anion} = \left(\frac{2-0.5x}{2}\right)r_o + \left(\frac{0.5}{2}x\right)r_v} \qquad \textbf{3.2.3-4}$$

In these equations r_s, r_h, r_o, and r_v refer to the Shannon radii of the substituted cation, the host cation, the oxygen ion, and the oxygen vacancy, respectively. Combining the above equations allows us to determine an expression of the chemical expansion coefficient, which highlights the contribution from the metal ion and the oxygen vacancy.

$$\boldsymbol{\alpha_C = \alpha_M + \alpha_V = \left[\frac{r_s - r_h}{r_h + r_o} + \frac{1}{4}\frac{(r_v - r_o)}{(r_h + r_o)}\right]} \qquad \textbf{3.2.3-5}$$

This equation will permit the determination of the effective oxygen vacancy radius once the chemical expansion coefficient is known. Furthermore, in order to design materials with zero chemical expansion, α_C can be set to zero and the above equation solved for r_s.

$$\boldsymbol{r_s = r_h - \frac{1}{4}(r_v - r_o)} \qquad \textbf{3.2.3-6}$$

Thus, r_s is the ionic radius of an 8-fold coordinated trivalent ion which can be substituted in for an 8-fold coordinated tetravalent ion of ceria. **Table 3.2.3-1** below illustrates the decreasing vacancy radius with increasing zirconium concentration. In order to determine the host ionic radii, Vegard's Law was employed. Note that the decreasing trend in vacancy radius with increasing zirconium concentration coincides with the trend in the chemical expansion coefficient from the previous section.

TABLE 3.2.3-1 Relevant radii in ZDC compounds for modeling thermochemical expansion behavior

Material	r_h (Å)	r_v (Å)	r_o (Å)
Ceria	0.970	1.169	1.397
ZDC10	0.957	1.151	1.397
ZDC20	0.944	1.133	1.397

It is important to note that the substituted cation (those with lower oxidation state) will all be necessarily larger than the host ionic radius, since $r_v - r_o$ is a negative quantity. This suggests that using other fixed valence dopants with smaller ionic radius than zirconium could result in negligible chemical expansion.

Chapter 4 Zirconium doped Ceria inverse Opals

4.1 Background

In order to optimize the reaction kinetics of a reactive monolith, a high surface area and high porosity morphology is desired. Benefits accrue when accessible surface area, rather than total surface area, is increased in materials with ordered porosity. This is a result of decreased reactant gas path tortuosity and increased pore connectivity. As shown in **Figure 4.1-1**, the inverse opal structure is a highly ordered array of pores formed by filling a close-packed array of polystyrene beads with a ceramic solution, and then burning off the polystyrene beads, leaving the negative image. Unlike the reticulated porous ceramic, the pore structure of the inverse opals is ordered, consisting of nodes where the gaps in the polystyrene bead array originated, and struts, which bridge the spacing in those gaps. Inverse opal samples have been synthesized with feature sizes as low as 100 nm. This smaller feature size leads to a higher specific surface area than the RPC morphology, which is desirable for faster reaction kinetics in this surface-reaction-limited process at low temperature. In addition, the ordered design has ideal tortuosity for gas phase access to the surface. These two features make inverse opals ideal morphologies for the oxidation and reduction reactions.

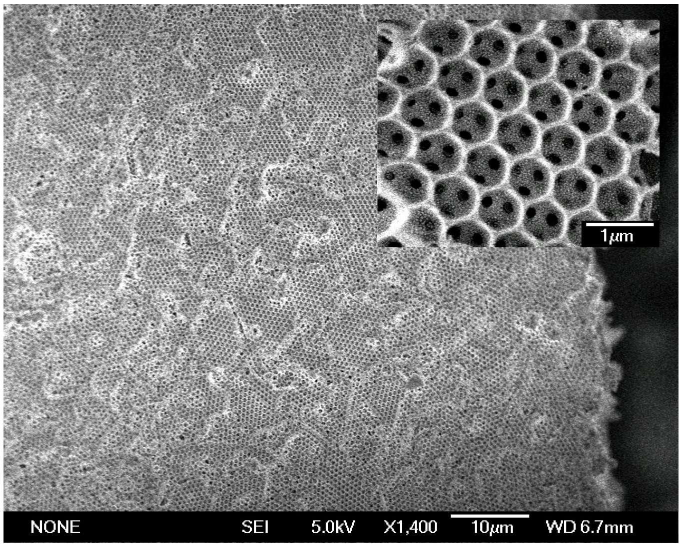

FIGURE 4.1-1 SEM image of the inverse opal ceria-zirconia showing the continuous oxide framework and pore network (inset).

Unfortunately, to date, ceria-based inverse opals have demonstrated poor thermal stability. Namely, the sharp radius of curvature encourages mass diffusion of ceramic from the strut to the node, eventually leading to collapse and densification or coarsening. Previous thermochemical energy production studies with ceria inverse opals focused on cycling at temperatures low enough (550˚C and 800˚C) to maintain ordered structures, but too low for efficient fuel production. In order to harness the benefits attributed to inverse opal architectures, ordered porosity must be preserved at the temperatures required for thermochemical cycling (800-1500˚C). However, ceria undergoes considerable grain growth and coarsening at temperatures greater than 800 ˚C [30]. This results in loss of pore interconnectivity and macroporosity, [31] and after extended time at elevated temperatures, the outcome is complete structural collapse [32-34]. In studies where pure ceria and Zr-substituted ceria inverse opals underwent multiple isothermal redox cycles at 825°C, the authors concluded that increasing Zr content stabilized the macroporous structures [35]. In this work, the thermochemical cycling ability and thermal stability up to temperatures of 1000°C is demonstrated for ceria-zirconia based inverse opals.

4.2 Fabrication and Characterization

Inverse opal samples of ceria and ZDC were prepared and provided by Danielle Casillas in Professor Dunn's laboratory at UCLA. Polystyrene opal templates were prepared by sedimentation of colloidal spheres in solution. The 4.3 μm beads were coated in reduced graphene oxide before sedimentation to improve the connectivity of the inverse structure [36]. The beads were drop-cast onto porcelain crucibles (sub-micron beads), or siliconized silica substrates (4.3 μm beads) and allowed to dry ambiently. The resulting colloidal crystal was finally dried in an oven at 105°C. To create the inverse opal structures, appropriate amounts of ceria-based precursor were added drop-wise (10 μL drop size, multiple rounds of infiltration) to the colloidal crystal templates and allowed to dry overnight at 60°C. The template/sol composite was heated at 1°C/min to 550°C and calcined for 1 hour, followed by annealing at 800°C for one hour (Barnstead Thermolyne, Type FB1400). BET surface areas of the resulting structures fell in the range of ~ 25 to ~ 50 $m^2 g^{-1}$, depending on bead size.

Powder x-ray diffraction (XRD) was performed with a tabletop powder x-ray diffractometer (Rigaku MiniFlex, 300 W) using a Cu Kα source ($\lambda = 1.54$ Å) before and after heat treatment for phase verification. Scherrer's equation was used to estimate crystallite size [37]. Raman spectroscopy (Renishaw, 514 nm) was used to verify subtle changes in the oxygen lattice, such as vacancy formation and emergence of the pseudocubic (t”) phase. SEM was performed using the FEI Nova Nano 230 field emission instrument. Most images were taken in low vacuum mode (10 KV, 60 Pa) – otherwise, samples were sputtered with gold. Inverse opals were lightly crushed and deposited onto sample stubs to ensure that the ordered porosity was viewed throughout the entire sample.

4.3 Gas Phase Diffusion

In order to better understand how varying the inverse opal pore size will affect thermochemical cycling dynamics, gas diffusion and specific surface area are considered. First, inverse opals with larger pore sizes have a lower specific surface area as confirmed by BET measurements listed in **Table 4.3-1**. Thus, larger pore size inverse opals should have a longer characteristic time of oxidation due to the slow surface kinetics of the materials.

TABLE 4.3-1 BET surface area for ZDC20 powders and inverse opals

Inverse opal samples	**Control powders**	**300 nm**	**650 nm**	**1 µm**
Surface area (m^2 g^{-1})	51.8 ± 3.7	36.2 ± 8.8	31.3 ± 1.2	25.1 ± 1.4

One possibility is that the mass diffusion benefit from the larger pores compensates for the lower surface area. To investigate this, one can calculate the type of diffusion dynamics that occur inside the pores. As pore radius decreases, the gas phase diffusion of molecules through them will become slower. Once the pore radius becomes comparable to the mean free path of the gas molecule, Knudsen diffusion occurs [38]. Once the pore radius becomes less than twice the radius of the gas molecule, only single file diffusion can occur, and intuitively, once the pore radius is smaller than the gas molecule radius, the pores will reject the gas molecules. Typical diffusion coefficients for regular molecular diffusion, Knudsen diffusion, and single file diffusion are 10^{-1}, 10^{-5} to 10^{-2}, and 10^{-14} to 10^{-6} cm^2/s, respectively. To determine whether the diffusion in the pores is molecular or Knudsen in nature, it is useful to compare the pore diameter to the mean free path of the gas molecule. This will indicate whether the diffusion is dominated by gas molecule collision with the pore wall, or with other gas molecules. The ratio of mean free path to pore diameter is called the Knudsen number. When the Knudsen number is far above unity, Knudsen diffusion is dominant, and far below unity molecular diffusion is dominant, such that

$$\boldsymbol{Kn = \frac{\lambda}{d} = \frac{k_B T}{\sqrt{2}\pi\sigma_D^2 p d}} \qquad \textbf{4.3-1}$$

where d is the pore diameter, λ is the mean free path, k_B is the Boltzmann constant, T is the temperature, σ_D is the hard sphere diameter of a gas molecule, and p is the pressure. All quantities are in scientific units.

The hard sphere radius (or van der Waals radius) can be determined from the volume exclusion coefficient in the van der Waals equation of state, or the second virial coefficient in the virial equation of state. This quantity is a function of temperature. In some cases, however, the coefficient is negative, indicating that the hard sphere approximation is not valid. For a rough approximation, the hard sphere radius is determined from the molecular volume of the gas using the relation,

$$\mathbf{b} = \boldsymbol{Na} * \frac{4}{3}\boldsymbol{\pi}\left(\frac{\sigma_D}{2}\right)^3 \qquad \mathbf{4.3\text{-}2}$$

where b is the excluded volume coefficient (m^3/mol) and Na is Avogadro's number.

To determine the smallest pore radius that will ensure that molecular diffusion is still dominant, the Knudsen number can be set to 0.1 and then solved for the critical pore radius. The pressure is taken to be atmospheric (101325 Pa). **Table 4.3-2** below outlines the values of van der Waals coefficients used [39], and the resulting critical pore diameters when reaching the transition regime from molecular to Knudsen diffusion for the pertinent species.

TABLE 4.3-2 Critical pore diameters for the transition to Knudsen diffusion

Gas	$b/10^{-5}$ (m^3/mol)	Min. Pore Diameter (µm)	
		800˚C	1500˚C
Water	3.05	1.56	2.58
Oxygen	0.886	3.56	5.88
Hydrogen	0.436	5.71	9.44

The smallest pore diameter in the inverse opal structure occurs in the neck regions, which are about one third the diameter of the beads used to synthesize the structure. Thus, so long as the PS beads used to make the inverse opals are at least 30µm in diameter, the gas phase diffusion in the inverse opal structure should be well within the molecular diffusion regime. Since the inverse opals in this study are significantly smaller in size, it is reasonable to conclude that there are appreciable changes to the diffusion coefficient of the gas molecules over the inverse opal pore diameters investigated.

4.4 Isothermal Chemical Cycling

In order to demonstrate that the inverse opal morphology exhibits the kinetic benefits anticipated in actual thermochemical cycling, low temperature, in-situ chemical cycling experiments were conducted. Since the inverse opal cannot be exposed to temperatures higher than 1000°C, an isothermal chemical cycling method, which mimics the nonstoichiometry of the two-temperature cycling, was employed. Reduction of the sample was achieved by a humidifying hydrogen/argon gas mixture at room temperature. The presence of hydrogen and water vapor fixes an equivalent partial pressure of oxygen at a given temperature (based off of the well-known thermodynamics of water dissociation). In effect, both the oxygen partial pressure and the temperature have been lowered to achieve the same nonstoichiometry after reduction. **Figure 4.4-1** compares the reaction path for the traditional two-temperature thermochemical cycle with the experimental isothermal chemical cycle used here. Note that the vertical displacement in each cycle is approximately the same, indicating that the materials should cycle through the same range of nonstoichiometries and have the same overall fuel production.

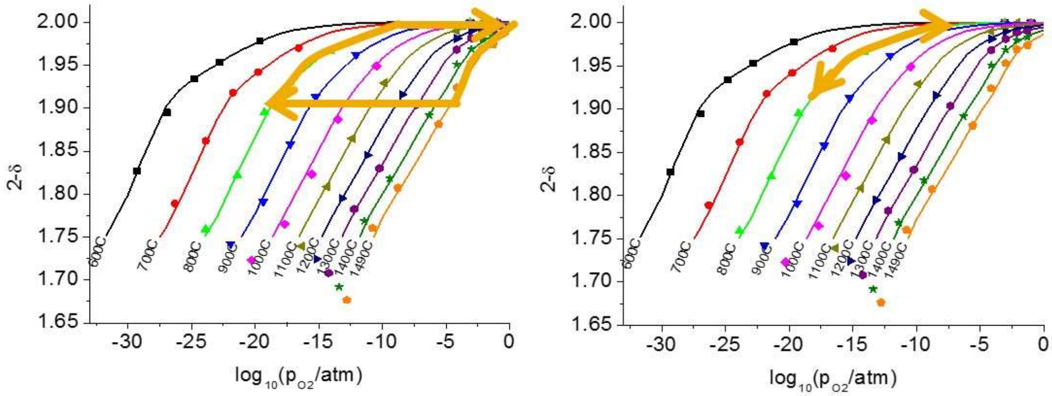

FIGURE 4.4-1 Nonstoichiometry plot of 20% zirconium doped ceria with the traditional thermochemical cycle and the isothermal chemical cycle overlaid on the left and right, respectively.

Chemically-reduced ZDC20 inverse opals having 300 nm, 650 nm, and 1 μm nominal pore sizes were evaluated for hydrogen production efficacy as follows. After synthesis, inverse opals were held at 800°C for 10 hours to equilibrate to experimental conditions. 400 mg samples were placed in a horizontal tube furnace, and heated at rate of 10˚C/min in air to 800˚C. After purging with Ar gas, the samples were reduced by exposure to a mixture of 3% H_2 and 2% H_2O in Ar for 20 minutes, at a flow rate of 200 sccm. This implies a gas velocity of 18 cm/s at the sample and reaction zone flush time of less than 1 second. The reactor was then purged with Ar for 5 minutes (1000 sccm and a gas velocity of 92 cm/s) to remove residual hydrogen, after which the inverse opals were oxidized using a wet Ar stream for 20 minutes (20% H_2O, 200 sccm). The reactor was then purged again with Ar for 5 minutes before beginning another cycle. The process was repeated 12 times. Representative hydrogen production profiles obtained during the inverse opal oxidation step are presented in **Figure 4.4-2.**. The samples were characterized before and after cycling via SEM, and no visual change in microstructure was found. BET measurements indicated only a modest decrease in specific surface area. This is likely due to surface-tension-activated diffusion at high temperatures causing a smoothing of the surfaces.

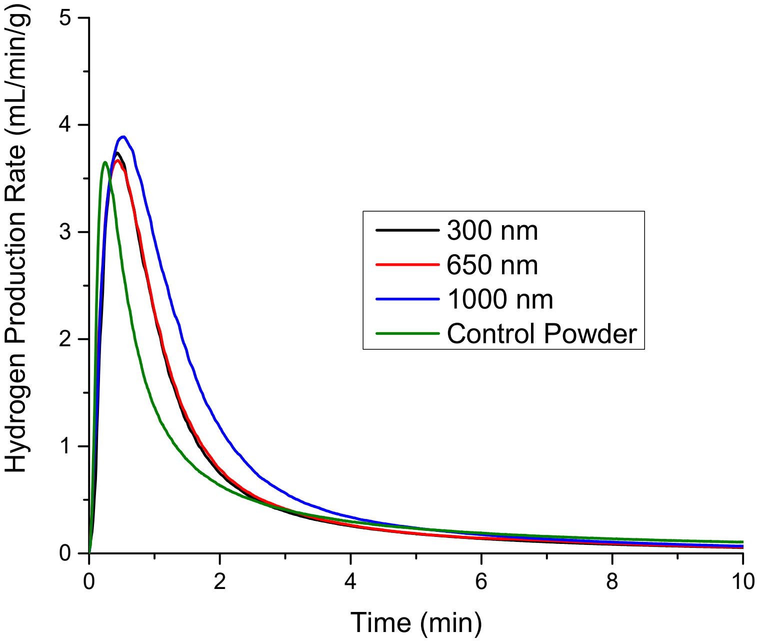

FIGURE 4.4-2 Hydrogen production profiles for different ZDC20 inverse opal microstructures and control powder.

It is immediately clear that there appears to be no significant trend in the hydrogen production of inverse opal samples. This could be due to the tradeoff between available surface area and the ease with which the gas can access the surface of each inverse opal sample (as discussed in the previous section). It is noted, however, that the control material performs similarly to the inverse opal samples. **Figure 4.4-3** shows the modeled hydrogen production profile with the assumption that the reaction is limited by gas flow rate and material thermodynamics. The model shows good agreement with the experimental profiles, replicating both the magnitude of hydrogen produced and the time scale over which it is produced. The disagreement between peak rates in the experimental and modeled profiles are the result of being unable to instantaneously switch gas atmospheres in the experimental set up. In addition, the control powder and 1000 nm inverse opal samples deviate from the model significantly due to varying path lengths for the gases. This alteration in path length is due to the water level in the condenser downstream of the reactor. If gas plugs take longer to reach the mass spectrometer downstream of the reaction, then the hydrogen production profile will broaden, thus taking longer to reach peak production. Conversely, if the time for the gas plugs to reach the mass spec shorten, then the profile will narrow and peak sooner. The minimal influence of pore size is therefore due to material thermodynamics, which serve as the reaction rate-limiting property, as opposed to surface reaction kinetics.

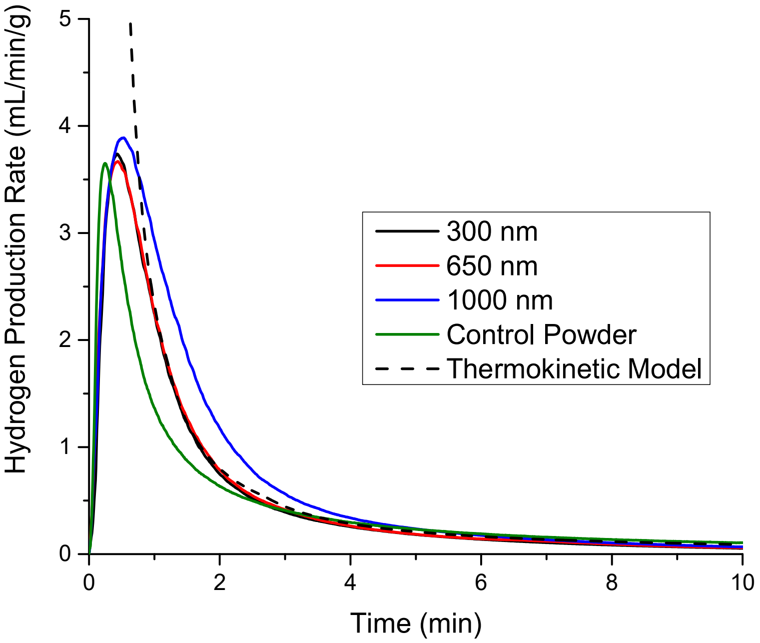

FIGURE 4.4-3 Hydrogen production profiles for different ZDC20 inverse opal microstructures and control powder compared to the thermokinetic model.

4.5 Conclusion

This work aims to allow for successful development of a solar thermochemical reactor with sunlight-to-chemical conversion efficiency significantly greater than the industry best. Novel reactor concepts address system-level shortcomings facing current thermochemical reactors, like batch-wise reactions, poor solid-state heat recovery, and overly complex designs. In order to realize the reactor discussed in the introduction and many others, the ceramic reactive element must be carefully designed. It must be mechanically stable enough to be self-supporting and survive thermal stresses, as well as provide optimal reaction kinetics. To address mechanical robustness, the thermochemical expansion behavior of ceria and zirconia-doped ceria compounds have been characterized, and a synthesis method for ceria RPC structures has been developed as a robust central reactor annulus. Kinetic evaluation of inverse opal and fiberboard structures were performed via in-situ thermochemical cycling. Both of these microstructures were found to exhibit good stability at the temperatures investigated.

These results have implications for both fundamental characterization of materials and for design of reactive components for solar-driven thermochemical cycling. For thermochemical fuel production, typical gas flow rates are low enough to place the material response within the gas-phase limited regimes (higher flow rates result in low solar-to-fuel conversion efficiencies due to the energy penalty of heating large volumes of gas). Consequently, efforts to increase the reactive element’s specific surface area, surface reaction constant, or bulk diffusivity are second to altering the materials’ thermodynamic properties, which will directly affect the gas flow limited regime. A deviation between the relaxation expected on the basis of material thermodynamic properties and the observed relaxation behavior can be used as a diagnostic for evaluating the accessibility of the solid to the sweep gas. Furthermore, although increasing the specific surface area, for example by creating bi-modal porosity, nominally increases the concentration of surface reaction sites, this cannot directly enhance the global response rate. Nevertheless, value remains in designing porous morphologies that optimize gas flow dynamics and, depending on reactor configuration, both solar radiation penetration and thermal transport. Initial studies have indicated that the optimal morphology is one that has hierarchical porosity. Where there is a dense backbone of material to allow for continuous diffusion paths throughout the structure and branches out in dendritic fashion to areas of higher surface area.

Chapter 5 Thermodynamic Evaluation of Advanced Materials

5.1 Doped Ceria Materials

One metric by which materials are evaluated on their capacity to produce hydrogen is the difference between the amount of oxygen vacancies that can be established under reducing conditions and under oxidizing conditions, affectionately termed the “delta-delta” value. In 1975, Panlener et al. investigated ceria’s nonstoichiometry behavior as a function of temperature and oxygen partial pressure. **Figure 5.1-1** displays a digitized version of the data. In this chart, points that lie further up the vertical axis indicate a more oxidized sample. Here, nonstoichiometry values close to zero (top of the plot) represent a fully oxidized material, and as temperature is increased or as the oxygen partial pressure is decreased, the oxide becomes more reduced.

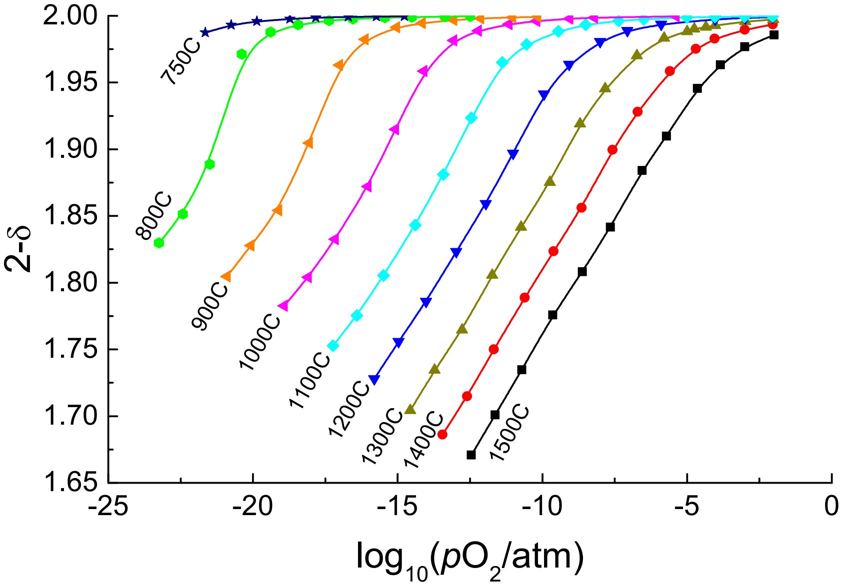

FIGURE 5.1-1 Nonstoichiometry in Ceria [40]

For example, in the most typical thermochemical cycle, ceria is reduced at 1500˚C in 10 ppm O_2 in Ar. This will establish a nonstoichiometry of about 0.067. Subsequent exposure to 20% steam in argon at 800˚C will fully oxidize the sample, since the thermodynamics of thermolysis dictate that the equivalent partial pressure of oxygen for 20% water vapor in inert gas is on the order of 10^{-7} atm. This procedure results in a delta-delta of 0.067, which corresponds to 8.66 mL/H_2, produced per cycle.

To enhance ceria's natural ability to achieve nonstoichiometry, ceria is doped with other lanthanide elements, which, in combination with ceria, remain stable in the cubic fluorite phase. Candidate dopants can be separated into two categories: redox active elements, such as praseodymium and terbium, and elements that are not redox active, such as samarium and zirconium. Redox active elements typically reduce much more easily than ceria, resulting in a larger delta-delta for a given temperature and oxygen partial pressure. Redox inactive dopants do not contribute to the reactions, but can affect the lattice structure by weakening the Ce-O bond, or by providing kinetic benefits. This work focuses on investigations of praseodymium, terbium, and samarium as dopants into the ceria lattice. The materials were all formed into porous pellets using the sol-gel method described in Chapter 2. The nonstoichiometry is measured via thermogravimetric analysis, and the materials are evaluated for their capacity to produce hydrogen. Promising candidate materials were then subjected to thermochemical cycling experiments.

5.1.1 Praseodymium and Terbium Doped Ceria

Praseodymium, which neighbors cerium on the periodic table, is known to be highly soluble in cerium dioxide, and to be somewhat more stable in the 3+ oxidation state than Ce. These factors render it an attractive candidate as a dopant for modifying cerium dioxide, and potentially enhancing the thermodynamic capacity of the latter for fuel production under isothermal operation. Recent reports have already suggested the applicability of Pr-doped ceria (PCO) for two-temperature thermochemical fuel production [41], and even indicate enhanced performance over neat ceria. Accordingly, PCO was selected to be screened as a potential next-generation material – specifically, the composition with the highest activity from the two-temperature study, 10PCO ($Ce_{0.90}Pr_{0.10}O_2$).

10PCO was prepared by the combined EDTA/citric acid solution process to ensure homogeneity. Stoichoimetric quantities of $Ce(NO_3)_3 \cdot 6H_2O$ and $Pr(NO_3)_2 \cdot 6H_2O$ were dissolved in water with 1.5 equivalents of EDTA and citric acid, and the solution pH was adjusted to 10 using ammonium hydroxide. The solvent was evaporated until a gel formed, which was then fired for 5 h at 170°C to form a hardened black foam. The foam was crushed with a mortar and pestle, yielding a black powder that was fired at 350°C for 15 h. In the final step, the resulting off-white powder was calcined at 950°C for 10 h.

In the TGA experiments, 10PCO was heated from room temperature to 1500°C at 10°C/min in 100°C increments (Netszch STA 449). At each step, the temperature was held for 1–3 h. The entire procedure was repeated multiple times, each time using a different gas atmosphere composed of either oxygen and argon or hydrogen and humidified argon. In the latter set of mixtures, the oxygen partial pressure was established through equilibrium between steam, hydrogen, and oxygen, according to the water thermolysis reaction, and its value was directly monitored at the instrument exhaust using a solid-state oxygen sensor. The weight was recorded during each temperature hold. If the sample mass did not reach a constant value during this period, the equilibrium mass was determined by fitting the trace of the mass loss to an exponential decay function.

The nonstoichiometry of 10PCO determined from these measurements is shown in **Figure 5.1-2**, both as a function of temperature for the specific gas atmospheres utilized, and as a function of (equivalent) oxygen partial pressures for the temperatures examined.

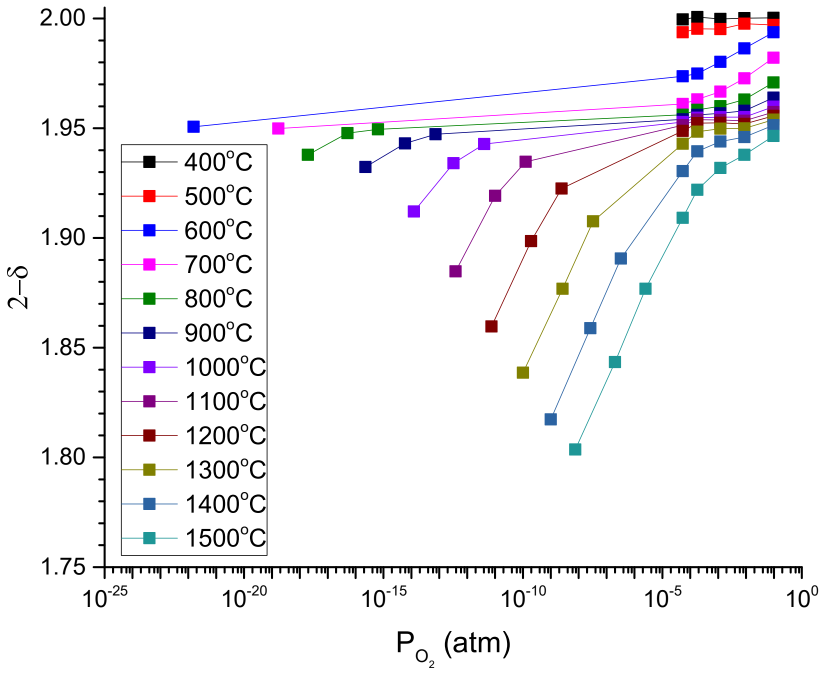

FIGURE 5.1-2 Nonstoichiometry of 10PCO as a function of oxygen partial pressure at various temperatures. The lines are guides to the eye.

Praseodymium is stable in the 4+ oxidation state under air, and is highly soluble in cerium dioxide. For these reasons, praseodymium was an attractive dopant for enhancing thermochemical fuel production. Similarly, terbium is also stable in the 4+ oxidation state under air, and is the only other lanthanide with this property. While broadly quite similar to praseodymium in terms of properties, the more detailed differences in redox behavior and ionic radius may lead to higher potential fuel productivity. Thus, this dopant was selected for investigation after praseodymium and the results of the TGA are presented in **Figure 5.1-3**.

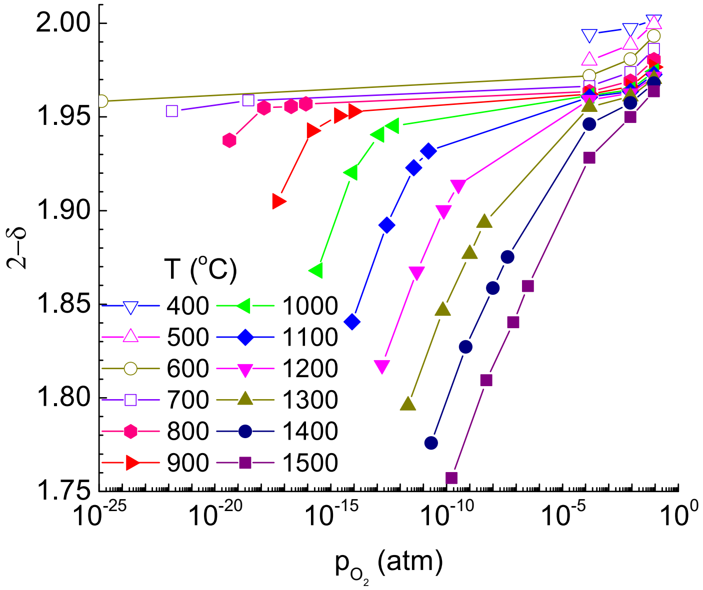

FIGURE 5.1-3 Nonstoichiometry of 10TCO as a function of oxygen partial pressure at various temperatures. The lines are guides to the eye.

The enthalpy and entropy values extracted from an analysis of the TGA data are presented in **Figure 5.1-4**. The figure summarizes the results for neat (undoped) ceria, 10TCO and 10PCO. Both 10TCO and 10PCO display large changes in thermodynamic functions around $\delta = 0.05$, interpreted to be the result of the $Tb^{3+/4+}$ and $Pr^{3+/4+}$ redox couples. At low values of δ, the reduction of Tb and Pr proceeds easily, with enthalpy values that are much smaller than those for Ce reduction. Above $\delta = 0.05$, all of the Tb (or Pr) is in the 3+ oxidation state, and the reduction behavior of 10TCO (or 10PCO) reverts to that of neat ceria. The close match in the thermodynamic functions of 10TCO and 10PCO above δ = 0.05 suggests that the behavior of the $Ce^{3+/4+}$ redox couple is largely unaffected by the presence of the dopant. Below δ = 0.05, the thermodynamic functions for 10TCO and 10PCO differ significantly, and the change in properties is more abrupt for Pr than it is for Tb at the transition (δ = 0.05). Because these materials will be employed at high temperatures under isothermal cycling in which δ is always greater than 0.05 (for both half-cycles), these differences, though striking from a materials-chemistry perspective, are not relevant for reactor operation.

The 10PCO material was subjected to two-temperature thermochemical cycling in hopes that the more easily reduced praseodymium would provide addition fuel production over that of neat ceria. The material was cycled in an IR furnace as described in Chapter 2. It was reduced at 1500°C under 10 ppm O_2 in an argon balance, and

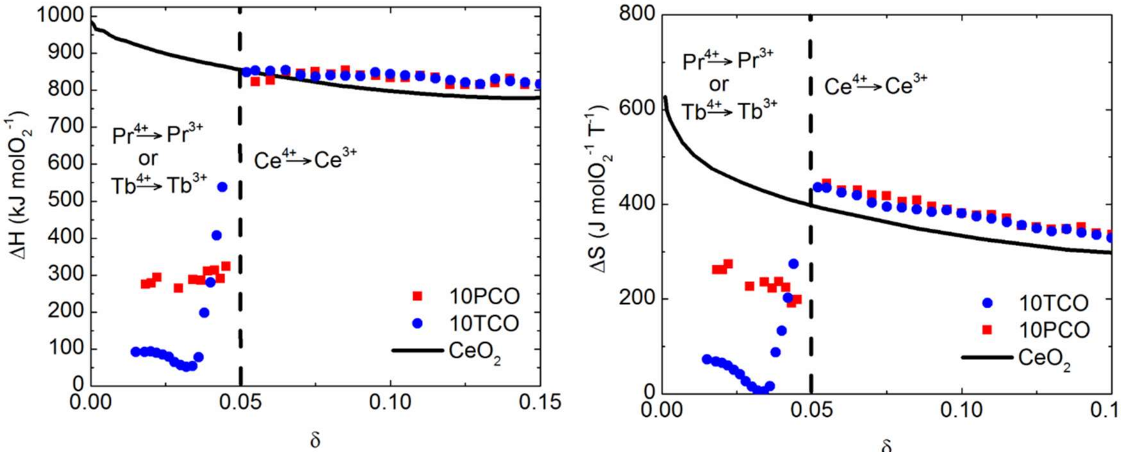

FIGURE 5.1-1 Thermodynamic functions describing the reduction of doped ceria compositions: (a) enthalpy and (b) entropy of reduction as a function of nonstoichiometry. Data for ceria provided for comparison. Accurate determination of the thermodynamic functions at δ close to zero is difficult due to the small weight changes that occur in this region.

oxidized under 20% steam in an argon balance. The material in each cycle was reduced to equilibrium. The oxidation was taken to equilibrium at 800°C, and then temperature was lowered in 200°C increments. The resulting profiles from the experiments are displayed in **Figure 5.1-5**.

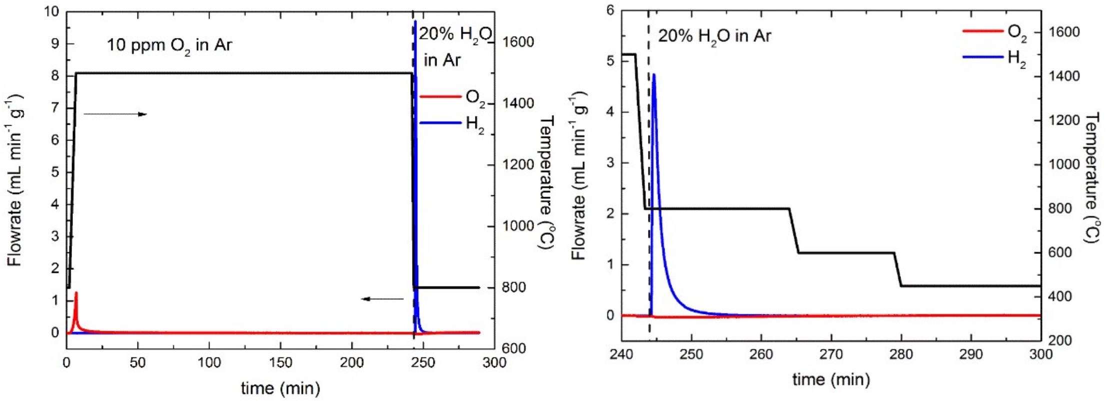

FIGURE 5.1-2 Fuel production from two-temperature cycling of 10PCO for reduction under 10 ppm O2 in Ar, and oxidation in 20% steam (Left). The right image shows fuel production while varying the temperature mid cycle.

In the image on the left in **Figure 5.1-5**, the expected thermodynamic quantities of oxygen and hydrogen are recovered from the cycle operating between 1500°C and 800°C. Under 20% steam at 800°C, only the cerium atoms are reoxidized fully to the 4+ state, and the majority of the praseodymium atoms remain in the 3+ state. Decreasing the temperature further, therefore, should allow for additional hydrogen production. However, even at 425°C, when the material should be fully oxidized, no additional hydrogen production was observed. This result is due to the incredibly low thermodynamic driving force. For rapid hydrogen evolution, as discussed by the thermokinetic limit in subsequent chapters, the nonstoichiometry behavior should be a strong function of oxygen partial pressure. As seen on the isotherms in **Figure 5.1-2**, the nonstoichiometry curves are very weak functions of oxygen partial pressure around $\delta=0.05$. Consequently, the slow rate at which the material reoxidizes prevents it from being a viable candidate for isothermal cycling or two-temperature cycling. Due to the similarity in thermodynamic behavior of 10TCO to 10PCO, it was not investigated for thermochemical cycling.

5.1.2 Samarium Doped Ceria

Samarium doped ceria is a well-established material for solid oxide fuel cells due to its high ionic conductivity [42]. In contrast to praseodymium and terbium, samarium can be expected to retain the 3+ oxidation state under cycling conditions, suggesting it will not enhance the fuel production thermodynamics. Consequently, 15 mol% samarium doped ceria (SDC15, $Sm_{0.15}Ce_{0.85}O_{1.925}$) has a fully oxidized fluorite lattice with inherent oxygen vacancies to maintain charge balance. Furthermore, because Sm is ideally matched in terms of ionic radius to the $CeO_{2-\delta}$ structure, it endows high mobility to the vacancies it generates, suggesting kinetic benefits. These intrinsic oxygen vacancies will facilitate further oxygen ion movement during both the oxidation and reduction cycles. In neat ceria, the reduction step takes approximately four hours to come to completion. The enhanced oxygen ion mobility should decrease the characteristic time of the reduction, and allow cycles to occur more frequently. One drawback of the inherent vacancies, however, is that during the oxidation reaction, those vacancies cannot be filled. This decreases the attainable delta-delta between the two cycles. Thus, a full thermodynamic characterization of the nonstoichiometry behavior is necessary to determine if appreciable amounts of hydrogen can still be obtained during each cycle. Porous pellets of SDC15 were fabricated from commercial SDC15 nanopowder. The powder was poured into a one-inch alumina tube template and sintered for 6 hours at 1500°C. The resulting pellets were approximately 70% porous.

The nonstoichiometry of SDC15 was determined as a function of temperature and oxygen partial pressure with thermogravimetric analysis (TGA). These data were analyzed to obtain the enthalpy and entropy of the reduction reaction. From knowledge of the thermodynamic characteristics, it is immediately possible to compute the maximum production of hydrogen and carbon monoxide attainable from an isothermal cycle, provided a robust screening methodology. In the TGA experiments, SDC15 was heated from room temperature to 1500°C at 10°C/min in 100°C increments (Netszch STA 449). The nonstoichiometry from these measurements is shown in **Figure 5.1-6,** plotted as a function of equivalent partial pressure at a given temperature.

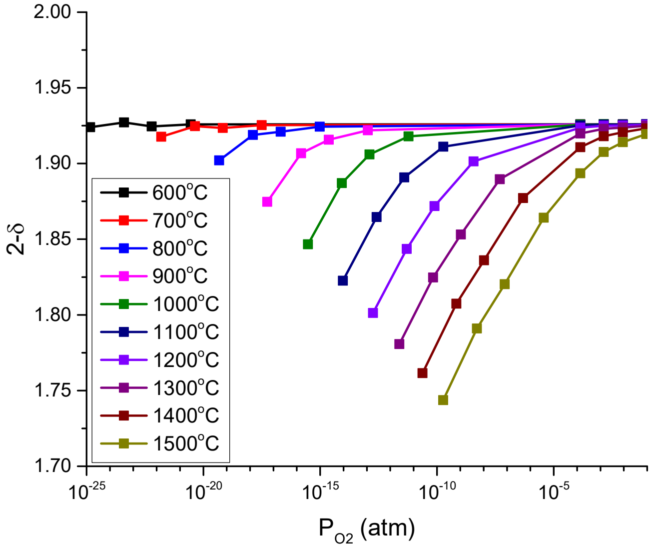

FIGURE 5.1-6 Nonstoichiometry of SDC15 as a function of oxygen partial pressure at various temperatures. The lines are guides to the eye.

As in previous sections, the nonstoichiometry information has been used to determine the enthalpy and entropy of the reduction reaction. The results of this analysis are presented along with a comparison to neat ceria in **Figure 5.1-7**. Both thermodynamic potentials are smooth functions of the nonstoichiometry, indicating that only the cerium is reducing. The entropy is slightly higher than that of neat ceria due to increased configurational entropy from the samarium ions. The slight increase in enthalpy could be due to differences in bond energies between the Ce-O and Sm-O bonds. The enthalpy is relatively independent of nonstoichiometry, indicating ideal solution behavior. Nevertheless, the SDC15 composition displays thermodynamic properties that deviate somewhat from those of ceria, and thus shows that introduction of a redox inactive element is not without consequence.

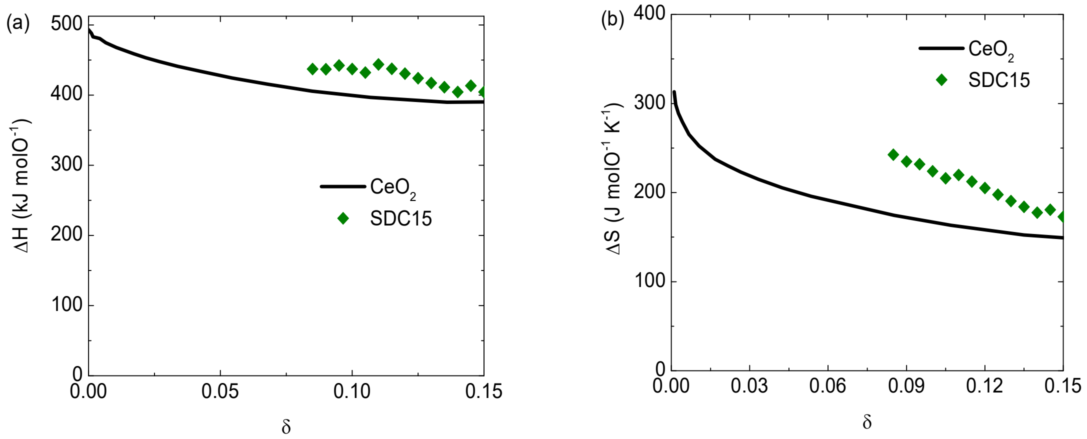

FIGURE 5.1-3 Thermodynamic functions describing the reduction of SDC15: (a) enthalpy and (b) entropy of reduction as a function of nonstoichiometry. Data for ceria provided for comparison.

A quantitative evaluation of the change in δ for a given cycle is possible by computing δ directly from the thermodynamic data for the two cycling conditions. Here, ΔS_{red} and ΔH_{red} are treated, as continuous functions of δ, by interpolation. Considering the case in which the thermochemical cycle is carried out at 1500°C during the reduction under 10 ppm O_2, and at 800°C during the oxidation under 20% H_2O, the oxygen partial pressures for the two conditions are 10^{-5} and 5.6×10^{-7} atm, respectively. For oxidation under 100% CO_2, the equivalent oxygen partial pressure is 1.8×10^{-3} atm. Under these conditions, SDC15 would be cycling between nonstoichiometries of 0.075 and 0.136, resulting in a hydrogen production of 7.88 mL/g per cycle. As expected, this is less than the 8.66 mL/g of H_2 per cycle that undoped ceria is expected to produce.

Because SDC15 has an overall high concentration of oxygen vacancies, it was speculated that the material may have a higher surface reaction constant than the other compositions. It has been established that at moderate temperatures (750 – 850°C), SDC15 has faster surface reaction kinetics than neat ceria under oxidizing conditions, but is comparable to neat ceria under reducing conditions [43]. These findings from small perturbation measurements hold promise that SDC15 will display rapid kinetics at high temperatures, even under large perturbations. To test this hypothesis, porous monoliths of Sm and undoped ceria were prepared using two different methods that yielded comparable porosity. For SDC, the loose powder was lightly packed inside a ½” alumina tube template and then fired, whereas for neat ceria, graphite and starch fugitive pore-formers were utilized, and a robust sintering protocol was followed. In both cases, porosity was ~ 70%. Isothermal cycling was performed at 1500°C, with reduction under 10 ppm O_2 in Ar and oxidation under 20% H_2O in Ar. Half cycle times were 4 hr and 1 hr, respectively. Gas flow rates were fixed at 400 sccm for both half cycles, and sample size for both compositions was 1 g.

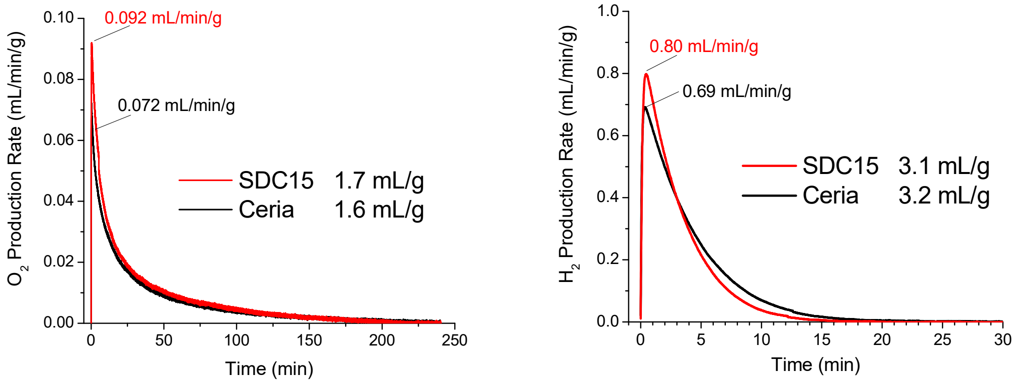

FIGURE 5.1-8 Oxygen release during the reduction reaction (left) and hydrogen release for the oxidation reaction (right) for ceria and SDC15 at 1500°C

The oxygen release and hydrogen production profiles (**Figure 5.1-8**) are generally similar between the two materials. However, the initial peak value in both sets of profiles is higher for SDC15 than it is for ceria. The difference amounts to 25% for oxygen release and 15% for hydrogen production. Similarly, the total (integrated) quantity of oxygen released in the reduction step is slightly higher for SDC15 than for ceria, despite the thermodynamic expectation that neat ceria will release more oxygen. In the case of SDC15, the amount released, 1.7 mL/g, is within error of the expected value of 1.6 mL/g. In contrast, the total oxygen released from neat ceria, 1.6 mL/g, is only ~ 75% of the expected value (2.2 mL/g). This discrepancy suggests that even four hours is insufficient time for the reduction of neat ceria at 1500°C to reach completion. The 1 hr oxidation time, on the other hand, appears to have been sufficient for both compositions to reach full reoxidation. The quantity of hydrogen produced from ceria, 3.2 mL/g, is almost precisely a factor of two greater than the oxygen release. The hydrogen detected from the oxidation of SDC (3.1 mL/g) is smaller than expected on the basis of the oxygen release. However, because of the high initial peak value and rapid decay in signal intensity, this result is taken to be an experimental artifact (possibly due to suboptimal exhaust gas flow configuration) rather than an indication of incomplete reoxidation. A close examination of the hydrogen production profiles shows a measurable kinetic advantage for SDC15 over neat ceria. Given that both reactions represented in **Figure 5.1-8** proceeded to completion, it is possible to directly compare the temporal dependence of the extent of the oxidation reaction. The analysis, **Figure 5.1-9**, reveals that the time to reach 63% completion is 4.3 min for neat ceria, whereas it is 3.3 min for SDC15, which is 23% shorter. In sum, for finite cycling times, SDC15 offers improved absolute fuel production rates, despite a lower theoretical capacity than neat ceria.

As we will see in more detail later in the chapter, the source of SDC's faster hydrogen production kinetics are a result of the concavity of the nonstoichiometry isotherms. Comparing the 1500 ^{o}C isotherms of ceria and SDC15, it is clear that the curl is more negative in the case of SDC15. That is the isotherm is concave down and curves more sharply. This behavior results is more rapid oxidation when governed by the thermokinetic limit.

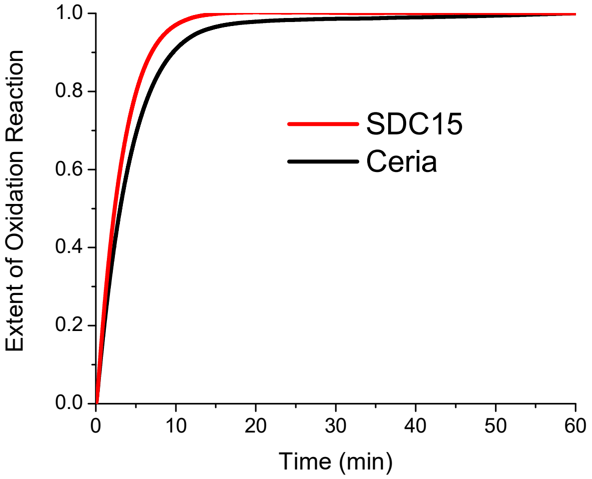

FIGURE 5.1-9 Extent of reaction for ceria and SDC15 oxidized in 20% steam, balance Ar, at 1500°C

5.2 Pressure Swing Cycling of Perovskites

5.2.1 Introduction

Variable valence oxides, in which the cation can adopt several oxidation states, have proven valuable in the process of solar-driven thermochemical fuel production. This far, fluorite structured materials have been examined to find that little practical improvements can be made in the way of thermochemical fuel generation. Now the discussion is turned to perovskite materials, which have a general chemical formula ABO_3. These structures primarily exist in the cubic perovskite structure, depicted in **Figure 5.2-1**, but have several distortions based on the relative ionic radii of the atoms on the A-site and B-Site. At heavily reducing conditions, vacancies form and reorder to form the Brownmillerite phase, a phenomenon observed in cobaltite and ferrite perovskites [44, 45]. At high oxidation states, distortion from Mn^{3+} on the B-site results in the orthorhombic structure was observed via neutron powder diffraction [46, 47]. Under cycling conditions relevant to thermochemical fuel production no phase change is expected. In particular, strontium-doped lanthanum manganite (LSM), which has the perovskite structure, is an attractive material due to the high degree of nonstoichiometry that can be achieved before decomposition. This material also has established nonstoichiometry behavior at lower temperatures (below 1000ºC) due to its relevance in solid oxide fuel cells [48-51].

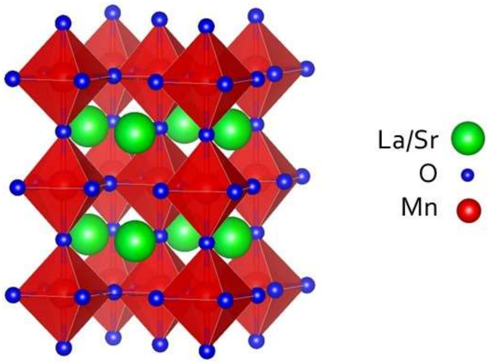

FIGURE 5.2-1 LSM exhibiting the cubic perovskite structure

LSM has already been demonstrated for thermal dissociation of steam and carbon dioxide as well as syngas formation [52-54], but these studies only performed calculation based on oxygen uptake and release rather than fuel production. A material previously considered for temperature-swing cycling. Slow kinetics of hydrogen evolution noted, but in the absence of reliable thermodynamic data and a quantitative model connecting thermodynamic properties to gas evolution rates, it was possible to definitely identify the source of the poor rates. Also, large mass of oxide per hydrogen produced produces large energy penalty for temperature swing cycling. The goal is to understand low hydrogen evolution rates and evaluate LSM's viability for isothermal, pressure-swing cycling Here we will explore the hydrogen production capability of different LSM compositions under both two temperature thermochemical cycling and isothermal pressure swing cycling. The specific compositions are of the form $(La_{1-X}Sr_{X})MnO_3$, with x between 0.1 and 0.5. Previous work by the Yang et al. have found some evidence that the material's kinetic response depends on the ratio of Sr and La cations to Mn cations on the A-site in two temperature ecycling [55]. Specifically, the fuel production increases but the rate of reaction decreases. Another obstacle to two temperature cycling of LSM is its high heat capacity, which is 85% larger than that of neat ceria (208 kJ/mol versus 112 kJ/mol) [56]. The higher heat capacity results in more energy required when transitioning to the high temperature reduction step. In isothermal pressure-swing cycling this is not an obstacle as there is no temperature change.

5.2.2 Two Temperature Thermochemical Cycling

5.2.2.1 Background

The increased reducibility of perovskite materials make them attractive for two temperature cycling equivalent amounts of fuel can be produced at lower temperatures than neat ceria [57]. Many studies in the literature demonstrate only the oxygen release upon reduction but not the fuel productivity upon reoxidation [56]. Yang et al. performed a study on various compositions of lanthanum strontium manganite oxide in which the high temperature reduction and low temperature oxidation was analyzed [55]. They found that at lower temperatures, the introduction of strontium seemed to worsen the reaction kinetics, depicted in **Figure 5.2-2**. Here the low temperature oxidation behavior of LSM is explored in the context of the thermokinetic limit.

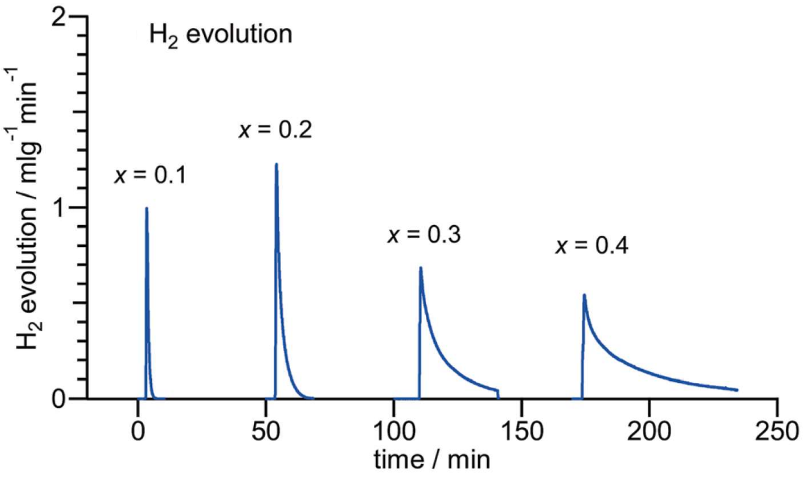

Figure 5.2-2 Impact of strontium substitution in La1-xSrxMnO3-δ on thermochemical water splitting during a 1400-800ºC cycle. The oxidation times at 800ºC were 8, 16, 36, and 65 min respectively. **[55]**

5.2.2.2 Low Temperature Thermokinetic Limit

Comparing the experimentally determined low temperature oxidation of the LSM composition series to the oxidation productivity computed by the thermokinetic model will demonstrate if the materials are cycling under thermodynamically limited conditions or kinetically limited conditions. In order to compute the hydrogen productivity via the thermokinetic model, accurate nonstoichiometry thermodynamics are necessary. Bork et al. recently published work providing such data [58]. They use Computer Coupling of Phase Diagrams and Thermochemistry (CALPHAD) to decrease the uncertainty in the current literature nonstoichiometry results and defect models. They provided the nonstoichiometry thermodynamic data for LSM91, LSM82, LSM73, and LSM64 in the form of enthalpy and entropy as a function of nonstoichiometry over the appropriate range. The results of the CALPHAD model are depicted in **Figure 5.2-3**. Note that the data for LSM91 extends to a nonstoichiometry of 10^{-6}, while the other only extend to 10-

3. The sudden trends developing in this low nonstoichiometry region are a result of the material thermodynamics transitioning from oxygen deficiency to oxygen excess. Only the LSM91 experiences nonstoichiometries in this region under the thermochemical cycling conditions of interest and thus, the thermodynamics in this region were not calculated for the other materials. When modeling the hydrogen production behavior, the profile will truncate when the material's nonstoichiometry reaches 10^{-6}. This corresponds to a hydrogen production rate of around 0.003 mL/min/g, which is below the experimentally detectable limits and thus the missing hydrogen from the model is not of concern.

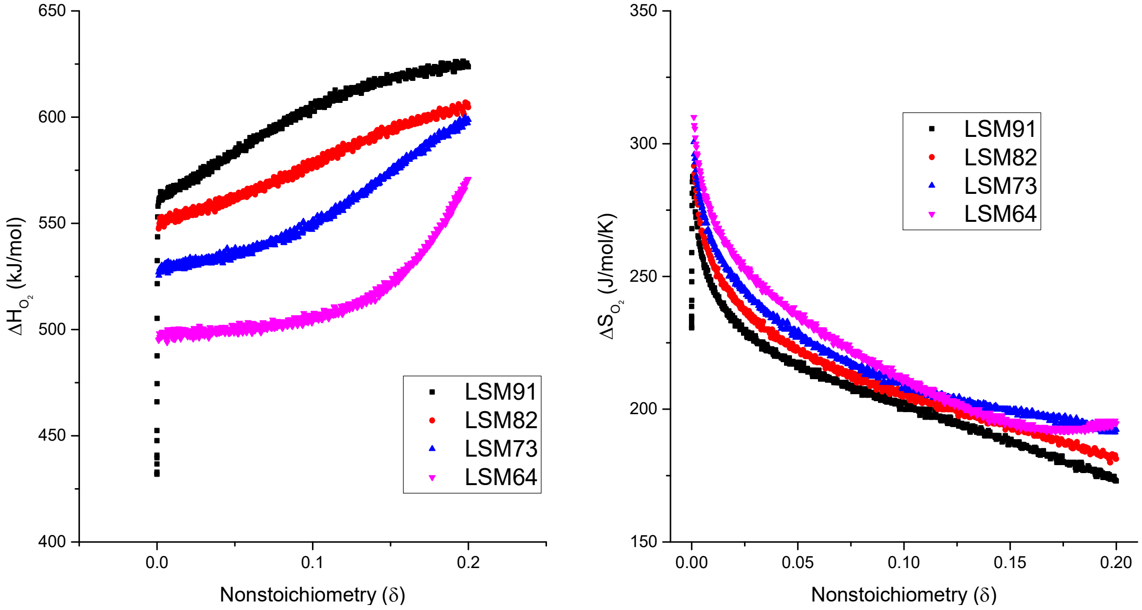

FIGURE 5.2-3 CALPHAD computed enthalpy and entropy of LSM compounds with varying strontium content as a function of nonstoichiometry.

Knowing the enthalpy and entropy as a function of nonstoichiometry allows the equilibrium partial pressure of oxygen to be calculated for a given temperature and nonstoichiometry via the equilibrium expression for an infinitesimal change in nonstoichiometry.

$$\lim_{\varepsilon \to 0} \frac{2}{\varepsilon} La_{1-x}Sr_xMn\ \ _{3-\delta} \Leftrightarrow \frac{2}{\varepsilon} La_{1-x}Sr_xMnO_{3-\delta-\varepsilon} + O_2 \qquad 5.2.2\text{-}1$$

$$\frac{1}{2} ln\left(P_{O_2}(\delta, T)\right) = \frac{-\Delta H_{red}(\delta)+T\Delta S_{red}(\delta)}{RT} \qquad 5.2.2\text{-}2$$

The governing equation (derived in the following Chapter) for the oxidation reaction is given by

$$\boldsymbol{\frac{d\delta_{ox}}{dt} = \frac{F_{ox}}{n_{LSM}}\left(\frac{2P_{O_2}(\delta,T_0)}{\left(P_{tot}-P_{O_2}(\delta,T_0)\right)} - \frac{\chi_{H_2O}K_{H_2O,T_0}}{\left(P_{O_2}(\delta,T_0)^{\frac{1}{2}}+K_{H_2O,T_0}\right)}\right)} \qquad 5.2.2\text{-}3$$

where δ_{ox} is the nonstoichiometry, t is time, F_{ox} is the total molar flowrate of the oxidizing gas, n_{LSM} is the moles of oxide, P_{O_2} is the partial pressure of oxygen, P_{tot} is the total pressure of the system, χ_{H_2O} is the fraction of steam in the oxidizing gas, K_{H_2O,T_0} is the water thermolysis equilibrium constant, and T_0 is the temperature, nominally equal to 800^{o}C.

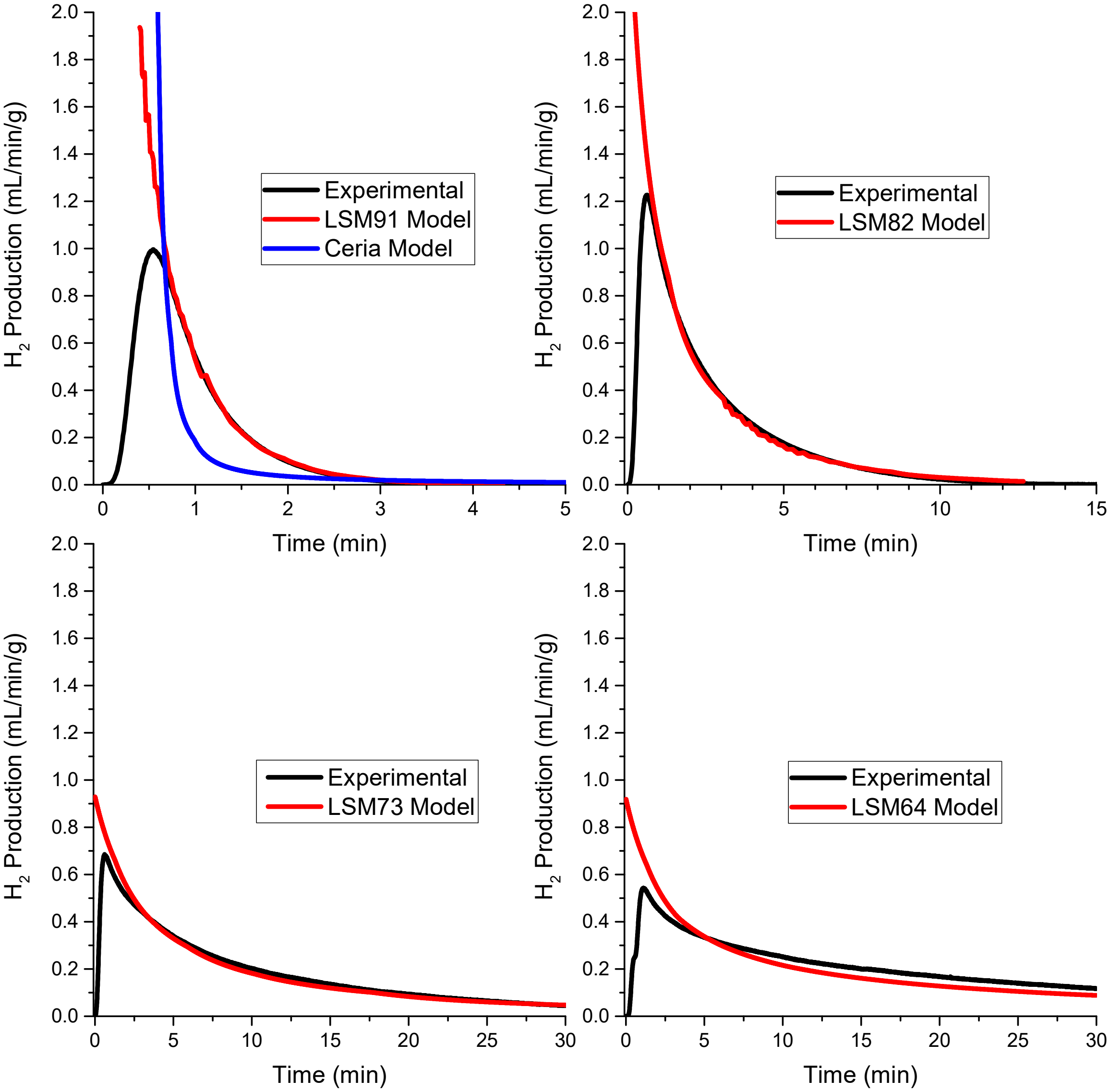

FIGURE 5.2-4 Hydrogen production calculated by the Thermokinetic model compared to experimental data for two temperature cycling of various LSM compounds. Reduction performed nominally at 1400ºC and 10ppm O2 flowed at 1000sccm. Oxidation occurred nominally at 800ºC under 20% steam at 200 sccm. The thermokinetic limit model for ceria is overlaid with the LSM91 data for comparison.

Figure 5.2-4 shows the experimental data compared to the thermokinetic model calculated for LSM and for ceria as a comparison. The ceria model will look identical when compared to each LSM composition; however, due to the longer time scales of higher strontium content samples the ceria data would look like a step change. The IR furnace used for these experiments has a temperature uncertainty of approximately 50ºC. This information was not recorded at the time of the experiment and consequently the model temperature was varied to promote agreement with the experimental data within this range. The specific reduction temperatures used for the models was 840ºC, 795ºC, 810ºC, and 800ºC for LSM91, LSM82, LSM73, and LSM64 respectively. The reduction temperatures used were 1385ºC, 1440ºC, 1440ºC, and 1400ºC for LSM91, LSM82, LSM73, and LSM64 respectively. Also due to the time delay from when the solenoid valves switch to when the gas actually reaches the reactor and the mass spectrometer, the model is delayed by 0.4 minutes. This was only relevant for the LSM91 sample because the entire reaction occurs over such a short time scale. In general the models show poor agreement with the experimental at very low times (until the experimental data peaks) due to the transitioning of the gas. As the strontium content increases, the peak production rates and tails are in worse agreement. This phenomenon, which is most evident in LSM64, where the material underperforms the model at low times and then outperforms at longer times is indicative of a kinetically limited material. Nevertheless, the thermodynamic models calculated using the CALPHAD data represent the upper bound on the LSM material performance. While the LSM theoretical models all have peak production rates below 3 mL/min/g, the ceria model peaks around 58 mL/min/g and finishes fuel production well before any of the LSM materials.

We can now say conclusively that the changing thermodynamics, not kinetics, of LSM when increasing strontium content is the cause of the lengthy reduction times even at lower temperature. Since the thermokinetic limit represents the upper bound on fuel production for a set of cycling conditions, the LSM materials will not exceed the cycling productivity of ceria.

5.2.3 Isothermal Pressure Swing Cycling

Here, the behavior of perovskite-structured oxides are explored as candidates for this cycle. In principle, fuel production capacity can be determined, a priori, from knowledge of the thermodynamic properties of a non-stoichiometric oxide. Accordingly, as a first step, the thermodynamics of various compositions of lanthanum strontium manganite oxides ($La_xSr_{1-x}MnO_3$) were modeled at high temperature from literature data [48]. The theoretical, equilibrium fuel production capacity at 1500°C is found, on the basis of this analysis, to exceed that of undoped ceria, by almost a factor of two (and more than a factor of three at 1400°C). Motivated by this result, samples of x = 0.2, 0.3, and 0.4 were synthesized via solid state reaction and then experimentally evaluated for fuel productivity using in an in-house constructed thermochemical reactor.

5.2.3.1 Experimental Synthesis and Characterization Methods

Pressure-swing cycling studies were carried out using $La_{1-x}Sr_xMnO_{3-\delta}$ (x = 0.2, 0.3, 0.4, 0.5) pellets produced from a solid-state reaction method. Stoichiometric quantities of La_2O_3 (Alfa Aesar, REacton®, 99.99%), $SrCO_3$ (Sigma-Aldrich $99.9%), and $MnCO_3$ (Sigma-Aldrich $99.9%) were combined and attrition-milled in isopropanol for 6 hours at 500 rpm. After drying, the powder was calcined at 1000 °C for 3 hours under air. A porous monolith was fabricated from this powder by mixing the latter with isopropanol (3 ml liquid per gram of powder) to obtain a thick paste. This paste was then placed (without application of pressure) into an alumina cylindrical mold with an inner diameter of 10 mm and fired at 1500 °C for 6 hours under air. The result was porous pellets of mass 0.325 g (65-70% porous), two of which were used in the reactor. **Figure 5.2-5** shows SEM images of the pellets before thermochemical cycling. The particle size and overall porosity are independent of dopant concentration.

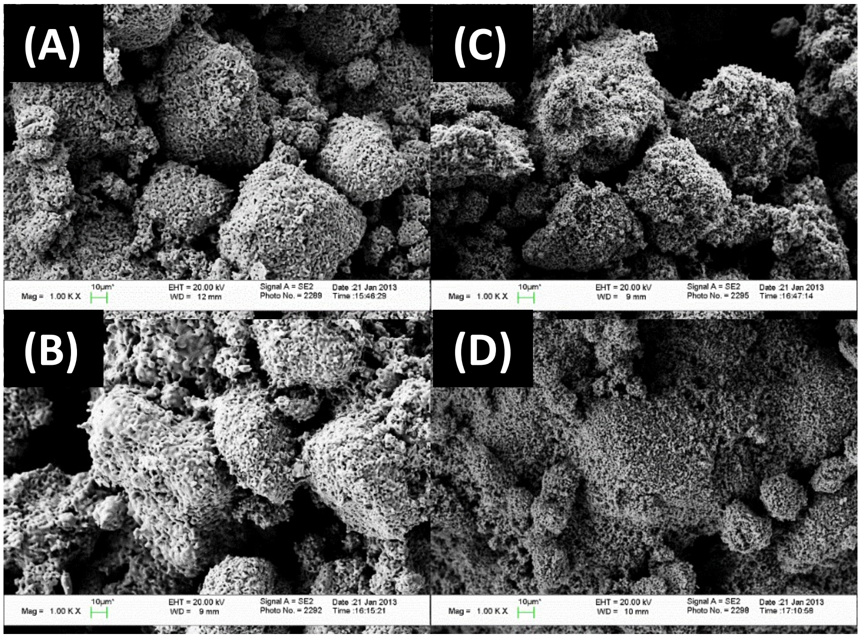

FIGURE 5.2-5 SEM micrographs depicting the microstructure of LSM samples. A, B, C, and D are 20%, 30%, 40%, and 50% strontium doped respectively.

The ceria experiments were conducted using CeO_2 fiberboard blocks were obtained from Zircar Zirconia, Inc. with bulk density of 125 lb ft^{-3} corresponding to overall porosity of ~73%. Blocks were broken into irregular pieces with an edge length in the range of 1.19 – 2.38 mm. A collection of pieces with a mass of 0.65 g was loaded into a horizontal alumina tube reactor (9.5 mm diameter), in turn, placed inside a high-temperature electric furnace (Lindberg/Blue M STF54434C with controller model CC59256PCOMC). The furnace was ramped to 1500 °C (at 10 °C min^{-1}) and held at 1500 °C for the duration of the experiments. Calibration of the temperature within the alumina tube with an external thermocouple indicated that the temperature in the alumina tube at the position of the sample was uniform at 1500 ± 2 °C. Digital mass flow controllers delivered 10 ppm O_2 in Ar gas at 300 sccm to the reactor during the reduction half-cycle. Oxidation was carried out using an atmosphere of 20% H_2O in Ar, achieved by passing dry Ar through a bubbler inside a temperature-controlled oven at 60 °C prior to its delivery to the reactor. The flow rate into the bubbler was fixed at 240 sccm. Gas flow rates were calibrated by a primary air flow calibrator. All gas flow rates and volumes are referenced to 0 °C and 1 atm. Gases were obtained at UHP purity from Air Liquide. Effluent gas composition was measured using a Pfeiffer Omnistar GSD320 quadrupole mass spectrometer after passing through a condenser held at 1 °C. Quantification of the mass spectrometry data was achieved by a five- or six-point calibration with known compositions of hydrogen and oxygen in Ar. A zirconia pellet with Rh particles was placed downstream of the reaction zone at about 700°C to induce recombination of hydrogen and oxygen produced by the autodissociation of water at 1500 °C which otherwise results in a high H_2 and O_2 background signal. The Rh coating was achieved by incipient wetness impregnation; an aqueous solution of $RhNO_3 \cdot 2H_2O$ (99.9%, Alfa Aesar) was applied three times. The final Rh loading was approximately 2% by weight. After 24 hours of short cycles to ensure steady-state operation of the reactor, the sample was allowed to equilibrate with the oxidation atmosphere atmosphere. Reduction was then carried out for a period of 4 h, over which time the material reached (near) equilibrium with the reduction gas atmosphere. The subsequent oxidation half-cycles were carried out for a period of 60 min.

5.2.3.2 Results and Discussion

Before performing thermochemical cycling measurements, on the LSM material series, it is important to understand the fuel production capacity for these materials. While the thermodynamic data available for LSM materials are not suitable for detailed prediction of high temperature behavior, the differences from ceria are such that direct thermochemical cycling was deemed valuable. An estimate of the fuel productivity expected for LSM compositions under isothermal, pressure-swing cycling at 1400^{o}C and 1500^{o}C is summarized in **Figure 5.2-6**. The prediction method is discussed in Chapter 3 and is based on lower temperature, moderate-quality thermogravimetric data reported by Mizusaki et al. [48], and presumes complete equilibration with 10 ppm O_2 (balance Ar) in the reduction step and complete oxidation by 20% H_2O (balance Ar) in the oxidation step, thus represents the thermodynamic limit based on extrapolated behavior. While the uncertainty is high, significantly greater fuel quantities are expected from high Sr-content LSM materials than from ceria. The large increase in fuel production from Ceria to higher strontium content perovskites is largely the result of distinctly different thermodynamic characteristics.

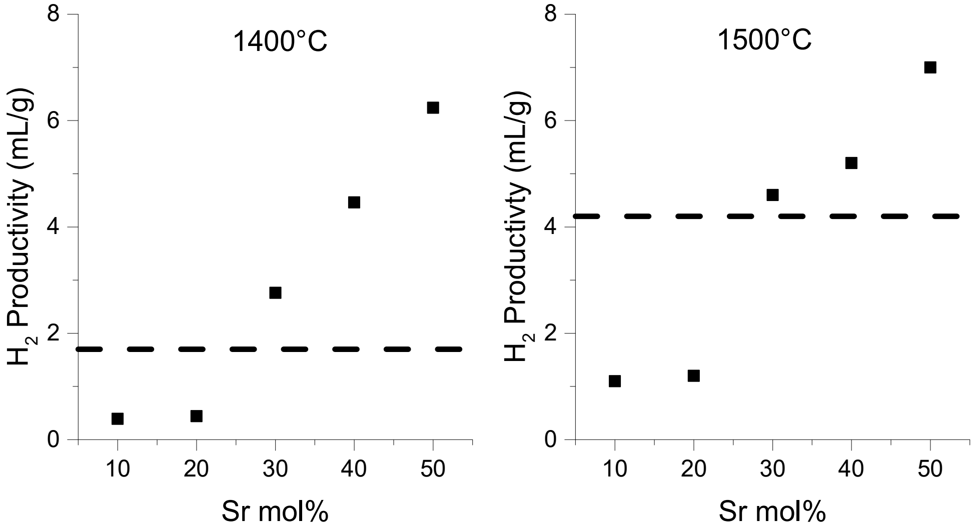

FIGURE 5.2-6 Theoretically estimated hydrogen production per pressure-swing cycle at 1400ºC (left) and 1500ºC (right). The dashed lines denote the productivity of neat ceria.

While the x = 0.2 composition would appear undesirable (**Figure 5.2-6**), the anomalous prediction for this particular composition suggests some problem with the literature thermodynamic data, motivating inclusion of this composition in the present investigation. Each sample was held at temperature for 24 hours while cycling the gas atmospheres to allow the thermochemical test station to reach equilibrium.

The results from these experiments are summarized in **Figure 5.2-7** and **Figure 5.2-8**. The raw gas evolution profiles The figures below show the first 200 min of characteristic four hour oxygen evolution steps and the first 20 min of the following one hour hydrogen production steps for each of the samples.One point of interest denoted in the table below is that the LSM82 sample produced over 200% of the expected oxygen and hydrogen in a cycle. The remaining production amounts are within 80-90% of the theoretical value which is reasonable given the actual reduction P_{O2} is slightly larger due to leaks.

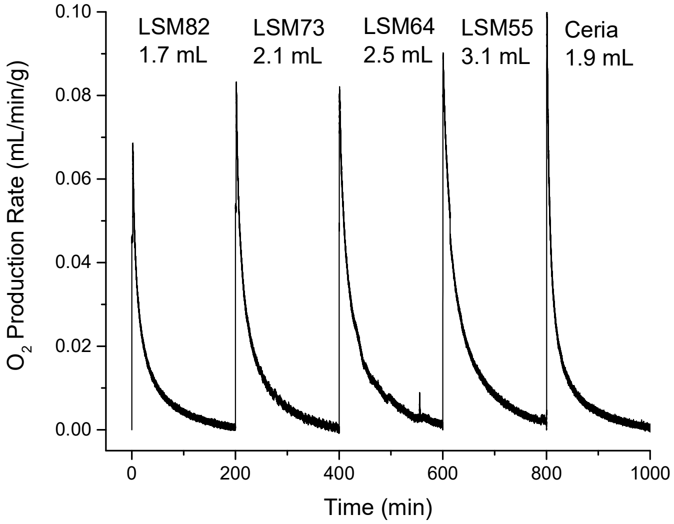

FIGURE 5.2-7 Characteristic oxygen production curves during reduction under 300 sccm 10ppm oxygen from complete oxidation under 20% steam. The integrated oxygen amounts are denoted above each curve.

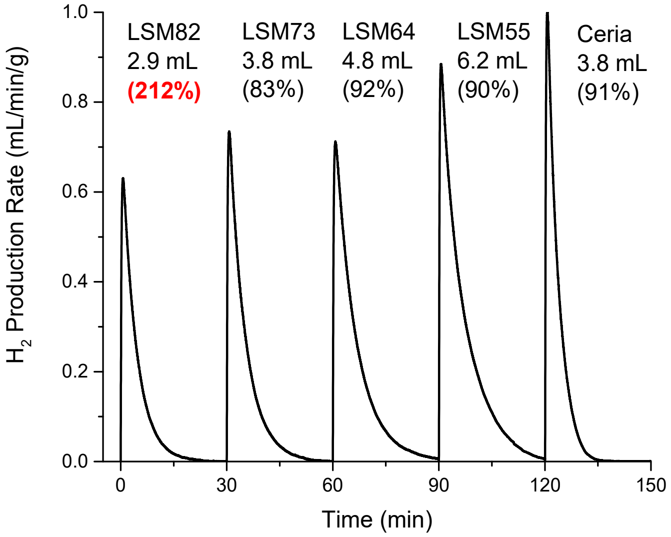

FIGURE 5.2-8 Characteristic hydrogen production curves during oxidation under 300 sccm of 20% steam from four-hour reduction 10pm oxygen. The integrated oxygen amounts are denoted above each curve with percent of theoretical max denoted in parenthesis.

From the kinetic analyses featured in **Figure 5.2-9**, it is clear that increasing the strontium content of LSM results in a larger fuel production capacity and more sluggish kinetics on the oxidation and reduction reactions. This is evidenced by the increasing peak production rates with strontium content. At this stage it is unclear whether the increase in peak production rate is due to the enhanced thermodynamic capacity for fuel production provided by additional strontium or if the surface reaction constant for the material is increased with additional strontium. Unfortunately, the perovskite materials do not achieve peak production rates comparable to that of neat ceria. The reduction reactions for each material all exhibit similar peak production rates, indicating that LSM might not provide a greater efficiency than ceria, since the length of the reduction must be very long to see the benefit in the oxidation.

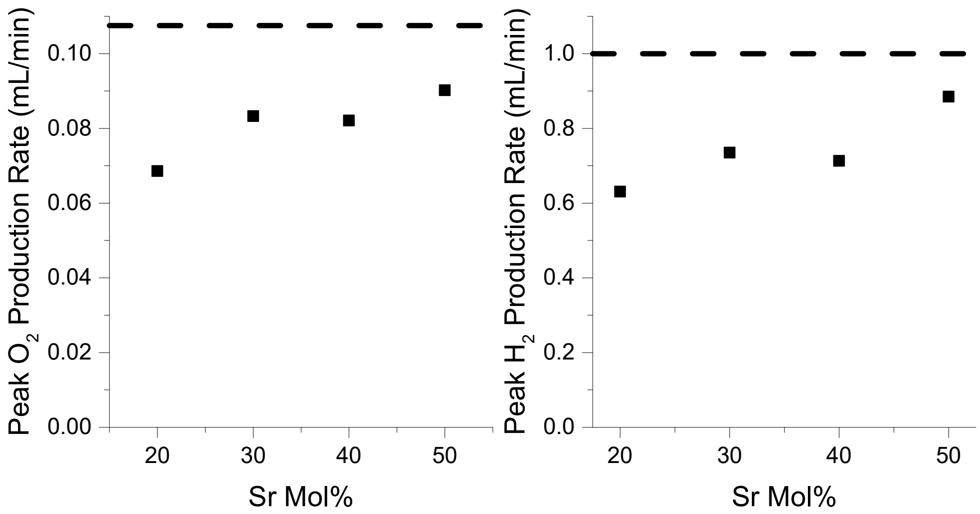

FIGURE 5.2-9 Peak oxygen and hydrogen production rates as a function of strontium content. The peak production rate for neat ceria is denoted by the black line.

When examining the cumulative oxygen production profiles for each of the materials in **Figure 5.2-10** it is clear to see that the higher strontium content materials evolve more oxygen than neat ceria as predicted from the thermodynamic extraction. More importantly, at longer finite times (30+ min) the LSM64 and LSM55 compounds evolve more oxygen than ceria on an absolute basis. This higher average oxygen evolution rate is advantageous for reactor design as it corresponds to a greater average hydrogen production rate for equal times. Similarly, in **Figure 5.2-11** it is clear to see that the greater strontium content perovskite materials produce more fuel than neat ceria. At very short times (less than 3 minutes) ceria produces more fuel on an absolute basis than any of the perovskite materials. After five minutes of oxidation, LSM55 produces more hydrogen than ceria on an absolute basis, but at that point in time ceria's oxidation half cycle is approximately 80%, while that of LSM55 is only 45% complete.

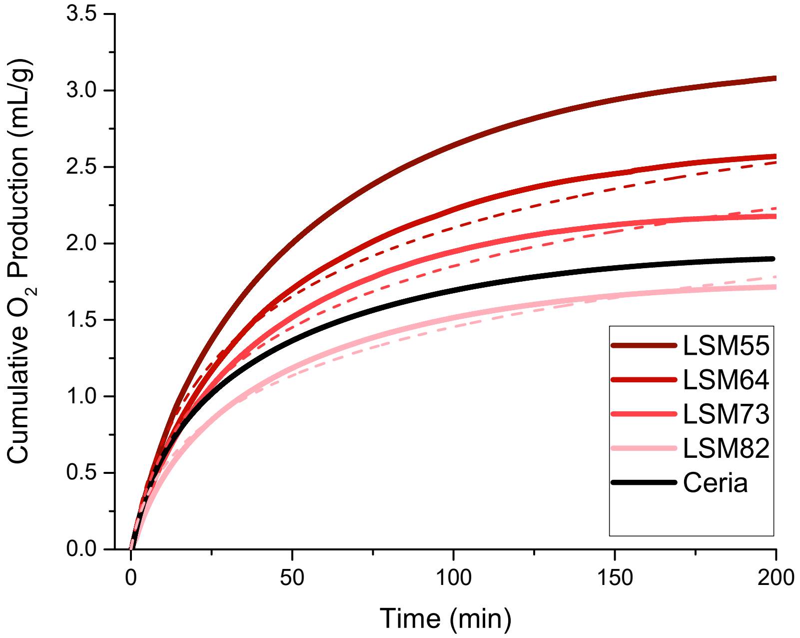

FIGURE 5.2-10 Cumulative oxygen production during the reduction half-cycle under 10ppm oxygen from full oxidation under 20% steam. Dashed lines represent the thermokinetic model.

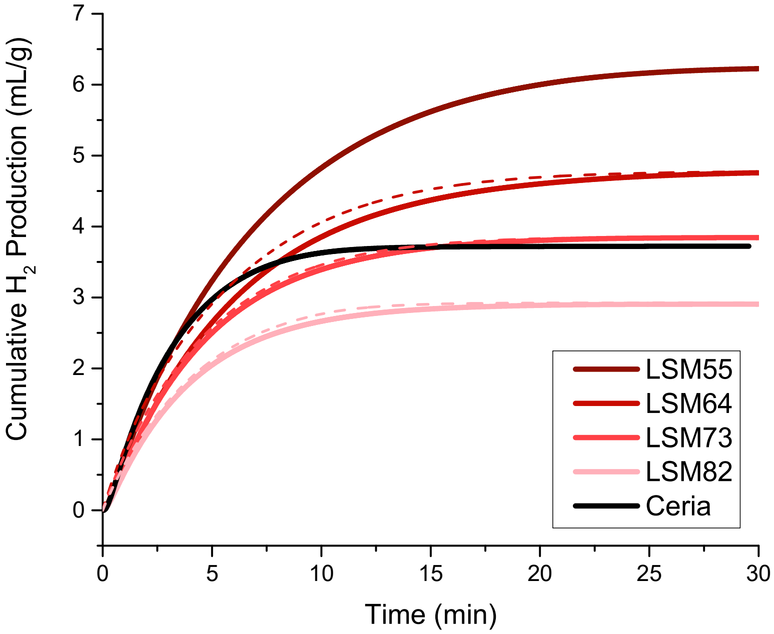

FIGURE 5.2-11 Cumulative hydrogen production during one-hour oxidation under 20% steam following four-hour reduction under 10ppm oxygen. Dashed lines represent the thermokinetic model.

Thus in an isothermal pressure-swing cycle between Ar (with 10 ppm oxygen) and 20% steam (balance Ar) at 1500°C shows that indeed the series of materials offer higher fuel production capacity under conditions of long-cycle times. In addition, oxygen release rates are higher for the perovskites than they are for ceria, indicating that more fuel is produced for a given cycle with finite periods. One remaining concern with the perovskite materials is the high temperature decomposition observed by Mizusaki et al. Here there was no visible evidence in the reactor of such decomposition and post mortem SEM micrographs showed only minor agglomeration of particles. Nevertheless, a long term thermochemical cycling experiment to test for microstructure and phase stability is warranted.

It is expected that under isothermal pressure-swing cycling, both the oxygen and hydrogen production profiles will be governed by the gas flow and should match the thermokinetic model well. This behavior is observed for each of the hydrogen profiles. The oxygen profiles, however, experimentally exceed the theoretical maximum evolution rate. An explanation for this is discussed further in the subsequent chapter for the LSM55 composition.

5.2.4 Conclusion

Perovskite materials generally exhibit a larger range of nonstoichiometries than fluorite structured materials at corresponding temperature and oxygen partial pressure ranges. Here the perovskite system $La_{1-x}Sr_xMnO_3$ was investigated for both two temperature cycling and isothermal pressure swing cycling. In pressure swing cycling the capacity of LSM for fuel production increased with increasing strontium content and for compositions with greater than 30% strontium on the A site, the capacity for fuel production exceeded that of neat ceria. During high temperature reduction, LSM evolves more oxygen than neat ceria for finite cycling times. The high temperature oxidation kinetics of all the LSM compounds are slower than that of neat ceria, likely due to thermodynamic limitation. In two temperature cycling LSM exhibits significantly reduced kinetics with increasing strontium content at low temperature oxidation. Even at low temperatures, these materials are thermodynamically limited during oxidation. Even with infinitely fast kinetics, the oxidation performance of the LSM materials studied is much slower than that of neat ceria. It is suspected that the lower enthalpy results in an inefficiency for the materials to reoxidize. In reactor systems this would result in very poor steam utilization, which is a major cost factor towards overall efficiency. Consequently, the perovskite materials are not recommend for larger scale two temperature reactor operation, but if thermally stable could be used for large scale isothermal pressure swing cycling.

5.3 Ideal Material Thermodynamics

In the previous sections, examples of materials that do not provide significant gas production benefits beyond that of neat ceria have been evaluated. In the case of the praseodymium and terbium doped samples, it was due to a weak thermodynamic driving force, and in the case of samarium it was due to a decreased capacity for fuel production. It would be useful to establish guidelines for the optimal material thermodynamics that will result in a direct benefit to the thermochemical cycling process – in particular, what functional forms of the nonstoichiometry lines will result in the highest average hydrogen production rate during a cycle. For the purposes of this investigation, the material is assumed to have infinitely fast kinetics, and the limitation for gas evolution is dictated by the nonstoichiometry thermodynamics. Under these conditions, the oxygen evolution during reduction and hydrogen production during oxidation are governed by **Equations 2.4.2-7** and **2.4.2-21**, respectively. The full derivations are provided in Chapter 2.

The hypothetical materials will be subjected to an isothermal pressure-swing cycle at 1500°C with 10 ppm O_2 in argon and pure steam as the reduction and oxidation conditions, respectively. The total flowrate is 100 sccm for both the reduction and oxidation, and the cycles are calculated for samples of equal number of moles, which will result in constant total hydrogen production.

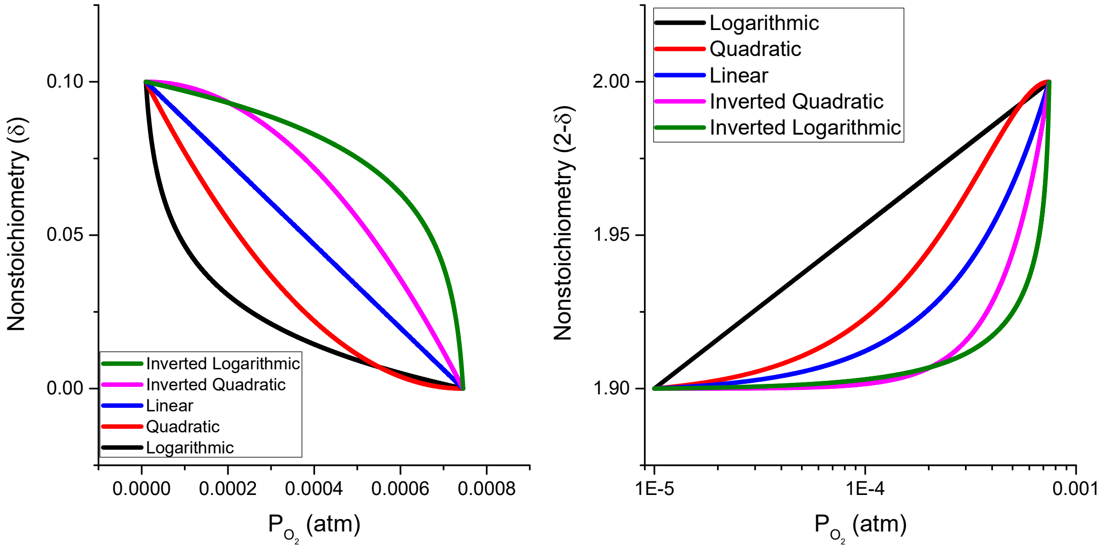

FIGURE 5.3-1 Nonstoichiometry isotherms for various functional forms. The left image indicates the concavity of each curve, while the right image shows the isotherms plotted as 2-δ in the more traditional log-scale format.

Since the total amount of hydrogen produced will be constant for each model, the maximum average hydrogen production rate will be achieved by minimizing the total cycle time for the reduction and oxidation. In earlier experiments, the time for each material to reach equilibrium under reduction is orders of magnitude longer than the time to reach equilibrium under oxidation. All of the materials investigated so far have nonstoichiometry lines that can be approximated by a logarithmic dependence of nonstoichiometry on oxygen partial pressure. In particular, the nonstoichiometry lines are all concave up (when plotted in an absolute sense versus δ, rather than 2-δ). Increasing the curl of these lines would only increase the reduction time and decrease the oxidation time proportionally, resulting in lower average hydrogen production. The nonstoichiometric curves were chosen such that the concavity decreased towards zero, and then the symmetric curves were examined to explore what happens when the concavity's parity is changed. **Table 5.2.4-1** below outlines the exact functional forms used for the models.

TABLE 5.2.4-1 List of the exact equations for nonstoichiometry as a function of P_{O2}

Function	Equation	A	B	C
Logarithmic	$\delta = A*\log_{10}(P_{O2}) + B$	-5.341E-2	-0.1670	-
Quadratic	$\delta = A*(P_{O2})^2 + B*P_{O2} + C$	1.849E5	-275.6	0.1027
Linear	$\delta = A*P_{O2} + B$	-136.0	0.01014	-
Inverted Quadratic	$\delta = -A*(P_{O2})^2 + B*P_{O2} + C$	-1.849E5	3.700	0.09998
Inverted Logarithmic	$\delta = -A* \log_{10}(7.554E\text{-}4 - P_{O2}) + B$	5.341E-2	0.2670	-

Each function was fit to two points. The oxygen partial pressure values were dictated by the equilibrium P_{O2} of the reducing and oxidizing conditions: 10^{-5} atm and 7.554×10^{-4} atm, respectively. The nonstoichiometries at these values were chosen to be 0.01 and 0.1, respectively, so that one order of magnitude in nonstoichiometry was experienced. The functions must all exhibit a monotonic decrease in nonstoichiometry between the two points, otherwise the reaction would stop at an intermediate equilibrium. The linear and logarithmic curves were fit to these points using standard methods. The quadratic vertex was fixed at the oxidation condition, while the inverted quadratic's vertex was specified at the reduction condition. The inverted logarithmic equation was determined by rotating the logarithmic equation 180° around the point ($P_{O2}=3.827*10^{-4}$, $\delta=0.05$).

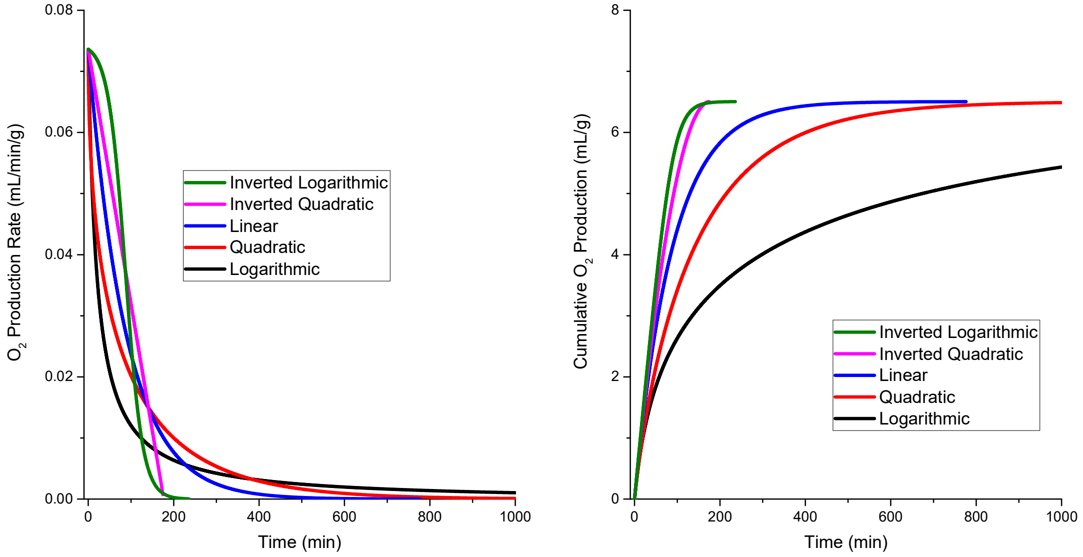

FIGURE 5.3-2 Oxygen evolution profiles (left) and cumulative oxygen evolution curves (right) for various nonstoichiometric isotherms from an isothermal pressure-swing cycle at 1500°C under 10 ppm O_2 in argon at 100 sccm.

The profiles for the oxygen evolution of each model are depicted on the left side of **Figure 5.3-2**. One point of interest is the oxygen evolution profile for the inverted quadratic curve, which is linear. This is expected because, in this case, the rate of production is proportional to the zeroth order of nonstoichiometry. The essential observation is that the amount of time for each model to reach equilibrium with the reduction condition increases as the slope of the nonstoichiometry curve at the oxidation point increases (becomes more negative). The hydrogen production profiles in **Figure 5.3-3** exemplify a similar pattern around the oxidation and reduction points, respectively. Thus, we can conclude that concave up curves will benefit the oxidation reaction, while concave down curves will benefit the reduction reaction.

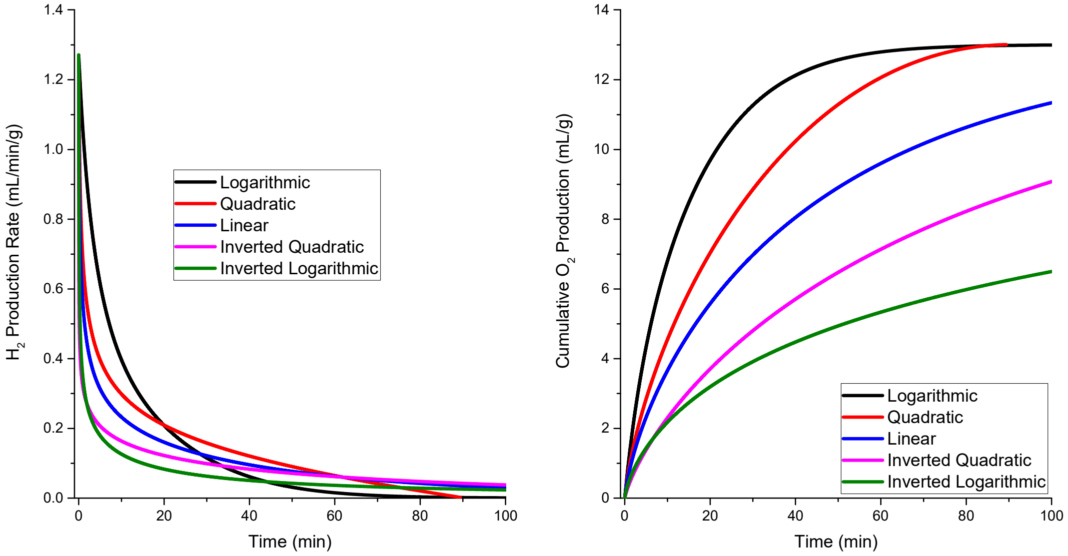

FIGURE 5.3-3 Hydrogen evolution profiles (left) and cumulative hydrogen evolution curves (right) for various nonstoichiometric isotherms from an isothermal pressure-swing cycle at 1500ºC under 10 ppm O_2 in argon at 100 sccm.

Because of the tradeoffs observed between the oxidation time and the reduction time, the ideal material will take equal time to oxidize and reduce. In this study, the linear model comes closest to balancing the two half reactions. The complete cycle then, calculated to 99.99% of equilibrium for each half step, would take 1300 minutes. The time for each half reaction is not equal, as roughly 65% of the time is spent reducing and 35% oxidizing. **Figure 5.3-4** displays the average hydrogen production for each model. In all cases, as the curl of the nonstoichiometry lines increase, the average hydrogen production rate decreases. Material discovery should therefore be aimed at materials that will exhibit close-to-linear hydrogen production rates.

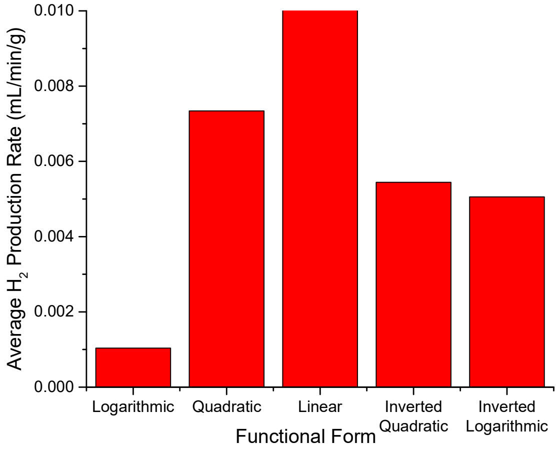

FIGURE 5.3-4 Average hydrogen production rate for a complete isothermal pressure-swing cycle at 1500°C for various functional forms of nonstoichiometry.

5.4 Conclusion

The novel material investigation for solar-driven thermochemical fuel production was met with mixed success. The praseodymium and terbium doped samples do show a larger capacity for fuel production than neat ceria. However, the oxidation and reduction of Pr and Tb occur too slowly to yield a measureable amount of hydrogen. The samarium doped ceria does exhibit slightly higher peak production rates, but this is compromised by its reduced capacity for fuel production. **Table 5.2.4-1** summarizes the production capacities for the materials discussed in this chapter for both hydrogen and carbon monoxide under isothermal pressure swing cycling. Note that the nonstoichiometry values for samarium doped ceria are significantly higher due to the intrinsic vacancies that do not participate in the cycle.

TABLE 5.2.4-1 Capacity for isothermal fuel production of SDC15, 10TCO, and 10PCO in comparison to neat ceria

Parameter	Ceria	10TCO	10PCO	SDC15
δ, reduction, 10^{-5} atm pO_2	0.067	0.101	0.109	0.133
δ, H_2O oxidation, 20% H_2O	0.034	0.070	0.080	0.109
$\Delta\delta$, H_2O cycle	0.033	0.031	0.029	0.024
H_2, ml/g	4.4	4.0	3.7	3.1
δ, CO_2 oxidation, 100% CO_2	0.023	0.058	0.068	0.097
$\Delta\delta$, CO_2 cycle	0.044	0.043	0.041	0.037
CO, ml/g	5.7	5.5	5.4	4.8

It was determined that the logarithmic nature of the dependence of nonstoichiometry on oxygen partial pressure causes the lengthy reduction times. Further material discovery should be aimed at finding materials that exhibit a more linear dependence of nonstoichiometry on oxygen partial pressure. This behavior is found when oxygen atoms are incorporated into the interstitial sites of a lattice structure. Unfortunately, interstitial oxygen atoms typically only exist at higher pressures, and, in addition, interstitial atoms exhibit diminished mobility throughout the bulk of the material.

Chapter 6 Thermokinetic Limit with Axial Nonstoichiometry Variation

6.1 Axial Nonstoichiometry Variation

In developing the thermokinetic model with axial nonstoichiometry variation, the assumption that the entire oxide reactive element has a uniform nonstoichiometry is relaxed. If the material's surface reaction kinetics are exceptionally fast relative to the gas flow through the reactor and the ionic diffusion in the bulk of the material, then one expects the upstream end of the sample to begin reacting before the downstream edge, resulting in a nonstoichiometric gradient in the axial direction. As an example, in the reduction half cycle, the first plug of gas entering the reactor reduces the front portion of the sample such that it reaches equilibrium. Then that plug moves on to interact with the next section of the sample. Finally, the plug of gas reaches equilibrium with the last segment of the sample and exits the reactor. Since the plug of gas interacts with successive segments of the reactive element, which are each fully oxidized, the plug of gas is able to uptake significantly larger amounts of oxygen than if it interacted with the whole reactive element at once. Thus, each plug of gas is able to draw more oxygen from the oxide, resulting in a higher gas evolution rate through the duration of the half cycle. In order to derive the governing equations for this behavior, a shell balance is employed in the axial direction.

6.1.1 Reduction

The reduction half cycle is considered first. For an arbitrary volume element in the oxide, we can perform a mole balance on oxygen. For a reactive element of length Δz, the difference between the molar flow rate of oxygen in and out is how much oxygen evolved due to reaction with the oxide in the small volume element.

$$\boldsymbol{F_{O_2}\big|_{z+\Delta z} - F_{O_2}\big|_{z} = r_{O_2}\big|_{\Delta V}} \qquad \textbf{6.1.1-1}$$

The moles of oxygen generated in the control volume can be expressed in a form analogous to **Equation 2.4.2-3**.

$$\boldsymbol{r_{O_2}\big|_{\Delta V} = \frac{\Delta z}{L}\frac{n_{CeO_{2-x}}}{2}\frac{d\langle\delta\rangle_{\Delta V}}{dt}} \qquad \textbf{6.1.1-2}$$

where $\langle\delta\rangle_{\Delta V}$ is the average nonstoichiometry of the oxide in the control volume and can be expressed formally as,

$$\boldsymbol{\langle\delta\rangle = \frac{1}{\Delta z}\int_{z}^{z+\Delta z}\delta(z')dz'} \qquad \textbf{6.1.1-3}$$

The molar oxygen flowrate at the upstream and downstream ends of the control volume can be expressed as fractions of the total molar flowrate, based on the partial pressure of oxygen at that point. Thus, the total molar flow at position z and z+Δz is expressed below.

$$\boldsymbol{F_{O_2}\big|_{z} = \frac{P_{O_2}(\delta(z))}{P_{tot}}\mathrm{F}|_{z}} \qquad \textbf{6.1.1-4}$$

$$\boldsymbol{F_{O_2}\big|_{z+\Delta z} = \frac{P_{O_2}(\delta(z+\Delta z))}{P_{tot}}\mathrm{F}|_{z+\Delta z}} \qquad \textbf{6.1.1-5}$$

Additionally, the total flowrate exiting the control volume is equal to the flowrate entering plus the moles generated in the control volume.

$$\mathrm{F}|_{z+\Delta z} = \left(\mathrm{F}|_z + \frac{\Delta z}{L}\frac{n_{CeO_2}}{2}\frac{d\langle\delta\rangle}{dt}\right) \qquad \textbf{6.1.1-6}$$

By substituting **Equations 6.1.1-2** and **6.1.1-4** through **6.1.1-6** into **Equation 6.1.1-1**, combining like terms and taking the limit as Δz goes to zero, the following relation is produced.

$$\frac{n_{CeO_{2-x}}}{2L}\left(P_{tot} - P_{O_2}(\delta(z))\right)\frac{d\delta(z)}{dt} = \frac{\partial P_{O_2}(\delta(z))}{\partial z}\mathrm{F}|_z \qquad \textbf{6.1.1-7}$$

The only remaining unknown term is $\mathrm{F}|_z$, the total molar flow rate at an arbitrary position in the oxide. This can be calculated by performing a macroscopic balance on the oxide. Since we know the total flow at the front edge of the oxide, F_{red}, the total exiting the reactor will be the sum of the initial flowrate and the amount of oxygen generated by the oxide.

$$F_{out} = \left(F_{red} + \frac{n_{CeO_2}}{2}\frac{d\delta}{dt}\right) \qquad \textbf{6.1.1-8}$$

By rearranging **Equation 6.1.1-7**, substituting for $\frac{n_{CeO_2}}{2}\frac{d\delta}{dt}$, and combining like terms, the following relation between the flow exiting the reactor and the flow entering the reactor can be determined. This relation is analogous to equating the flow at a specific position to the nonstoichiometry at that position.

$$F_{out} = F_{red}\frac{\left(P_{tot}-P_{O_2 in}\right)}{\left(P_{tot}-P_{O_2}(\delta)\right)} \Leftrightarrow \mathrm{F}|_z = F_{red}\frac{\left(P_{tot}-P_{O_2 in}\right)}{\left(P_{tot}-P_{O_2}(\delta(z))\right)} \qquad \textbf{6.1.1-9}$$

Substituting this relation into **Equation 6.1.1-7** and simplifying yields the governing equation for the reduction half cycle with axial nonstoichiometry variation.

$$\frac{d\delta(z)}{dt} = \frac{2L*F_{red}}{n_{CeO_2}} \frac{\left(P_{tot} - P_{O_2 in}\right)}{\left(P_{tot} - P_{O_2}(\delta(z))\right)^2} \frac{\partial P_{O_2}(\delta(z))}{\partial z} \qquad \textbf{6.1.1-10}$$

As a check on this derivation, the rate of nonstoichiometry change can be averaged over the length of the oxide, yielding the governing equation for the reduction half cycle in the case of uniform nonstoichiometry.

$$\frac{1}{L}\int_0^L \frac{d\delta(z)}{dt} dz = \frac{2F_{red}}{n_{CeO_2}} \left(P_{tot} - P_{O_2 in}\right) \int_0^L \frac{1}{\left(P_{tot} - P_{O_2}(\delta(z))\right)^2} \frac{\partial P_{O_2}(\delta(z))}{\partial z} dz \qquad \textbf{6.1.1-11}$$

As a result of the integration, the following relation, which is analogous to **Equation 2.4.2-7** is realized.

$$\langle \frac{d\delta}{dt} \rangle = \frac{2F_{red}}{n_{CeO_2}} \frac{\left(P_{O_2}(\delta(z=L)) - P_{O_2 in}\right)}{\left(P_{tot} - P_{O_2}(\delta(z=L))\right)} \qquad \textbf{6.1.1-12}$$

6.1.2 Oxidation

The derivation for the oxidation half cycle will be similar to the reduction case, but with the inclusion of gas phase water thermolysis. As before in **Equation 6.1.1-1**, a molar oxygen shell balance on a small volume element of the oxide is performed. Now the oxide acts as an oxygen sink in the control volume and the thermolysis reaction in the gas phase is a source. Note that since the nonstoichiometry is decreasing throughout the half reaction, $\frac{d\langle\delta\rangle}{dt}$ is a negative quantity.

$$r_{O_2}\Big|_{\Delta V} = \frac{\psi|_{z+\Delta z} - \psi|_z}{2} F_{H_2O}\Big|_z + \frac{\Delta z}{L} \frac{n_{CeO_2}}{2} \frac{d\langle\delta\rangle}{dt} \qquad \textbf{6.1.2-1}$$

The additional amount of oxygen generated in the control volume from the thermolysis reaction is one half the molar conversion of water from the upstream edge of the control volume to the downstream edge. As before in **Equations 6.1.1-4** and **6.1.1-5**, the molar flow rate of oxygen scales linearly from the total molar flow rate based the oxygen partial pressure. The molar flow rates of hydrogen and water also scale linearly with the total flow rate based on the partial pressures of hydrogen and steam, respectively.

$$\boldsymbol{F_{H_2O}}\Big|_z = \chi_{H_2O}\boldsymbol{F}|_z \qquad \textbf{6.1.2-2}$$

The change in moles from the two reactions causes an increase in total molar flow rate across the control volume. This can be express in an analogous form to **Equation 2.4.2-17**.

$$\mathbf{F}|_{z+\Delta z} = \left(\mathbf{F}|_z + \frac{\psi|_{z+\Delta z} - \psi|_z}{2}\boldsymbol{F_{H_2O}}\Big|_z + \frac{\Delta z}{L}\frac{n_{CeO_2}}{2}\frac{d\langle\delta\rangle}{dt}\right) \qquad \textbf{6.1.2-3}$$

Lastly, as described in **Equation 2.4.2-7**, the total flow rate at the downstream edge of the control volume can be described relative to the initial flow rate entering. This will be the upstream flow rate plus the added moles from the thermolysis reaction minus the consumption reaction. Due to the stoichiometry of the water thermolysis and oxygen equilibrium with the sample, this change is simply equivalent to the amount of oxygen generated. The result of this macroscopic balance is below.

$$\mathbf{F}|_z = \boldsymbol{F_{ox}} + \frac{P_{O_2}(\delta(z))}{P_{tot}}\mathbf{F}|_z \qquad \textbf{6.1.2-4}$$

Combining equations in to the oxygen mole balance yields the following result.

$$\frac{P_{O_2}(\delta(z+\Delta z))}{P_{tot}}\left(\mathbf{F}|_z + \frac{\psi|_{z+\Delta z}-\psi|_z}{2} F_{H_2O}\Big|_z + \frac{\Delta z}{L}\frac{n_{CeO_2}}{2}\frac{d\langle\delta\rangle}{dt}\right) - \frac{P_{O_2}(\delta(z))}{P_{tot}}\mathbf{F}|_z =$$

$$\frac{\psi|_{z+\Delta z}-\psi|_z}{2} F_{H_2O}\Big|_z + \frac{\Delta z}{L}\frac{n_{CeO_{2-x}}}{2}\frac{d\langle\delta\rangle_{\Delta V}}{dt} \qquad \textbf{6.1.2-5}$$

By collecting like terms, dividing by Δz and taking the limit as Δz approaches zero, following governing equation is realized.

$$\frac{d\delta(z)}{dt} = \frac{2L*\mathbf{F}|_z}{n_{CeO_2}}\left(\frac{P_{tot}}{P_{tot}-P_{O_2}(\delta(z))}\right)\left[\frac{1}{P_{tot}}\frac{\partial P_{O_2}(\delta(z))}{\partial z} + \left(1 - \frac{P_{O_2}(\delta(z))}{P_{tot}}\right)\frac{\chi_{H_2O}P_{O_2}(\delta(z))}{2}\frac{\partial\psi}{\partial z}\right] \qquad \textbf{6.1.2-6}$$

The contribution to the overall rate from the oxygen gradient in the oxide and the gas phase, is clear. Rearranging the result of the macroscopic balance in **Equation 6.1.2-4**, and substituting for $\mathrm{F}|_z$ yields the following relation.

$$\frac{d\delta(z)}{dt} = \frac{2L*F_{ox}}{n_{CeO_2}}\left(\frac{P_{tot}}{\left(P_{tot}-P_{O_2}(\delta(z))\right)^2}\right)\left[\frac{\partial P_{O_2}(\delta(z))}{\partial z} + \left(P_{tot} - P_{O_2}(\delta(z))\right)\frac{\chi_{H_2O}P_{O_2}(\delta(z),T_0)}{2}\frac{\partial\psi}{\partial z}\right]$$

6.1.2-7

Equation 2.4.2-20 can be used to eliminate the extent of reaction. Lastly, the chain rule is performed to collect all the partial derivative terms of oxygen partial pressure with respect to axial position.

$$\frac{d\delta(z)}{dt} = \frac{2L*F_{ox}}{n_{CeO_2}}\left(\frac{P_{tot}}{\left(P_{tot}-P_{O_2}(\delta(z))\right)^2}\right)\left[1 + \frac{\chi_{H_2O}K_{H_2O,T}\left(P_{tot}-P_{O_2}(\delta(z))\right)P_{O_2}(\delta(z))}{4\sqrt{P_{O_2}(\delta(z),T_0)}\left(K_{H_2O,T}+\sqrt{P_{O_2}(\delta(z),T_0)}\right)^2}\right]\frac{\partial P_{O_2}(\delta(z))}{\partial z}$$

6.1.2-8

6.2 Application to Reactor Systems

6.2.1 Effects of Gas Phase Diffusion

In order to apply the governing equations derived in the previous sections to actual reactor systems, a finite element method is employed. Without prior knowledge of the oxygen partial pressure gradient throughout the sample, the rate of change of the nonstoichiometry cannot be calculated for each position using Euler's Method. Thus, the system will be treated as a series of reactors, each of which contains a fraction of the oxide material existing with uniform nonstoichiometry. The effluent gas from one reactor becomes the input gas for the subsequent reactor. The underlying assumption here is that each partition of the reactive oxide operates independently from its neighboring partition or equivalently, that the gas phase diffusion dynamics are dominated by forced convection. To assure this is the case the partitions must be large enough that the gas molecules are not diffusing axially between adjacent partitions. More explicitly, the time for the gas to diffuse due to free convection over the length of the pellet should be at least an order of magnitude smaller than the time it takes for the gas molecules to travel the length of the plug due to forced convection. The method for assuring this criterion is satisfied is outlined in this section.

In the case of free convection, the gas phase diffusion coefficient needs to be determined. Correlations for this coefficient have been derived by several sources based on the kinetic theory of gases [59]. These theories all employ the assumption that the gas molecules will interact as hard spheres in perfectly elastic collisions; however, due to the typically high temperatures of thermochemical cycling systems this assumption is not valid. Hirschfelder et al. improved upon the previous models by accounting for influence of molecular forces on the collisions by using the Leonard-Jones potential [60]. This model has a higher order dependence on temperature as well as a pressure dependence. For nonpolar and nonreacting molecules, such as oxygen and argon, the diffusion coefficient of oxygen in argon is expressed by,

$$\boldsymbol{D_{O_2.Ar}} = \frac{\mathbf{0.001858} * \boldsymbol{T^{\frac{3}{2}}} * \sqrt{\frac{1}{M_{O_2}} + \frac{1}{M_{Ar}}}}{\boldsymbol{P} * \boldsymbol{\sigma^2_{O_2,Ar}} * \boldsymbol{\Omega_{\mathrm{D}}}} \qquad \textbf{6.2.1-1}$$

where $D_{O_2.Ar}$ is the mass diffusivity of oxygen through argon in cm^2/s, T is the absolute temperature in Kelvin, M_{O_2} , M_{Ar} are the molecular weights of oxygen and argon, respectively, P is the absolute pressure in atmospheres, $\sigma_{O_2,Ar}$ is the ‘‘collision diameter’’ (a Lennard–Jones parameter) in Å, and Ω_{D} is the ‘‘collision integral’’ for molecular diffusion, a dimensionless function of the temperature and intermolecular potential field for one molecule each of oxygen and argon. The collision diameters of the system are simply the average of each gas species’ collision diameter. The intermolecular potential field, ε, between oxygen and argon is the geometric mean of each molecules self-interacting energy.

$$\boldsymbol{\sigma_{O_2,Ar}} = \frac{1}{2}\left(\boldsymbol{\sigma_{O_2}} + \boldsymbol{\sigma_{Ar}}\right) \qquad \textbf{6.2.1-2}$$

$$\frac{\boldsymbol{\varepsilon_{O_2,Ar}}}{\boldsymbol{k}} = \sqrt{\frac{\boldsymbol{\varepsilon_{O_2}}}{\boldsymbol{k}} \frac{\boldsymbol{\varepsilon_{Ar}}}{\boldsymbol{k}}} \qquad \textbf{6.2.1-3}$$

Tabulated values for the collision diameter, intermolecular potential field, and collision integral were taken from J. R. Welty's Fundamentals of Momentum, Heat, and Mass Transfer [61]. The relevant tabulated parameters are displayed in **Table 6.2.1-1** for a temperature of 1500ºC and a pressure of 1 atm.

TABLE 6.2.1-1 The relevant tabulated and calculated parameters for determining the diffusion coefficient of oxygen in argon.

T	P	M_{O_2}	M_{Ar}	σ_{O_2}	σ_{Ar}	$\sigma_{O_2,Ar}$	$\frac{\varepsilon_{O_2}}{k}$	$\frac{\varepsilon_{Ar}}{k}$	$\frac{\varepsilon_{O_2,Ar}}{k}$	Ω_D	$D_{O_2,Ar}$
1773.15	1	32.00	39.95	3.433	3.418	3.426	113	124	118	0.703	3.99

Experiments in this work were performed on a laboratory scale system where the sample is a cylindrical pellet sitting in a long tube. The gas will predominantly pass in the space between the side of the pellet and the tube inner. The time for a plug of gas to pass over the pellet completely is the length of the pellet divided by the face velocity of the gas passing through the space between the pellet and the tube.

$$t = \frac{L}{v_z} \tag{6.2.1-4}$$

The latter can be calculated by dividing the cross sectional area of the space by the volumetric flow rate. It is important to note that the volumetric flow rate must be scaled up from standard temperature and pressure to the operating temperature.

$$\dot{V} = \pi\left((r_{tube})^2 - \left(r_{pellet}\right)^2\right) v_z \tag{6.2.1-5}$$

$$\dot{V} = \frac{T}{T_{ref}} * \dot{V}_{stp} \tag{6.2.1-6}$$

Now that the residence time for the gas around the pellet is known, the distance that the gas molecules diffuse due to natural convection in the axial direction can be approximated. For this approximation, the length scales by

$$\boldsymbol{L = \sqrt{D_{O_2.Ar} * t}} \qquad \textbf{6.2.1-7}$$

to ensure that the gas plugs of adjacent partitions are non-interacting in this model, the length of a partition is taken to be twice the calculated length that an oxygen or argon molecule can diffuse under free convection. In order to recover the total gas production during the half cycle, the mass weighted average productivity is calcualted for each partition. For both of the following scenarios, the partitions are all of equal mass and the individual partitions need only be averaged together. The calculation is described below, where *n* is the number of partitions.

$$\boldsymbol{O_2\, Production\, Rate\left(\frac{mL}{min*g}\right) = \frac{22400\frac{mL}{mol}}{2*MM_{Oxide}} * \frac{1}{n}\sum_{i=1}^{n}\left(\frac{d\delta}{dt}\right)_i} \qquad \textbf{6.2.1-8}$$

6.2.2 General Ceria Based Pressure-Swing Reactor

Now, we will use the axial nonstoichiometry model to explore the effect on a large sample geometry on gravimetric reduction rate. This sample geometry is a long cylindrical rod ceria, 5g in mass. The rod begins at equilibrium with pure steam at 1500C and is reduced by 10ppm oxygen in balance argon flowed at 100 sccm. The partition length for the model is chosen following the methodology discussed in section 6.4.1. For the following study, the length of the sample is varied while keeping all other parameters constant, including the face velocity and total mass. As the sample length (i.e. number of partitions) increases, it is equivalent to stretching out the sample to be another characteristic unit of length longer, with a correspondingly smaller cross sectional area.

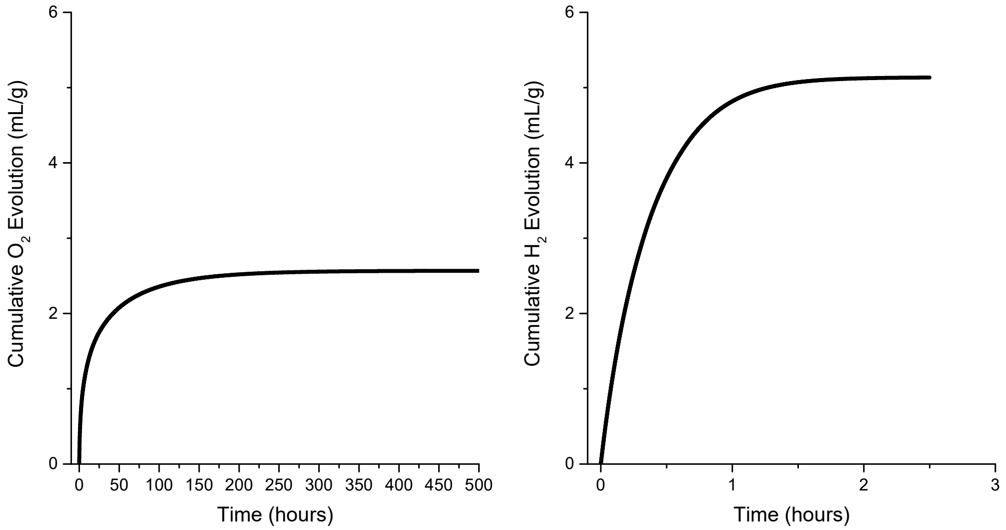

FIGURE 6.2-1 Theoretical oxygen (left) and hydrogen (right) fuel production for a 5g ceria rod, assuming uniform nonstoichiometry. The reduction occurs under 10ppm O_2 in a balance of argon and the oxidation occurs under pure steam. The reactor is operated isothermally at 1500°C.

First, the sample's behavior under the uniform nonstoichiometric condition is explored. The cumulative amount of oxygen and hydrogen produced over time are depicted in **Figure 6.2-1**. Due to the curvature of ceria's nonstoichiometric data (discussed in Chapter 4), there is a significant disparity between the time for the reduction and oxidation half cycles to reach equilibrium. The reduction step takes roughly 330 hours to complete, and the oxidation step only takes 2.5 hours. Thus, any decrease is oxidation time over the uniform nonstoichiometry case will be small relative to the decrease in reduction time. Therefore, in the remainder of this study only the reduction half cycle will be explored.

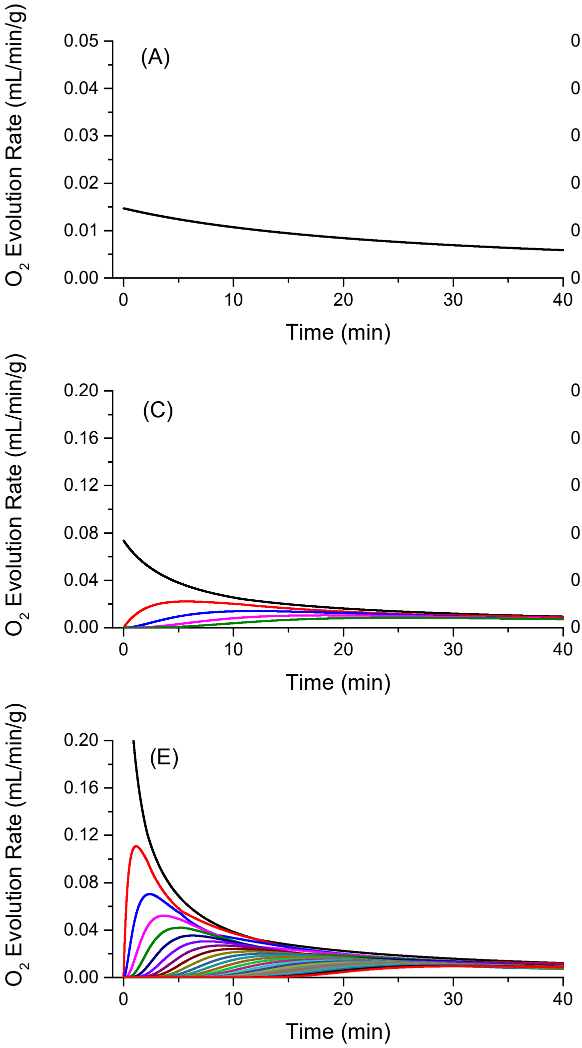

FIGURE 6.2-2 Oxygen evolution rates from a 5g long ceria rod modeled under 10ppm O_2 in balance argon after complete oxidation in steam at 1500ºC. The models use varying numbers of partitions for the finite element method (A, B, C, D, E corresponds to 1, 2, 5, 10, 25 partitions respectively). In each plot, the curves from top to bottom represent the partitions from upstream to downstream.

Five different sample lengths were modeled, corresponding to 1, 2, 5, 10, and 25 partitions. **Figure 6.2-2** displays the instantaneous oxygen evolution rate from each of the models during reduction. In order to better display the behavior of each model, the scale on plots (A) and (B) is only 25% of the others. In (E), the first partition's initial rate is 0.375 mL/min/g but has been scaled out of the plot to elucidate the behavior of the subsequent partitions. The initial rates of oxygen evolution scale with the number of partitions in each case, due to the fractional sample mass contained in each partition as discussed in the previous section. For the longer samples, the time at which the final partition begins to noticeably contribute to the oxidation of the gas plug is delayed. Up until this time, the gas coming out of the reactor is interacting with a fully oxidized sample, allowing for a sustained maximum evolution rate. After approximately 30 minutes of reduction all the partitions begin to converge to the same oxygen evolution rate, and, as a result, the average evolution rate of the partitions decreases.

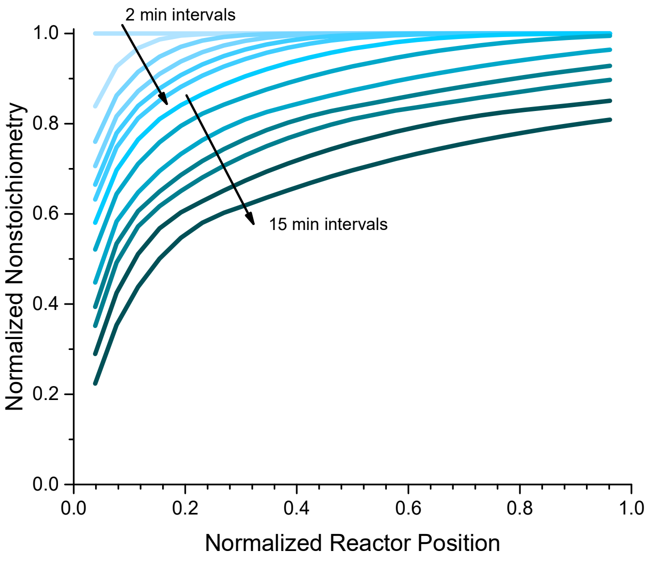

FIGURE 6.2-3 Nonstoichiometry profile along the ceria rod's length, normalized to the rod length, for the model using 25 partitions. The nonstoichiometry is normalized so that 1 corresponds to a fully oxidized state and 0 corresponds to the fully reduced state. The darker curves occur later in time; the first six curves are spaced two minutes apart, while the second half of the curves are spaced an average of 15 minutes apart.

The behavior of the early stages of the reduction behavior is explored in **Figure 6.2-3**. The curves grow darker as time passes in regular intervals. It takes about 20 minutes before the final partition feels the effects of the reducing gas. The leading partitions reduce very quickly during this 20 minute interval, and then their rate of nonstoichiometry change slows. This behavior is not observed in the later partitions, which experience uniform changes in nonstoichiometry at fixed time intervals. Once the final partition begins to undergo reduction the change in nonstoichiometry for each partition over a given time interval remains relatively constant, indicating that each partition is contributing equally to the reaction. At times beyond 120 minutes (not shown), the nonstoichiometry gradients become more uniform and the driving force for further reduction is diminished.

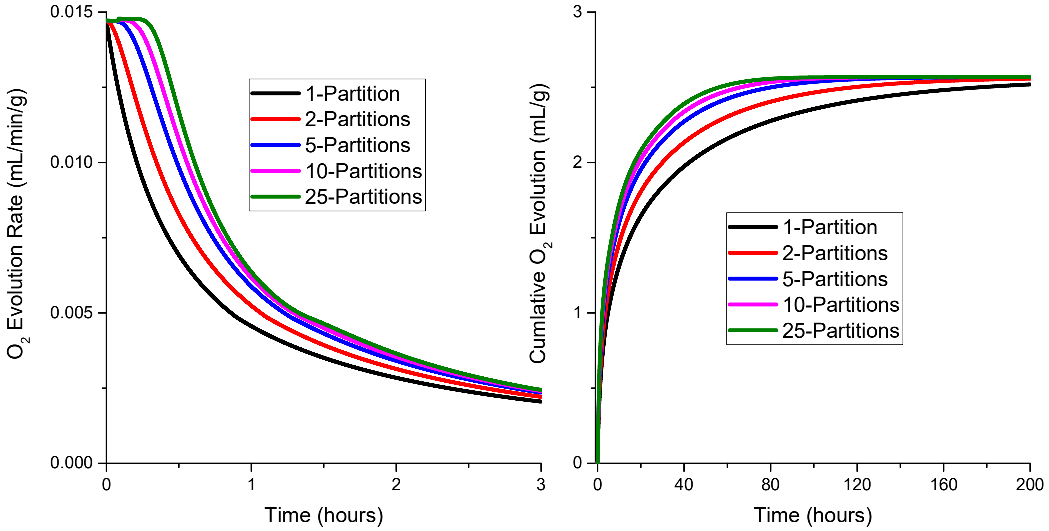

FIGURE 6.2-4 Weighted average oxygen evolution rate (left) and cumulative oxygen evolved (right) for a 5g ceria rod modeled under different numbers of partitions during reduction in 10ppm O_2 at 100 sccm after complete oxidation in steam at 1500ºC.

The instantaneous oxygen evolution rate and cumulative oxygen produced by the entire rod as a function of time were calculated and are displayed in **Figure 6.2-4**. Most notably, as the number of partitions increases a plateau region at the maximum evolution rate appears. This corresponds to the time until the final partition feels the effects of the reducing gas. This behavior was also experimentally observed in **Figure 2.4-6**. This also accounts for the vast majority of the rate increase compared to the uniform nonstoichiometry model. This effect is illustrated in the cumulative oxygen evolution plot, which shows the evolution profiles for models with more partitions relaxing to the equilibrium state at a faster rate. To quantify this improvement, the bar graph in **Figure 6.2-5** depicts a comparison of the amount of time for each model to reach 90% of the equilibrium value. In comparing the uniform nonstoichiometry case to the axial model using 25 partitions, a 61.9% decline in the amount of time it takes to reduce the sample to 90% of equilibrium.

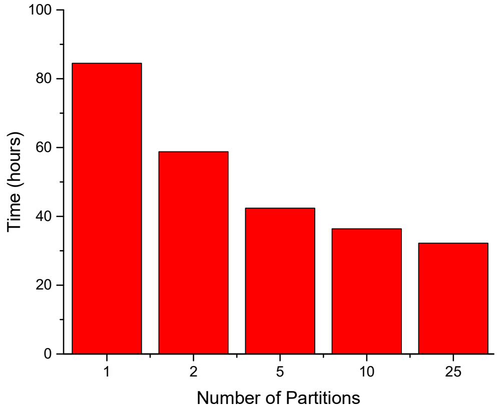

FIGURE 6.2-5 Comparison of the time needed for the rod to reach 90% of the equilibrium oxygen evolved for models with different numbers of partitions.

6.2.3 Demonstration with Ceria Fiberboard Samples

In order to demonstrate the effects of longer sample geometries on hydrogen production profiles, high-temperature thermochemical cycling experiments were performed (previously discussed in Chapter 2). A sample, 3 grams in mass and 12 cm in length was heated to 1500°C in an electric furnace, and the atmosphere was switched between 400 mL/min of reducing gas (10 ppm O_2 in Ar) and 400 mL/min of oxidizing gas (20% H_2O in Ar), with the material held under each atmosphere for 30 minutes, such that a full cycle was one hour in duration. During the evaluation, the material was exposed to more than 100 such cycles. In total, the material was held at 1500°C for ~ 4.5 days.

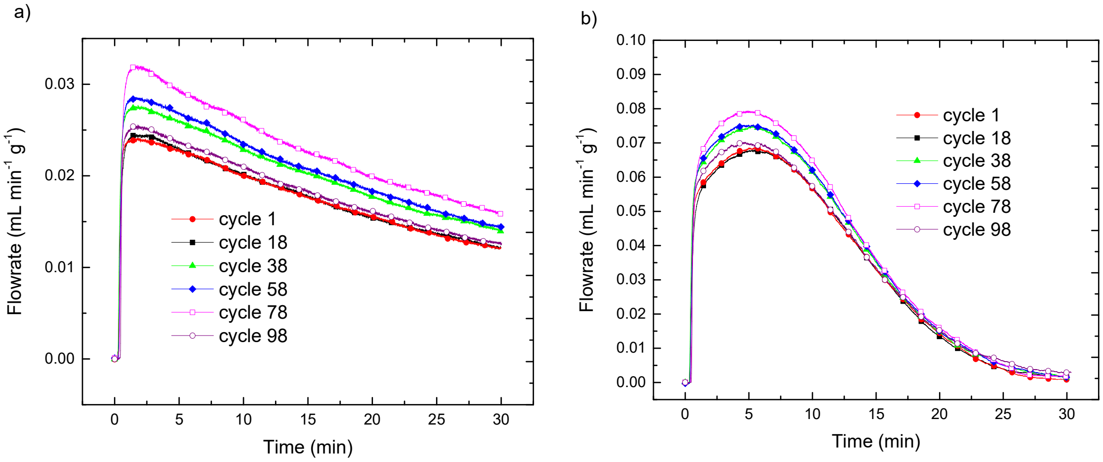

Figure 6.2-6 Isothermal cycling behavior of 3 g ceria fiberboard grog at 1500°C under 400 mL/min reducing gas (10 ppm O_2 in Ar) for 30 min and 400 mL/min of oxidizing gas (20% H_2O in Ar) for 30 min. (a) shows oxygen release profiles for six selected cycles of the 100-cycle test and (b) shows hydrogen production profiles for the same six selected cycles of the 100-cycle test.

The production curves of selected cycles from the 100-cycle evaluation are given in **Figure 2.4-6**. The shapes of the oxygen and hydrogen production profiles are generally reproduced for all of the cycles, although there is some variation in the magnitudes of the oxygen and hydrogen production curves, with the middle cycles (particularly cycles 58 and 78) peaking higher than the early or late cycles. The rounded profiles seen on the right image are indicative of a steady state production rate being achieved at shorter reaction times due to a nonstoichiometry gradient across the sample.

6.2.4 Isothermal Pressure-Swing Cycling of La$_{0.5}$Sr$_{0.5}$MnO$_3$

When the uniform nonstoichiometry model is applied to the LSM55 pressure-swing cycling data discussed in the previous chapter, we find good agreement with the oxidation half cycle, though the experimental oxygen evolution rate exceeds that predicted by the model (illustrated in **Figure 6.2-7**). To reconcile this discrepancy, an axial model was developed which relaxes the assumption that the entire sample is at a uniform nonstoichiometry. Finally, the axial nonstoichiometry model was compared to the uniform nonstoichiometry model in a theoretical pressure-swing reactor to demonstrate the enhancement during the reduction phase.

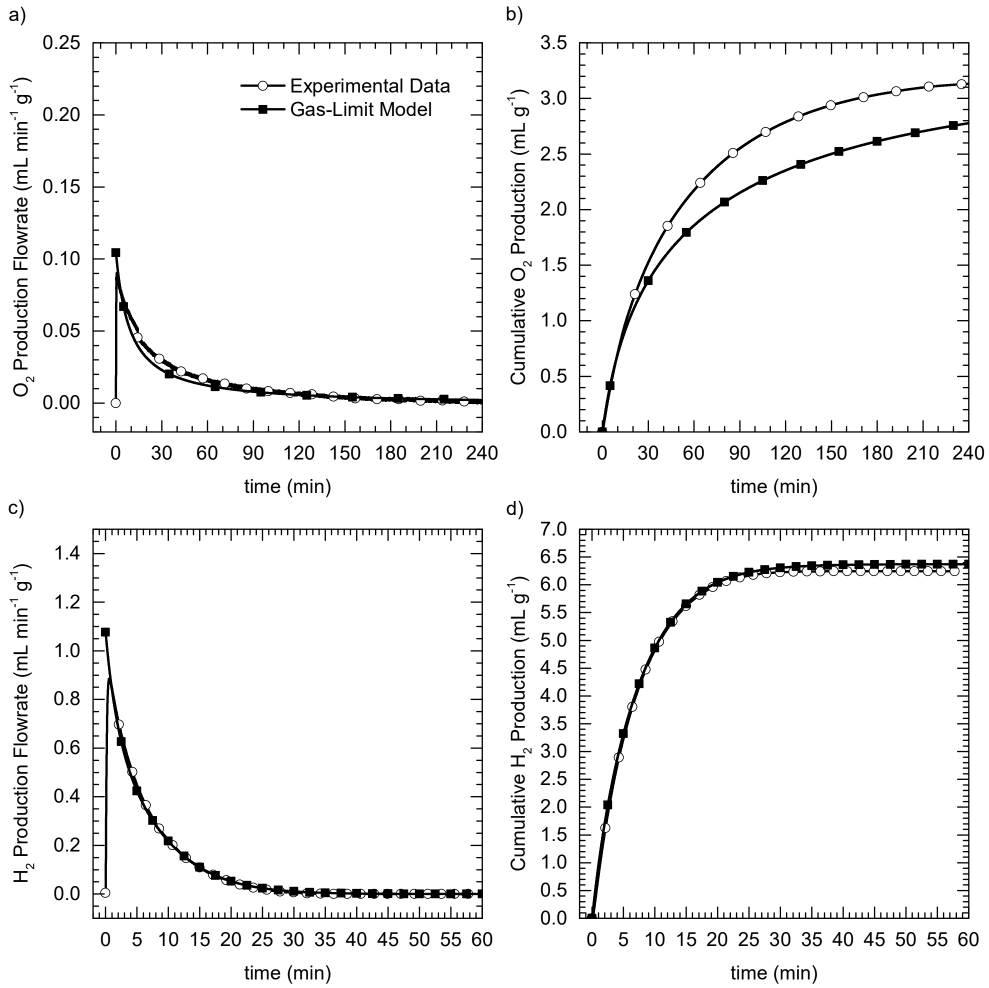

FIGURE 6.2-7 Comparison of an isothermal pressure-swing cycle at 1500 °C with (a-b) oxygen production during reduction of 0.65 g LSM55 by 300 sccm flow of 10 ppm O_2 in Ar, and (c-d) hydrogen production during oxidation by 300 sccm flow of 20% H_2O in Ar. Instantaneous flowrate profiles are given in (a) and (c), and cumulative production profiles are given in (b) and (d).

Here the axial nonstoichiometry model is employed to investigate this discrepancy. For these experimental conditions, the gas molecules will diffuse approximately 0.1 cm in the time it takes for the gas plug to move across the entire pellet, so the partition length should be roughly 0.2 centimeters. When loaded into the reactor, the sample was 1.2 cm in length, and thus five partitions will be used to model the experiment. First, to illustrate the features of the model, the sample is treated as only two partitions. **Figure 6.2-8** depicts the individual productivity of the first and second half of the pellet. Note that the raw hydrogen production rate for the uniform nonstoichiometry sample and the first partition in a partitioned sample differ only by a scalar. Since the first partition is only a fraction of the mass, once the productivity is mass normalized the initial rate for the first partition will always be a multiple of the uniform nonstoichiometry model. The second partition indicates the additional amount of oxygen the plug of gas is able to absorb from the portion of the sample that is more oxidized relative to the first partition. The first plug of gas to interact with the second partition has just been saturated with oxygen from the fully oxidized section of the sample. Consequently, the additional oxygen uptake is minimal, albeit nonzero.

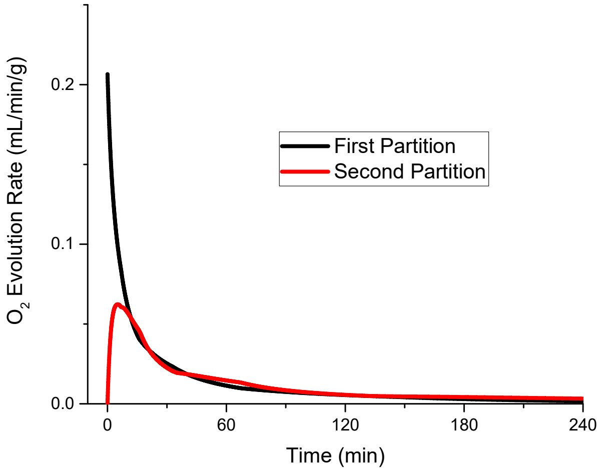

FIGURE 6.2-8 Theoretical reduction of a 0.65g LSM55 pellet held at 1500ºC in 10ppm oxygen for four hours after complete oxidation in 20% steam. The first partition indicates the productivity of the first half of the pellet, and the second partition indicates the productivity of the second half of the pellet.

As the sample approaches the fully reduced state, it is clear that the sample approaches a uniform nonstoichiometry and thus behaves comparably to a model without partitions. This similarity is demonstrated in **Figure 6.2-9**. After averaging the first and second partition, the increased O_2 evolution rate is barely noticeable in the normalized production rate plot, but is evident in the cumulative plot. After approximately 90 minutes of reduction, the difference in cumulative O_2 remains relatively constant between the two models. During the last half hour plotted, the uniform nonstoichiometry model evolves oxygen at a faster rate than the partitioned model. In the cumulative O_2 produced, this corresponds to a shallower slope of the partitioned sample. The rate for the partitioned model drops below the rate for the uniform model after about two hours because the nonstoichiometry of the partitions is larger than the uniform sample and the driving force for additional reduction is small. The theoretical equilibrium amount of oxygen evolved for these cycling conditions is 3.3 mL/g. Neither model has reached equilibrium after only four hours, but if the cumulative plots are extended out to twelve hours both models converge.

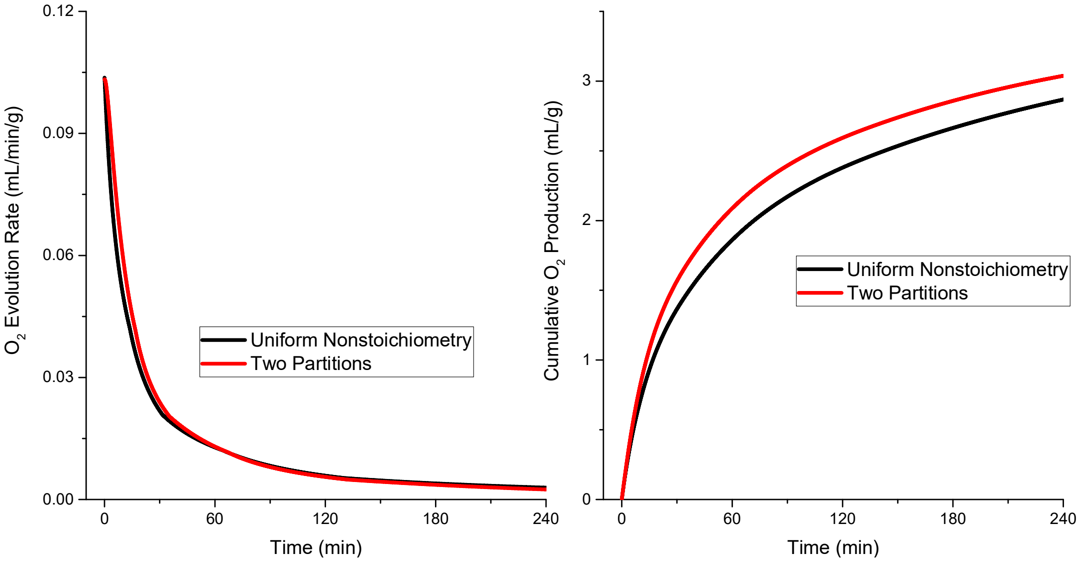

FIGURE 6.2-9 Theoretical reduction of a 0.65g LSM55 pellet held at 1500C in 10ppm oxygen after complete oxidation in 20% steam for four hours. The left and right plots compare the O_2 productivity and the cumulative O_2 production of the pellet when partitioned into halves versus when assumed to be at uniform nonstoichiometry.

Finally, the partitioned models are compared to the actual experimental data in **Figure 6.2-10**. Now the partitioned model is calculated with five partitions. With five partitions, the oxygen evolution of the model bounds the experimental oxygen production, providing a resolution to the discrepancy discussed earlier. It is important to note that for these models, a reduction gas of 11ppm was used instead of 10ppm. This accounts for the natural leaking of oxygen into the system from diffusion through piping and fittings. This adjustment along with other experimental imperfections explains most of the remaining disagreement between the five partition model and the experimental data.

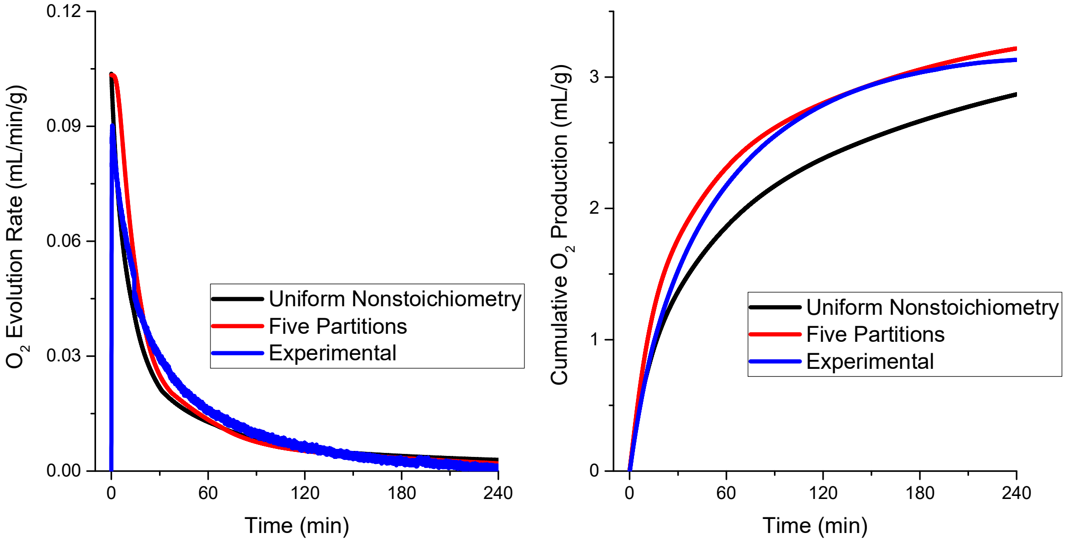

FIGURE 6.2-10 Theoretical and experimental reduction of a 0.65g LSM55 pellet held at 1500C in 10ppm oxygen after complete oxidation in 20% steam. The left plot indicates the normalized O_2 evolution rate and the right plot indicates the normalized cumulative O_2 production.

Additionally, after roughly 2.5 hours of reduction it appears that the experimental sample catches up to the total evolution of the five partition model. This should not be physically possible, but the suspected source of this error is uncertainty in the thermodynamic data used in calculating the model discussed more in detail in the previous chapter.

6.2.5 Summary and Implications

In this chapter, the effects of infinitely fast material kinetics on the fuel production rate were explored. In this paradigm, the oxygen evolution and hydrogen production rates are dictated by the thermodynamics of the material and the gas phase. The thermokinetic model was derived, demonstrating the governing equations for this behavior with and without the assumption of uniform nonstoichiometry of the oxide. When allowing for an axial nonstoichiometric gradient, the reduction cycling time was reduced significantly in a long rod sample. The axial variation model demonstrated a peak oxygen evolution rate for a finite period of time due to the varying rates at which portions of the oxide are reduced. The model with axial nonstoichiometry variation also fit the isothermal pressure swing cycling data more accurately than the uniform nonstoichiometry model.

In a previous work on the thermokinetic limit, an optimization was performed to determine the optimal cycling conditions for an isothermal pressure swing cycle on ceria [16]. The cycling conditions, which optimized the peak rate, were to have cycles of infinitesimal time, which would maintain a maximum driving force between the oxide and the gas. This provides great insight, but is largely impractical. The thermokinetic model with axial variation in nonstoichiometry indicates that this maximum rate is achievable for finite cycling times. The major cost introduced to the long rod reactor is the need for a longer heating zone. A careful cost analysis of the energy requirements for such a reactor would be required to determine if the expedited reduction rate offsets the increased power requirement.

Chapter 7 Conclusions and Future Work

7.1 Conclusions

Various nonstoichiometric oxides were evaluated for thermochemical properties, with particular emphasis on morphology, thermodynamics, and kinetics. A benchtop thermochemical reactor system was designed and in aid of realizing more efficient solar driven thermochemical reactors, it was shown that:

1) Ceria exhibits substantial thermochemical expansion when exposed to reducing conditions under high temperature. Doping neat ceria with zirconia not only enhances its reducibility, but also stabilizes the chemical expansion
2) Zr-doped ceria compounds stabilize inverse opals structures up through 1000ºC. Larger pore diameter inverse opal are more stable and have better gas diffusion than smaller pore inverse opals. Zr-doped ceria inverse opals have sufficiently high surface area to exhibit thermochemical cycling limited by thermodynamics rather than material kinetics even at low temperatures.
3) Ceria fiberboard structures have narrow pore size distributions which allow for sufficient gas phase access to all surfaces. For sufficient low flowrate the surface area is high enough such that high temperature cycling is limited by thermodynamics.
4) For long samples, an axial nonstoichiometry gradient will form during reduction. This allows the gas plug to absorb more oxygen than if the sample were held at uniform nonstoichiometry, resulting in improved cycling efficiency.

In pursuit of discovering new materials, which will outperform ceria in either thermochemical cycling capacity or kinetics, it was found that:

1) Praseodymium and terbium doped ceria reduce more easily than neat ceria and have a larger capacity for fuel production at comparable temperatures and oxygen partial pressures. Pr- and Tb-doped ceria have thermodynamic functions which exhibit two distinct regions of redox reactions. Pr-doped ceria's (and consequently Tb-doped ceria's entropy is too low to allow for Pr (or Tb) to participate in traditional thermochemical cycles.
2) Samarium doped ceria has a reduced capacity for fuel production due to intrinsic vacancies formed within the sample upon doping. Under high-temperature, isothermal, pressure-swing cycling the faster ionic transport in Sm-doped ceria does not compensate for reduced fuel production per cycle.
3) Lanthanum strontium manganite perovskites are limited by poor thermodynamics even at low temperatures. For certain finite cycling times and conditions, the large nonstoichiometry change of perovskites over ceria under isothermal pressure-swing cycling, result in more favorable fuel production rates.
4) The materials that are likely to be more efficient than ceria at thermochemical cycling under the thermokinetic limit are those with linear nonstoichiometry isotherms. These are characterized by materials, which undergo oxygen excess rather than oxygen deficiency.

7.2 Future Work

7.2.1 Alternate Thermodynamic Characterization Technique

Currently, the only method used to determine a material’s reduction reaction enthalpy and entropy is thermogravimetric analysis. This process produces sparse plots of the nonstoichiometry at a given temperature and oxygen partial pressure. The experiments can be lengthy due to the long times required by the material to reach equilibrium. In principle, if cycling behavior occurs under the thermokinetic limit, then the nonstoichiometric profile and the enthalpy and entropy of reduction as a function of nonstoichiometry can be determined from the gas evolution rate data. Here, an appropriate experimental procedure is outlined.

7.2.1.1 Theory

From thermochemical cycling experiments, oxygen evolution and hydrogen production rates are measured as a function of time. By integrating the volumetric gas evolution profiles, the cumulative amount of gas produced as a function of time is obtained. If the material began the cycle from a known reference state, then the total amount of oxygen evolved (or hydrogen produced) during each time step can be used to calculate the nonstoichiometry of the material as a function of time via the equation below.

$$\boldsymbol{\delta(t) = \delta_{ref}^{ox}(t_0) + \frac{2M_{CeO_2}}{V_M}\int_{t_0}^{t} \dot{v}_{O_2}(t)dt} \qquad \textbf{7.2.1-1}$$

where δ_{ref}^{ox} is the equilibrium nonstoichiometry under the oxidizing conditions and t_0 refers to the reduction half cycle's start time. An analogous equation can be used to determine the nonstoichiometry as a function of time for the oxidation half cycle.

$$\boldsymbol{\delta(t) = \delta_{ref}^{red}(t_0) - \frac{M_{Ce\;\;2}}{V_M}\int_{t_0}^{t} \dot{v}_{H_2}(t)dt} \tag{7.2.1-2}$$

where δ_{ref}^{red} is the equilibrium nonstoichiometry under the reducing conditions and t_0 refers to the oxidation half cycle's start time. Next, the oxide's equivalent oxygen partial pressure as a function of time must be determined from the gas production data. The oxide's nonstoichiometric rate of change during the reduction half cycle can be directly determined from the volumetric oxygen production rate data.

$$\boldsymbol{\frac{d\delta_{red}}{dt}(t) = \frac{2M_{Ce\;\;2}}{V_M}\dot{v}_{O_2}(t)} \tag{7.2.1-3}$$

For the portion of the oxygen evolution profile described by the thermokinetic limit, knowing the nonstoichiometric rate of change allows the material's equivalent oxygen partial pressure as a function of time to be determined. By rearranging, **Equation 6.2.1-7**, the governing equation for the reduction reaction, the following relation is obtained.

$$\boldsymbol{P_{O_2}(t) = \frac{n_{Ce\;\;2}P_{tot}\frac{d\delta_{red}}{dt}(t) + 2F_{red}P_{O_2in}}{n_{Ce\;\;2}\frac{d\delta_{red}}{dt}(t) + 2F_{red}}} \tag{7.2.1-4}$$

An analogous set of equations can be derived to allow for the determination of the material's equivalent oxygen partial pressure from the oxidation half reaction.

$$\boldsymbol{\frac{d\delta_{ox}}{dt}(t) = -\frac{M_{Ce\;\;2}}{V_M}\dot{v}_{H_2}(t)} \tag{7.2.1-5}$$

$$\boldsymbol{\frac{d\delta_{ox}}{dt}(t) = \frac{F_{ox}}{n_{CeO_2}}\left(\frac{2P_{O_2}(t)}{\left(P_{tot}-P_{O_2}(t)\right)} - \frac{\chi_{H_2O}K_{H_2O,T_0}}{\left(\sqrt{P_{O_2}(t)}+K_{H_2O,T_0}\right)}\right)} \tag{7.2.1-6}$$

where $P_{O_2}(t)$ must be solved for numerically as an analytical expression is untenable.

Now that $P_{O_2}(t)$ and $\delta(t)$ are known, the pairs at the same time become the nonstoichiometric data at the temperature for which the cycle is conducted. The free energy of reduction can be determined from the equilibrium expression for the reduction reaction.

$$\frac{1}{2}\boldsymbol{RT ln}\left(\boldsymbol{P_{O_2}(\delta,T)}\right) = -\boldsymbol{\Delta G_{red}(\delta)} \qquad \textbf{7.2.1-7}$$

Note that here the free energy of reduction is expressed per oxygen atom. In order to determine the enthalpy and entropy of the reduction reaction explicitly, several cycles at different temperatures with overlapping nonstoichiometry values are necessary. The entropy and enthalpy could then be extracted by generating an Arrhenius plot of ΔG_{red} versus inverse temperature at a given nonstoichiometry.

7.2.1.2 Experimental

To demonstrate a proof of concept for this methodology, this analysis was performed on a previously published isothermal, pressure-swing cycle [17]. **Figure 7.2-1** illustrates the comparison between the free energy of reduction for neat ceria at 1500ºC as calculated from reference nonstoichiometry data [40] and the free energy of reduction for neat ceria at 1500ºC as calculated from a thermochemical, isothermal, pressure-swing, cycling experiment. The experimental data shows moderate agreement with the nonstoichiometry data, but at this stage, results are too preliminary to make generalization about why the matching is better or worse.

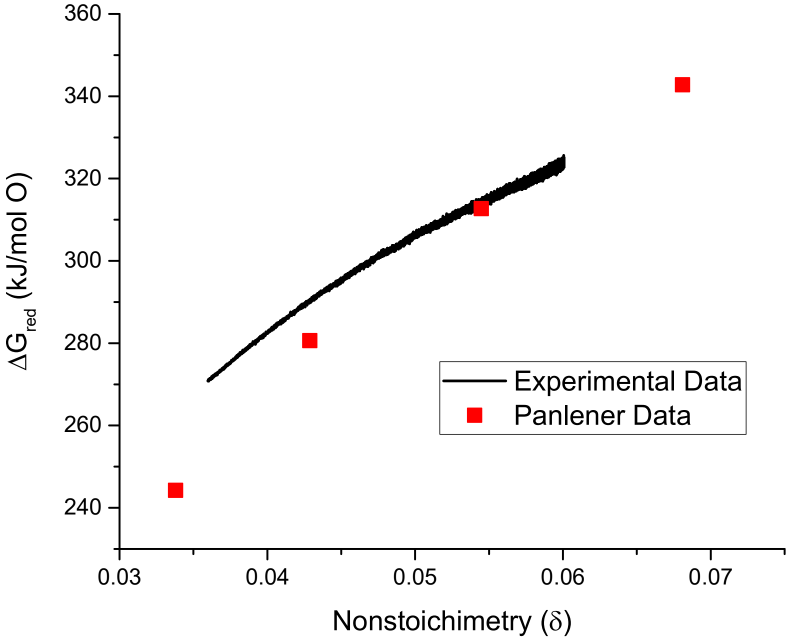

FIGURE 7.2-1 Comparison between the free energy of reduction as calculated from Panlener's neat ceria nonstoichiometric data and the free energy of reduction as calculated from thermochemical, isothermal, pressure-swing cycling experiments.

In order to fully determine the enthalpy and entropy of reduction the following experiments should be performed. One half gram of neat ceria should be isothermally, chemically cycled at multiple temperatures between 1100ºC and 1500ºC with flow rates at or below 200sccm for both the oxidizing and reducing streams. This will ensure that all operation occurs within the regime of the thermokinetic limit. The oxidizing gas should be pure argon passed through a humidifier held at 60ºC (P_{H_2O} of 0.19660 atm). The reducing gas should be 3% H_2 in argon passed through a humidifier held at 20ºC (P_{H_2O} of 0.02308 atm). These two gas compositions will ensure that the ceria undergoes a sufficiently wide range of overlapping nonstoichiometries between each experiment. This is the widest range possible due to experimental and safety limitation and should be used for other materials, unless there are known phase changes under these conditions. In between the reduction and oxidation half cycles, a 30 second 1500sccm pure argon purge should be conducted to remove hydrogen from the reactor. **Table 7.2.1-1** outlines the nonstoichiometry ranges the cycles will reach at each temperature, based on the exact theoretical values calculated from the Panlener data.

TABLE 7.2.1-1 Relevant equilibrium nonstoichiometric conditions in neat ceria for isothermal, pressure-swing cycling.

Temperature (^{0}C)	Reducing P_{O_2} (atm)	Oxidizing P_{O_2} (atm)	Reducing Nonstoichiometry	Oxidizing Nonstoichiometry
1100	$4.974*10^{-14}$	$9.329*10^{-6}$	0.1153	0.001399
1200	$9.712*10^{-13}$	$2.512*10^{-5}$	0.1464	0.003712
1300	$1.304*10^{-11}$	$5.969*10^{-5}$	0.1689	0.008583
1400	$1.287*10^{-10}$	$1.280*10^{-4}$	0.1874	0.01694
1500	$9.833*10^{-10}$	$2.518*10^{-4}$	0.2057	0.03382

This experimental method will allow for the determination of the reduction reaction's entropy and enthalpy over a nonstoichiometry range of about 0.034 to 0.12. This range can be increased significantly by reducing in a more aggressive environment at lower temperatures, however, this would pass the lower combustible limit for hydrogen and pose significant safety concerns. Lower values of nonstoichiometry can be accessed by oxidizing in higher concentrations of steam at higher temperatures, but water management becomes more difficult as the gas lines will need to be held at a higher temperature to prevent premature condensation. Alternatively, if the need for five data points when fitting the Arrhenius plot is relaxed to four data points, then the range increases to nonstoichiometric values of 0.017 to 0.15. Furthermore, more temperature steps could be explored within this range to provide better accuracy.

It is important to note that, in this cycling paradigm, the oxidation half cycle can be modeled with the current thermokinetic model to determine the nonstoichiometry thermodynamics, but a new reduction model is necessary to properly account for the introduction of hydrogen and water to the reducing gas. Additionally, an oxygen sensor should be downstream of the reactor for accurate determination of equilibrium oxygen partial pressure.

Chapter 8 References

1. Diver, R.B., et al., *Solar Thermochemical Water-Splitting Ferrite-Cycle Heat Engines.* Journal of Solar Energy Engineering, 2008. **130**(4): p. 041001.
2. Wegner, K., et al., *In situ formation and hydrolysis of Zn nanoparticles for H2H2 production by the 2-step ZnO/Zn water-splitting thermochemical cycle.* International Journal of Hydrogen Energy, 2006. **31**(1): p. 55-61.
3. Marrocchelli, D., et al., *Understanding Chemical Expansion in Non-Stoichiometric Oxides: Ceria and Zirconia Case Studies.* Advanced Functional Materials, 2012. **22**(9): p. 1958-1965.
4. Chueh, W.C., et al., *High-Flux Solar-Driven Thermochemical Dissociation of CO2 and H2O Using Nonstoichiometric Ceria.* Science, 2010. **330**(6012): p. 1797-1801.
5. Roeb, M., et al., *Solar Hydrogen Production by a Two-Step Cycle Based on Mixed Iron Oxides.* Journal of Solar Energy Engineering, 2006. **128**(2): p. 125.
6. Ji, H.-I., et al., *Gas-phase vs. material-kinetic limits on the redox response of nonstoichiometric oxides.* Physical Chemistry Chemical Physics, 2017. **19**(10): p. 7420-7430.
7. Stokes, D.J., *Principles of SEM*, in *Principles and Practice of Variable Pressure/Environmental Scanning Electron Microscopy (VP-ESEM)*. 2008, John Wiley & Sons, Ltd. p. 17-62.
8. Müller, R., P. Haeberling, and R.D. Palumbo, *Further advances toward the development of a direct heating solar thermal chemical reactor for the thermal dissociation of ZnO(s).* Solar Energy, 2006. **80**(5): p. 500-511.
9. Roeb, M., et al., *Test operation of a 100kW pilot plant for solar hydrogen production from water on a solar tower.* Solar Energy, 2011. **85**(4): p. 634-644.
10. Lewis, N.S. and D.G. Nocera, *Powering the planet: chemical challenges in solar energy utilization.* Proc Natl Acad Sci U S A, 2006. **103**(43): p. 15729-35.

11. Xiao, L., S.-Y. Wu, and Y.-R. Li, *Advances in solar hydrogen production via two-step water-splitting thermochemical cycles based on metal redox reactions.* Renewable Energy, 2012. **41**: p. 1-12.
12. Kodama, T., Y. Nakamuro, and T. Mizuno, *A Two-Step Thermochemical Water Splitting by Iron-Oxide on Stabilized Zirconia.* Journal of Solar Energy Engineering, 2006. **128**(1): p. 3.
13. Graf, D., et al., *Economic comparison of solar hydrogen generation by means of thermochemical cycles and electrolysis.* International Journal of Hydrogen Energy, 2008. **33**(17): p. 4511-4519.
14. Hao, Y., C.-K. Yang, and S.M. Haile, *High-temperature isothermal chemical cycling for solar-driven fuel production.* Physical Chemistry Chemical Physics, 2013. **15**(40): p. 17084-17092.
15. Ermanoski, I., J.E. Miller, and M.D. Allendorf, *Efficiency maximization in solar-thermochemical fuel production: challenging the concept of isothermal water splitting.* Physical Chemistry Chemical Physics, 2014. **16**(18): p. 8418-8427.
16. Davenport, T.C., et al., *Maximizing fuel production rates in isothermal solar thermochemical fuel production.* Applied Energy, 2016. **183**: p. 1098-1111.
17. Davenport, T.C., et al., *Implications of Exceptional Material Kinetics on Thermochemical Fuel Production Rates.* Energy Technology, 2016. **4**(6): p. 764-770.
18. Singhal, S.C. *Application of ionic and electronic conducting ceramics in solid oxide fuel cells*. 1997. United States.
19. Steele*, B.C.H., *Materials for IT-SOFC stacks: 35 years R&D: the inevitability of gradualness?* Solid State Ionics, 2000. **134**(1–2): p. 3-20.
20. Yamamoto, O., *Solid oxide fuel cells: fundamental aspects and prospects.* Electrochimica Acta, 2000. **45**(15–16): p. 2423-2435.
21. Steele, B.C.H., *Ceramic ion conducting membranes.* Current Opinion in Solid State and Materials Science, 1996. **1**(5): p. 684-691.

22. Anderson, H.U., *Review of p-type doped perovskite materials for SOFC and other applications.* Solid State Ionics, 1992. **52**(1): p. 33-41.
23. Dyer, P.N., et al., *Mixed conducting membranes for syngas production*. 2002, Google Patents.
24. Atkinson, A. and T.M.G.M. Ramos, *Chemically-induced stresses in ceramic oxygen ion-conducting membranes.* Solid State Ionics, 2000. **129**(1–4): p. 259-269.
25. Hao, Y., C.-K. Yang, and S.M. Haile, *Ceria–Zirconia Solid Solutions (Ce1–xZrxO2−δ, x ≤ 0.2) for Solar Thermochemical Water Splitting: A Thermodynamic Study.* Chemistry of Materials, 2014. **26**(20): p. 6073-6082.
26. Chen, Yu, and S.B. Adler, *Thermal and Chemical Expansion of Sr-Doped Lanthanum Cobalt Oxide (La1-xSrxCoO3-δ).* Chemistry of Materials, 2005. **17**(17): p. 4537-4546.
27. Mogensen, G. and M. Mogensen, *Reduction reactions in doped ceria ceramics studied by dilatometry.* Thermochimica Acta, 1993. **214**(1): p. 47-50.
28. Tietz, F., *Thermal expansion of SOFC materials.* Ionics, 1999. **5**(1-2): p. 129-139.
29. Hong, S.J. and A.V. Virkar, *Lattice Parameters and Densities of Rare-Earth Oxide Doped Ceria Electrolytes.* Journal of the American Ceramic Society, 1995. **78**(2): p. 433-439.
30. Rudisill, S.G., Z. Wang, and A. Stein, *Maintaining the Structure of Templated Porous Materials for Reactive and High-Temperature Applications.* Langmuir, 2012. **28**(19): p. 7310-7324.
31. Ergang, N.S., et al., *Effect of a Macropore Structure on Cycling Rates of LiCoO[sub 2].* Journal of The Electrochemical Society, 2005. **152**(10): p. A1989.
32. Stein, A., F. Li, and N.R. Denny, *Morphological Control in Colloidal Crystal Templating of Inverse Opals, Hierarchical Structures, and Shaped Particles.* Chemistry of Materials, 2008. **20**(3): p. 649-666.

33. Venstrom, L.J., et al., *The Effects of Morphology on the Oxidation of Ceria by Water and Carbon Dioxide.* Journal of Solar Energy Engineering, 2011. **134**(1): p. 011005-011005-8.
34. Rudisill, S.G., et al., *Enhanced Oxidation Kinetics in Thermochemical Cycling of CeO2 through Templated Porosity.* The Journal of Physical Chemistry C, 2013. **117**(4): p. 1692-1700.
35. Petkovich, N.D., et al., *Control of Heterogeneity in Nanostructured Ce1–xZrxO2 Binary Oxides for Enhanced Thermal Stability and Water Splitting Activity.* The Journal of Physical Chemistry C, 2011. **115**(43): p. 21022-21033.
36. Yang, L., et al., *Highly Ordered 3D Graphene-Based Polymer Composite Materials Fabricated by "Particle-Constructing" Method and Their Outstanding Conductivity.* Macromolecules, 2014. **47**(5): p. 1749-1756.
37. Scherrer, P., *Bestimmung der Grosse und der inneren Struktur von Kolloidteilchen mittels Rontgenstrahlen.* Gottinger Nachrichten Gsell., 1918. **2**.
38. Davis, M.D.a.R., *Fundamentals of Chemical Reaction Engineering*. 4th ed. 2003, New York, NY: McGraw Hill.
39. Weast, R., *Handbook of Chemistry and Physics*. 53rd ed. 1972, Cleveland, OH: Chemical Rubber Co.
40. Panlener, R.J., R.N. Blumenthal, and J.E. Garnier, *A thermodynamic study of nonstoichiometric cerium dioxide.* Journal of Physics and Chemistry of Solids, 1975. **36**(11): p. 1213-1222.
41. Meng, Q.-L., et al., *Solar thermochemical process for hydrogen production via two-step water splitting cycle based on Ce1−xPrxO2−δ redox reaction.* Thermochimica Acta, 2012. **532**: p. 134-138.
42. Eguchi, K., et al., *Electrical properties of ceria-based oxides and their application to solid oxide fuel cells.* Solid State Ionics, 1992. **52**(1–3): p. 165-172.
43. Gopal, C.B. and S.M. Haile, *An electrical conductivity relaxation study of oxygen transport in samarium doped ceria.* Journal of Materials Chemistry A, 2014. **2**(7): p. 2405-2417.

44. Leonidov, I.A., et al., *High-temperature electrical conductivity of Sr0.7La0.3FeO3−δ.* Solid State Ionics, 2001. **144**(3–4): p. 361-369.
45. Ovenstone, J., J.S. White, and S.T. Misture, *Phase transitions and phase decomposition of La1−xSrxCoO3−δ in low oxygen partial pressures.* Journal of Power Sources, 2008. **181**(1): p. 56-61.
46. Chmaissem, O., et al., *Structural and magnetic phase diagrams of ${\mathrm{La}}_{1\ensuremath{-}x}{\mathrm{Sr}}_{x}{\mathrm{MnO}}_{3}$ and ${\mathrm{Pr}}_{1\ensuremath{-}y}{\mathrm{Sr}}_{y}{\mathrm{MnO}}_{3}$.* Physical Review B, 2003. **67**(9): p. 094431.
47. Mitchell, J.F., et al., *Structural phase diagram of ${\mathrm{La}}_{1\ensuremath{-}x}{\mathrm{Sr}}_{x}\mathrm{Mn}{\mathrm{O}}_{3+\ensuremath{\delta}}$: Relationship to magnetic and transport properties.* Physical Review B, 1996. **54**(9): p. 6172-6183.
48. Mizusaki, J., et al., *Oxygen nonstoichiometry and defect equilibrium in the perovskite-type oxides La1−xSrxMnO3+d.* Solid State Ionics, 2000. **129**(1–4): p. 163-177.
49. Mizusaki, J., et al., *Electronic conductivity, Seebeck coefficient, defect and electronic structure of nonstoichiometric La1−xSrxMnO3.* Solid State Ionics, 2000. **132**(3–4): p. 167-180.
50. Kuo, J.H., H.U. Anderson, and D.M. Sparlin, *Oxidation-reduction behavior of undoped and Sr-doped LaMnO3 nonstoichiometry and defect structure.* Journal of Solid State Chemistry, 1989. **83**(1): p. 52-60.
51. Andrieux, M. and C. Picard, *Nonstoichiometry and phase stability of La0.8Sr0.2MnO3±δ at 1273 K.* Journal of Materials Science Letters, 2000. **19**(8): p. 695-697.

52. Evdou, A., L. Nalbandian, and V.T. Zaspalis, *Perovskite membrane reactor for continuous and isothermal redox hydrogen production from the dissociation of water.* Journal of Membrane Science, 2008. **325**(2): p. 704-711.

53. Evdou, A., V. Zaspalis, and L. Nalbandian, *La(1−x)SrxMnO3−δ perovskites as redox materials for the production of high purity hydrogen.* International Journal of Hydrogen Energy, 2008. **33**(20): p. 5554-5562.

54. Nalbandian, L., A. Evdou, and V. Zaspalis, *La1−xSrxMO3 (M = Mn, Fe) perovskites as materials for thermochemical hydrogen production in conventional and membrane reactors.* International Journal of Hydrogen Energy, 2009. **34**(17): p. 7162-7172.

55. Yang, C.-K., et al., *Thermodynamic and kinetic assessments of strontium-doped lanthanum manganite perovskites for two-step thermochemical water splitting.* Journal of Materials Chemistry A, 2014. **2**(33): p. 13612-13623.

56. Scheffe, J.R., D. Weibel, and A. Steinfeld, *Lanthanum–Strontium–Manganese Perovskites as Redox Materials for Solar Thermochemical Splitting of H2O and CO2.* Energy & Fuels, 2013. **27**(8): p. 4250-4257.

57. McDaniel, A.H., et al., *Sr- and Mn-doped LaAlO3-[small delta] for solar thermochemical H2 and CO production.* Energy & Environmental Science, 2013. **6**(8): p. 2424-2428.

58. Bork, A.H., E. Povoden-Karadeniz, and J.L.M. Rupp, *Modeling Thermochemical Solar-to-Fuel Conversion: CALPHAD for Thermodynamic Assessment Studies of Perovskites, Exemplified for (La,Sr)MnO3.* Advanced Energy Materials, 2017. **7**(1): p. 1601086-n/a.

59. Sutherland, W., *LII. The viscosity of gases and molecular force.* Philosophical Magazine Series 5, 1893. **36**(223): p. 507-531.

60. J.O. Hirschfelder, R.B.B., E.L. Spotz, *The transport properties of gases and gaseous mixtures II.* Chem. Rev., 1949. **44**: p. 205-231.

61. J.R. Welty, C.E.W., and R.E. Wilson, *Fundamentals of Momentum, Heat, and Mass Transfer*. 3rd ed. 1984, New York: John Wiley & Sons.

62. Fernandes, J.D.G., et al., *Low-temperature synthesis of single-phase crystalline LaNiO3 perovskite via Pechini method.* Materials Letters, 2002. **53**(1–2): p. 122-125.

63. Colombo, P., *Conventional and novel processing methods for cellular ceramics.* Philosophical Transactions of the Royal Society A: Mathematical, Physical and Engineering Sciences, 2006. **364**(1838): p. 109.

64. Studart, A.R., et al., *Processing Routes to Macroporous Ceramics: A Review.* Journal of the American Ceramic Society, 2006. **89**(6): p. 1771-1789.

65. Furler, P., et al., *Thermochemical CO2 splitting via redox cycling of ceria reticulated foam structures with dual-scale porosities.* Physical Chemistry Chemical Physics, 2014. **16**(22): p. 10503-10511.

66. Nelson, J.B. and D.P. Riley, *An experimental investigation of extrapolation methods in the derivation of accurate unit-cell dimensions of crystals.* Proceedings of the Physical Society, 1945. **57**(3): p. 160.

67. Webb, P.A., *An Introduction to the Physical Characterization of Materials by Mercury Intrusion Porosimetry with Emphasis on Reduction and Presentation of Experimental Data*. 2001, Micromeritics Instrument Corp.: Norcross, GA.

68. de Hoffmann, E. and V. Stroobant, *Mass Spectrometry: Principles and Applications*. 2007: Wiley-Interscience.

Chapter 9 Appendix

9.1 Synthesis Techniques

In order to generate the materials discussed in this work, two synthesis techniques are used. The first is a Pechini or Sol-Gel technique. This is a wet chemical process and is used to make doped ceria compounds. The second is a solid-state technique which was used to make the perovskite material, lanthanum strontium manganite oxide. For each material to be useful in thermochemical cycling, a porous pellet is created from the synthesized powders.

9.1.1 Sol-Gel Technique

Results presented in Chapter 4.

The Sol-Gel technique used in this work is a type of wet chemical synthesis technique known as a Pechini method [62]. In this method, the relevant metals' nitrates are mixed, in stoichiometric quantities, into an aqueous solution containing the following: ethylenediaminetetraacetic acid as a chelating agent, citric acid as a linking agent, and ammonium hydroxide as a pH buffer. Stirring the mixture ensures a homogeneous distribution of ions at the atomic level. Controlled evaporation is performed on this mixture, yielding a homogenous gel. This gel is subsequently heated in two separate steps to 170ºC and 350ºC to burn off organics and evaporate any remaining moisture, leaving behind a powder of the desired oxide composition. This powder is then annealed at 950ºC to crystallize the product. At this point, samples are characterized by X-ray diffraction, which confirms the crystalline structure and desired cubic phase. Lastly, the powder is compressed in an isopropyl alcohol suspension and sintered at 1500ºC to yield the porous pellets. Scanning electron microscopy is used to characterize the morphology of the sample, while energy dispersive spectroscopy is used to confirm chemical uniformity of the sample.

9.1.2 Solid-State Synthesis

Results presented in Chapter 5.

The solid-state reaction method is more direct and lower in cost than the wet chemical techniques mentioned in the previous section. However, materials made from the solid-state reaction are prone to inhomogeneity and contamination during mixing. To minimize these risks, sufficient mixing times are used to promote uniform composition, and mixing materials are of greater hardness than the oxide materials so that no contamination will occur. Purity and composition are confirmed with powder x-ray diffraction and energy dispersive spectroscopy, respectively. This method was used to prepare compositions of lanthanum strontium manganite oxide ($La_{1-x}Sr_xMnO_3$, where x = 0.2, 0.3, 0.4, and 0.5). Stoichiometric quantities of La_2O_3 (Alfa Aesar, REacton®, 99.99%), $SrCO_3$ (Sigma-Aldrich $99.9%), and $MnCO_3$ (Sigma-Aldrich $99.9%) were combined and attrition-milled in isopropanol for six hours at 500 rpm. After drying, the powder was calcined at 1000 °C for three hours under air. A porous monolith was fabricated from this powder by mixing the latter with isopropanol (3 ml of liquid per gram of powder) to obtain a thick paste. This paste was then placed (without application of pressure) into an alumina cylindrical mold with an inner diameter of 10 mm and fired at 1500 °C for six hours under air. The results were porous pellets with a mass of 0.325 g (65-70% porous), two of which were used in the reactor. **Figure 9.1-1** illustrates the process by which the LSM pellets were made.

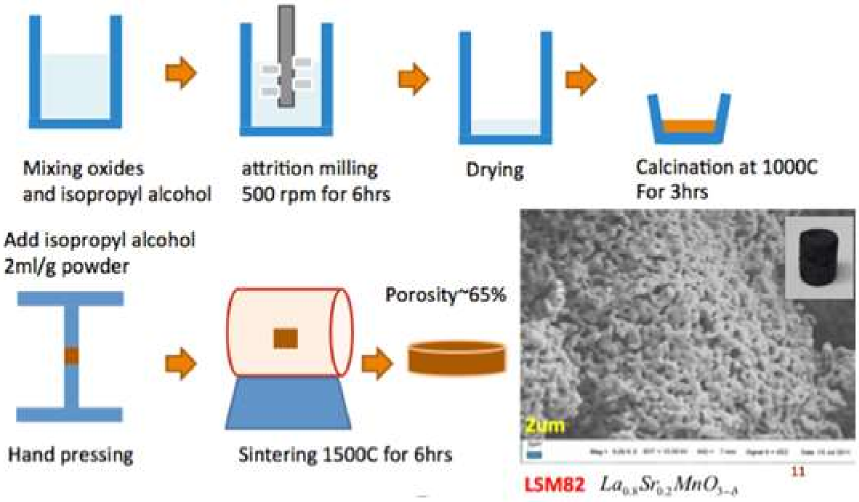

FIGURE 9.1-1 A schematic detailing the solid-state synthesis process. The result is a small pellet (upper right inset) whose microstructure is depicted in the SEM image.

9.1.3 Reticulated Porous Ceramics

The RPC fabrication process permits facile dimensional control at the macroscopic lengthscale [63, 64]. As is typical for RPC fabrication, a polyurethane sponge template with large scale pores, ~ 3 mm (**Figure 9.1-2a**), was coated with a ceramic slurry (**Figure 9.1-2b**). Upon removal of the polymer at high temperature, a macroporous monolith consisting of a network of struts with open porosity was obtained (**Figure 9.1-2c**). The starting powder for RPC preparation was a mixture of coarse (Alfa Aesar, 11328, 5 micron powder, 99.9 %) and fine (STREM chemicals, 58-1400, < 7 nm, > 99.7 %) ceria combined in a 7:3 ratio. The powders were mixed with water in a 6:4 powder:water weight ratio, to which Darvan® 821A (Vanderbilt Minerals, 14442, 5 wt% relative to ceria) was added as a dispersant, and carboxymethyl cellulose sodium (CMC, Tokyo Chemical Industry, C0603, 0.25 wt% relative to ceria) was added as a thickening agent. To create the RPC with bimodal pore structure, hereafter referred to as RPC-50, 50 vol% carbon pore-former (STREM chemicals, 93-0601, 325 mesh, vol% relative to ceria) was added to the slurry [65]. The RPC with unimodal pore structure, the preparation of which did not include this additional pore former, is hereafter referred to as RPC-00.

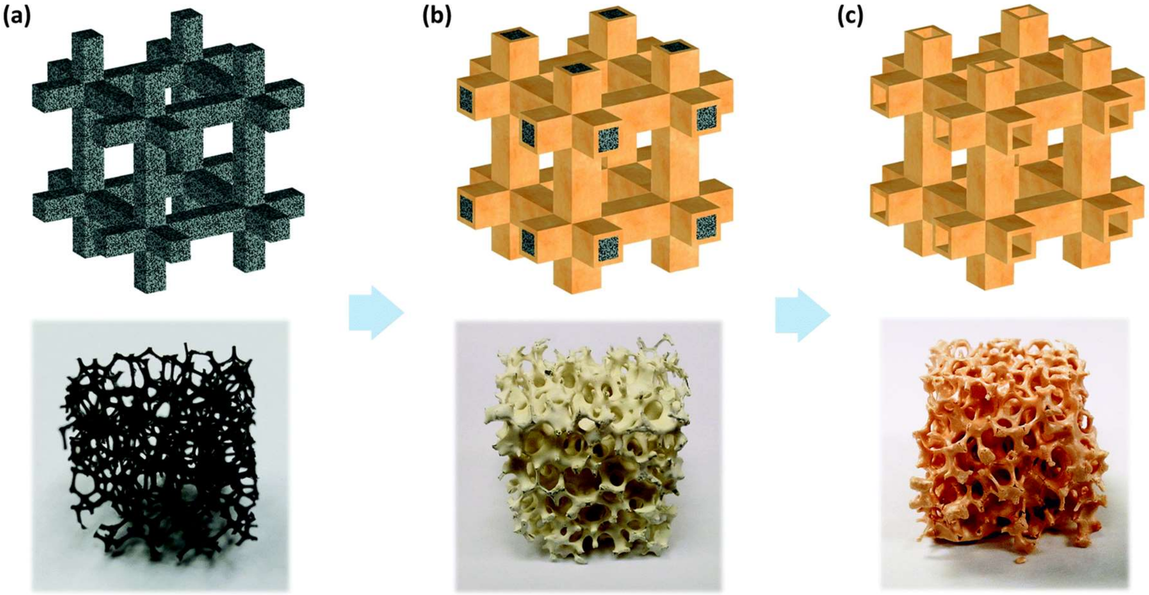

FIGURE 9.1-2 Images outlining the RPC fabrication process: (a) sacrificial polyurethane foam; (b) foam coated with ceramic slurry; and (c) final fired structure [6]

The slurries were ball-milled for 24 hours using YSZ (yttria-stabilized ZrO_2) grinding media. After this homogenization, commercial 10 PPI (pores per inch) Polyurethane (PU) sponges (Foam-Partner, Fritz Nauer AG) of cylindrical shape were immersed in the slurry and then dried at 70 ºC for 1.5 hours. After four repetitions of this coating step, the samples were fired under stagnant air to gently remove the polyurethane matrix and carbon pore-former. This heat treatment protocol was selected on the basis of the thermal decomposition behavior of the organic components as guided by thermogravimetric analysis (TGA). Specifically, the materials were heated stepwise under stagnant air to 500°C for RPC-00, and to 900°C for RPC-50, at a rate of 1°C/min with intermediate 30-minute holds at 300, 325, and 500°C. The temperature was then raised up to 1500°C at a rate of 5°C/min and held for five hours. The image in **Figure 9.1-2c** is that of a typical RPC-00 structure. SEM images of the prepared samples are shown in **Figure 9.1-3** to visually demonstrate the differences in porosity.

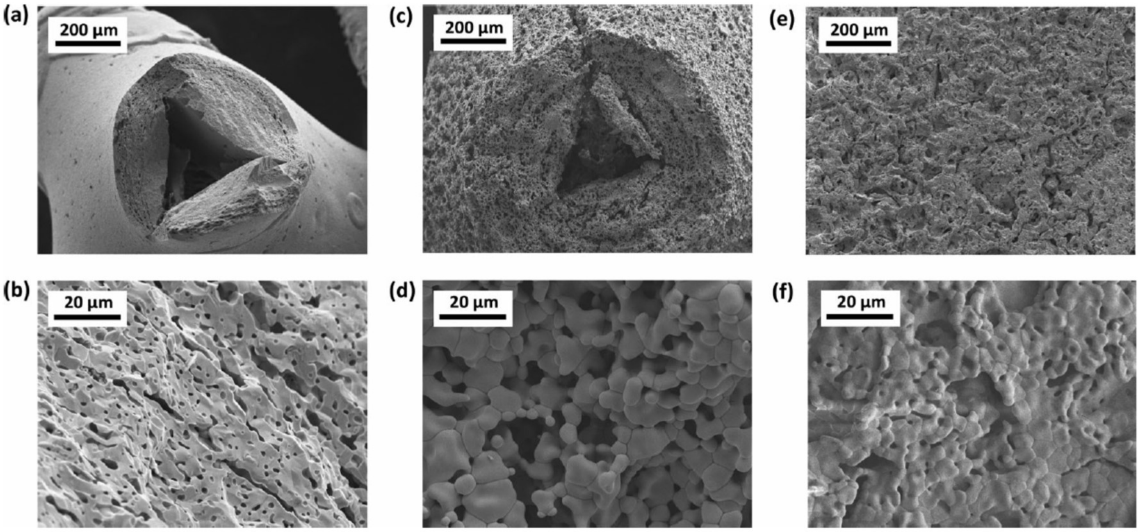

FIGURE 9.1-3 SEM micrographs of cross-sectional fracture surfaces of porous ceria: (a and b) RPC-00, (c and d) RPC-50, and (e and f) porous monolith

9.2 Characterization Methods

9.2.1 X-Ray Diffraction

X-ray diffraction (XRD) was used to determine the crystal structure, phase purity, and lattice parameters of the oxides discussed in this work. During operation, X-rays are generated when high power is delivered to an anode material inside the tube. The X-ray wavelength depends on the anode material (in this case, copper) and the applied accelerating voltage. The incident X-ray will interact with the electron clouds of the atoms in the sample. When Bragg's Law ($2d \sin \theta = n\lambda$) is satisfied with the incident X-ray geometry and the crystallographic planes in the sample, the X-ray is reflected onto a detector. The detector measures an increased intensity, indicating the position of the crystallographic plane. The intensity pattern across all measured incident angles reveals the spacing between the atomic planes. The crystal structure can be determined by comparing the pattern with a pattern of the same material composition in the database. Specifically, a Panalytical, PW3040-PRO diffractometer (Cu Kα source, 45 kV, 40 mA) was employed for polycrystalline samples that had been hand-ground into a powder. The Nelson-Riley method was used to determine the lattice parameter of each sample [66].

9.2.2 Scanning Electron Microscopy

Scanning Electron Microscopy (SEM) is a type of electron microscopy that allows the imaging of a sample’s morphology [7]. In this imaging technique, a focused electron beam strikes a specimen, and the electrons interact with the atoms of the specimen, generating a variety of signals (shown in **Figure 9.2-1**). Backscattered electrons (BSE’s) and secondary electrons (SE’s) are primarily used for SEM imaging. In this work, SEM was used to observe morphology both before and after the samples were thermochemically cycled, ensuring that a transient morphology was not contributing to fuel production trends. The SEM images provide specimen features such as grain size and pore size, which help in understanding the thermal stability properties of the specimen after the synthesis process, or after experimentation. In terms of equipment, electron imaging and qualitative chemical analysis were performed on a Carl Zeiss LEO 1550VP field emission scanning electron microscope (FE-SEM) equipped with an Oxford INCA Energy 300 energy dispersive spectrometer (EDS). SEM and EDS were typically performed with an applied voltage of 10-15 kV and an applied current of 25 nA. Samples were typically coated with carbon to prevent charging.

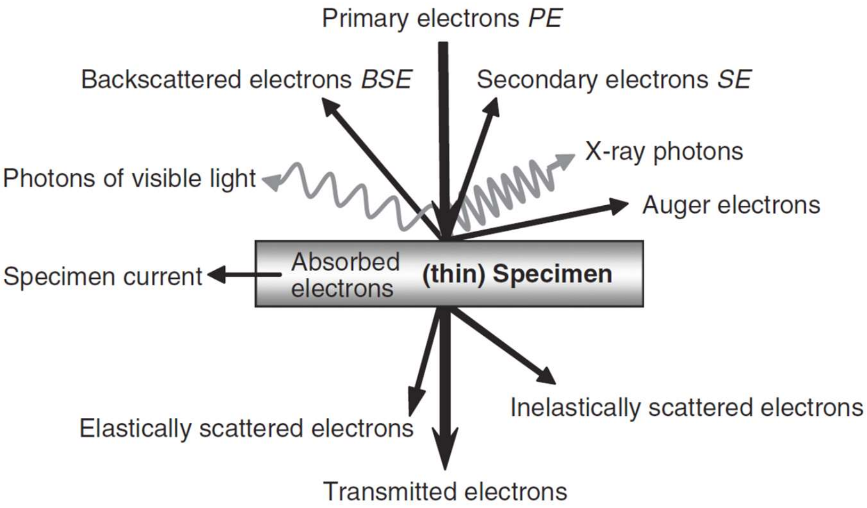

FIGURE 9.2-1 Some of the useful signals that are generated when a focused electron beam strikes a specimen [7].

9.2.3 Mercury Porosimetry

Mercury porosimetry is a technique used to quantify the distribution of pores by volume, number, and diameter in a pellet of arbitrary dimension [67]. Unlike conventional porosity measurements, mercury porosimetry can minimize errors from irregular sample shape, as well as provide insight into the distribution and quantity of various sized pores. Mercury does not wet most substances and will not penetrate pores by capillary action unless an external force applied. Since the surface tension properties of mercury are well understood at given temperatures, an externally applied pressure can be correlated to the diameter of a pore that the mercury will penetrate. During the measurement, an external pressure is applied to an oil bath, which pushes the mercury into the penetrometer (detailed in **Figure 9.2-2**). When the mercury meets the sample, the surface tension initially acts tangentially to the solid-liquid interface, but it then begins to penetrate the sample once a threshold pressure is reached. The relationship between pore diameter and applied pressure is detailed in equation **9.2.3-1**.

$$\boldsymbol{D = \frac{-4\gamma\cos(\theta)}{P}} \qquad \textbf{9.2.3-1}$$

In this equation, γ is the surface tension of mercury, θ is the contact angle (angle between the material surface and the tension force vector), and P is the applied pressure. For a given liquid-solid system, the numerator is constant, and the size of the pore into which mercury will intrude is inversely proportional to the applied pressure. The Hagen–Poiseuille equation, shown below in **Equation 9.2.3-2**, shows the relation between pore volume and applied pressure,

$$\boldsymbol{\Phi = \frac{dV}{dt} = \frac{\pi D^4}{128\eta}\frac{|\Delta P|}{L}} \qquad \textbf{9.2.3-2}$$

where Φ is the volumetric flow rate, V represents the volume of mercury intruded into the pore, L is the length of the pore space, and η is the viscosity of the fluid (mercury). $\frac{|\Delta P|}{L}$ represents the pressure drop per unit length of the pore. By measuring the volume of mercury that intrudes into the sample's pores as a function of applied pressure, the pore volume can be determined.

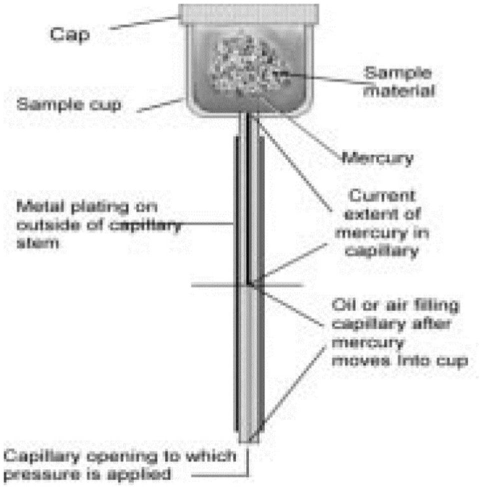

FIGURE 9.2-2 Cross-section of a penetrometer in which pressure has forced some mercury into the pores of the sample, and about 50% of the stem capacity has been used [67].

In this work, an AutoPore IV Micromeritics porosimeter was used for porosimetry measurements. This instrument can resolve 0.1 microliter changes in mercury volume resulting in a porosity detection range down to 10 nm. **Figure 9.2-2** illustrates the sample configuration during the porosity measurement. It is important to note that in this technique closed pores are not measured, which results in an underestimate of the porosity. This is not a concern relative to this work because there is no gas phase access to the closed pores, and they will not contribute to the cycling process.

9.2.4 Quadrupole Mass Spectroscopy

The mass spectrometer is an instrument that can be used to measure the mass-to-charge ratio of ionized atoms and other electrically charged particles [68]. Quadrupole Mass Spectrometry (QMS) is a type of mass spectrometry that uses a quadrupole as the mass analyzer. The quadrupole analyzer schematic is illustrated in **Figure 9.2-3**. The analyzer is held under a vacuum pressure of less than 10 torr. When detecting, the gas molecules enter the vacuum chamber via a capillary tube that samples gas from the main flow. The gas molecules are passed over an ionizer (hot filament), which ionizes the molecules. The ionized molecules are then sorted in the quadrupole mass filter, where four cylindrical electrodes are parallel to each other. An electric potential is applied across opposing rods, and applied potentials affect the trajectory of the ionized molecules traveling through the filter. The applied AC and DC voltages dictate that only ions with a prescribed mass to charge ratio will pass through. After the filtered ionized molecules pass through, they are collected by a detector and generate an ionic current. By oscillating the electric field applied to the quadrupole, the ions passing through the quadrupole filter can be monitored and the sample's mass spectrum can be generated.

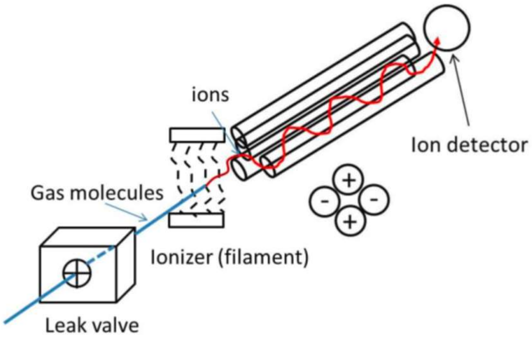

FIGURE 9.2-2 Schematic of the analyzer of a quadrupole mass spectrometer.

For this work, a quadrupole mass spectrometer (QMS, OMNI Star, Pfeiffer-vacuum) is connected to the lab-scale thermochemical test station. The effluent gases from the station are sampled by the QMS. In this way, the oxygen release and fuel (hydrogen or carbon monoxide) production can be quantified as a function of time by correlating the ion current with concentration in the gas stream. A gas calibration measurement is required to convert the ion currents to gas species concentrations, after which the amount of fuel generated from the thermochemical cycles can be calculated.

1. Diver, R.B., et al., *Solar Thermochemical Water-Splitting Ferrite-Cycle Heat Engines.* Journal of Solar Energy Engineering, 2008. **130**(4): p. 041001.
2. Wegner, K., et al., *In situ formation and hydrolysis of Zn nanoparticles for H2H2 production by the 2-step ZnO/Zn water-splitting thermochemical cycle.* International Journal of Hydrogen Energy, 2006. **31**(1): p. 55-61.
3. Marrocchelli, D., et al., *Understanding Chemical Expansion in Non-Stoichiometric Oxides: Ceria and Zirconia Case Studies.* Advanced Functional Materials, 2012. **22**(9): p. 1958-1965.
4. Chueh, W.C., et al., *High-Flux Solar-Driven Thermochemical Dissociation of CO2 and H2O Using Nonstoichiometric Ceria.* Science, 2010. **330**(6012): p. 1797-1801.
5. Roeb, M., et al., *Solar Hydrogen Production by a Two-Step Cycle Based on Mixed Iron Oxides.* Journal of Solar Energy Engineering, 2006. **128**(2): p. 125.
6. Ji, H.-I., et al., *Gas-phase vs. material-kinetic limits on the redox response of nonstoichiometric oxides.* Physical Chemistry Chemical Physics, 2017. **19**(10): p. 7420-7430.
7. Stokes, D.J., *Principles of SEM*, in *Principles and Practice of Variable Pressure/Environmental Scanning Electron Microscopy (VP-ESEM)*. 2008, John Wiley & Sons, Ltd. p. 17-62.
8. Müller, R., P. Haeberling, and R.D. Palumbo, *Further advances toward the development of a direct heating solar thermal chemical reactor for the thermal dissociation of ZnO(s).* Solar Energy, 2006. **80**(5): p. 500-511.
9. Roeb, M., et al., *Test operation of a 100kW pilot plant for solar hydrogen production from water on a solar tower.* Solar Energy, 2011. **85**(4): p. 634-644.